

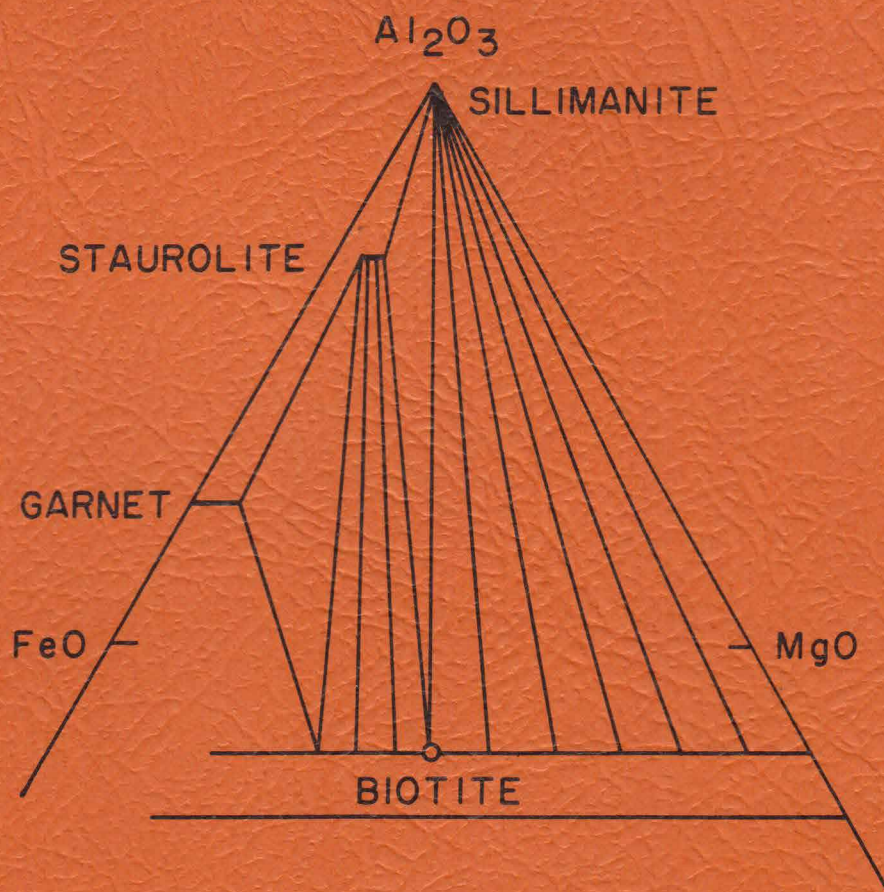
# COMPOSITIONAL VARIATIONS IN BIOTITES AND GARNETS

FROM KYANITE AND SILLIMANITE ZONE  
MICA SCHISTS

## ORANGE AREA

MASSACHUSETTS AND NEW HAMPSHIRE

BY DAVID J HALL



CONTRIBUTION NO. 4  
GEOLOGY DEPARTMENT  
UNIVERSITY OF MASSACHUSETTS  
AMHERST, MASSACHUSETTS

COMPOSITIONAL VARIATIONS  
IN  
BIOTITES AND GARNETS  
FROM  
KYANITE AND SILLIMANITE ZONE MICA SCHISTS,  
ORANGE AREA, MASSACHUSETTS AND NEW HAMPSHIRE

By  
David Joseph Hall

Contribution No. 4  
Department of Geology  
University of Massachusetts  
Amherst, Massachusetts  
February, 1970

## TABLE OF CONTENTS

	Page
Abstract.....	1
Introduction.....	3
Location.....	3
Geologic setting.....	3
Metamorphism.....	6
Purpose of study.....	10
Acknowledgments.....	10
Schist Specimens.....	12
Collection.....	12
Petrography.....	12
Biotites.....	13
Refractive indices.....	13
Measurement of Fe/Mg by X-ray intensity method.....	16
Theoretical basis.....	16
Application.....	21
X-ray measurement of $d_{001}$ .....	25
Separation of biotites for wet chemical analysis.....	25
Composition of analyzed biotites.....	32
Octahedral vacancies.....	34
Octahedral aluminum.....	38
Ferric/ferrous ratio.....	39
Ti content.....	41
Mn content.....	44
K/Na ratio.....	44



	Page
Octahedral Fe.....	47
Comparison of X-ray method with wet-chemical analyses...	50
Comparison of refractive index method with wet-chemical analyses.....	52
Results of X-ray measurements of biotites.....	54
Garnets.....	56
Measurement of compositional zoning.....	56
Composition of zoned garnets.....	60
Metamorphic Petrology.....	68
Regional variation in octahedral Fe-content of biotites.	68
Analysis of phase equilibria.....	69
Composition of biotites and metamorphic grade.....	76
Effect of pressure, temperature, and activity of $H_2O$ .....	90
$fO_2$ by ferric/ferrous ratio.....	90
Origin of garnet zoning.....	92
Conditions of metamorphism of the Orange area.....	97
References cited.....	100
Appendix 1: specimen locations.....	105
Appendix 2: analyses and atom ratios of Dartmouth samples...	110

## ILLUSTRATIONS

Figure	Page
1. Index map of Massachusetts showing Orange area.....	4
2. Stratigraphic column.....	5
3. Mineral compatibilities with quartz and muscovite: Thompson AFM projection.....	9
4. Comparison of refractive indices of 34 biotites deter- mined by both Hall and Robinson.....	15
5. Idealized phlogopite structure.....	17
6. 004 and 005 reflection geometries.....	19
7. Diffractometer chart record of 004 and 005 peaks for biotite U94X.....	23
8. Photomicrograph of biotite 4F5AY.....	30
9. Photomicrograph of biotite 50Y.....	30
10. Photomicrograph of biotite U94X.....	30
11. Photomicrograph of biotite 36Y.....	30
12. Photomicrograph of biotite M53X.....	31
13. Photomicrograph of biotite G24Y.....	31
14. Photomicrograph of biotite 1C7X.....	31
15. Photomicrograph of biotite Q67X.....	31
16. Octahedral vacancies as a function of percent Fe.....	37
17. Ranges in octahedral aluminum composition.....	40
18. Ferric/ferrous ratio as a function of percent total Fe.....	42
19. Comparison of percent of filled octahedral sites occupied by Ti with amounts of ferric and total Fe.....	43
20. Sodium content of biotites as a function of basal d-spacing..	46
21. Comparison of Na/K ratio of coexisting biotites and muscovites.....	48

	Page
22. Relative variation in octahedral Al, Fe, and Mg .....	49
23. Calibration curve for X-ray determinative method of biotites .....	51
24. Comparison of refractive indices and analyses .....	53
25. Calibration curve for X-ray fluorescence determination of mole percent spessartine in garnet.....	61
26. Calibration curve for X-ray fluorescence determination of mole percent almandine in garnet.....	62
27. Comparison of fluorescence milliprobe and electron microprobe analyses .....	66
28. Thompson projection for kyanite-zone specimens .....	71
29. Thompson projection for specimens from lower grade portion of sillimanite zone.....	72
30. Thompson projection for specimens from the higher grade portion of the sillimanite zone.....	73
31. Distorted and enlarged MnO-FeO-MgO diagram of garnets and biotites .....	77
32. Fe/Mg ratio of product biotite per mole of H <sub>2</sub> O as a function of Fe/Mg of reactant biotite <sup>2</sup> .....	83
33. P <sub>H<sub>2</sub>O</sub> -T diagram of biotites and Al <sub>2</sub> SiO <sub>5</sub> .....	89
34. P-T-P <sub>H<sub>2</sub>O</sub> diagram of biotites and Al <sub>2</sub> SiO <sub>5</sub> .....	91
35. Changes in garnet compositions from edges to centers.....	94
36. Possible changes in percent Fe in bulk composition due to three kinds of garnet zoning.....	98

#### Table

1. Distribution of mineral assemblages in mica schists.....	7
2. Modes and beta refractive indices of biotites from selected rock specimens.....	In pocket
3. Basal d-spacings of coexisting biotites and muscovites.....	26
4. Purity of biotite samples submitted for analysis.....	29

	Page
5. Results of chemical analyses.....	33
6. Calculated atomic ratios per 12 (O, OH, F).....	35
7. Calculated atomic ratios per 11 (O) exclusive of H <sub>2</sub> O and assuming all ferric iron is due to weathering.....	36
8. Calculated volume percent of graphite and ilmenite.....	45
9. X-ray data on biotites.....	55
10. Counting statistics and analyses of garnet standards.....	58
11. Compositions of zoned garnets by electron microprobe.....	59
12. Assumed molar volumes.....	81
13. $\Delta S^\circ$ values of reactions involving change in coordination of Al.....	85
14. Types of Al transition in reactions in Table 13.....	86

## Plate

1. Contour map of 100 Fe/occupied octahedral sites in biotites  
in assemblage 2..... In pocket
2. Garnet compositional profiles..... In pocket

Abstract: The Orange area of Massachusetts and adjacent New Hampshire is a gneiss-dome terrane containing mica schists with kyanite or sillimanite. Seven wet-chemical analyses of biotites from the Orange area in the critical assemblage quartz-muscovite-biotite-garnet-staurolite-kyanite or sillimanite indicate that the main areal variation is in the Fe/Mg ratio. A rough measure of this variation is provided by  $\beta = \gamma$  refractive indices, but an X-ray intensity method is preferred for its accuracy and reproducibility. A contour map of Fe in 34 biotites shows one Fe-biotite high near West Orange and one in the central part of the Mt. Grace quadrangle, both extending northwestward from the higher grade region to the southeast. The Fe/Mg ratio in the biotites was probably controlled by the reaction: Mg-rich biotite + staurolite + muscovite + quartz = Fe-rich biotite + kyanite or sillimanite + H<sub>2</sub>O. Thermodynamic calculations suggest that the slope of this reaction would be steeper in the kyanite than in the sillimanite zone. However, point-counted modes show that a change in effective bulk composition in the Thompson AFM projection is also necessary to explain the observed mineralogic variation. One of several possible mechanisms for progressive changes in the effective bulk composition is Fe-zoning in garnets. Semi-quantitative X-ray fluorescence studies of single garnet crystals from some of these same rocks indicate three kinds of Fe-zoning: (1) strong, (2) moderate, and (3) reverse. The mapped variations in the Fe/Mg ratio in biotites of the critical assemblage suggest that local variations in



the activity of  $\text{H}_2\text{O}$  were superimposed upon the pressure and temperature-controlled kyanite-sillimanite isograd at temperatures near  $650^\circ\text{C}$  and pressures near 6 kilobars.

## INTRODUCTION

### Location

The Orange area of Massachusetts and New Hampshire (Robinson, 1963) includes parts of five U. S. Geological Survey 7 1/2 minute series topographic quadrangles: the eastern two-thirds of the North-field and Millers Falls quadrangles, the Mt. Grace and Orange quadrangles, and the western one-quarter of the Athol quadrangle (Fig. 1). The center of the Orange area is approximately 80 miles west of Boston and six miles east of the Connecticut River.

### Geologic Setting

The bedrock geology of the Orange area has been mapped in detail by Robinson (1963, 1967) and will be only briefly summarized here (Fig. 2).

The main post-Cambrian tectonic events in the Orange area took place between the end of Devonian sedimentation and the end of Triassic faulting (Robinson, 1963, 1967). The first of four phases was characterized by formation of large-scale nappe structures with east toward west overfolding. This was followed by a phase of gneiss-dome formation and isoclinal folding about north-south trending axes. The culmination of regional metamorphism accompanied this second phase. The third phase was localized late-metamorphic folding associated with retrograding.

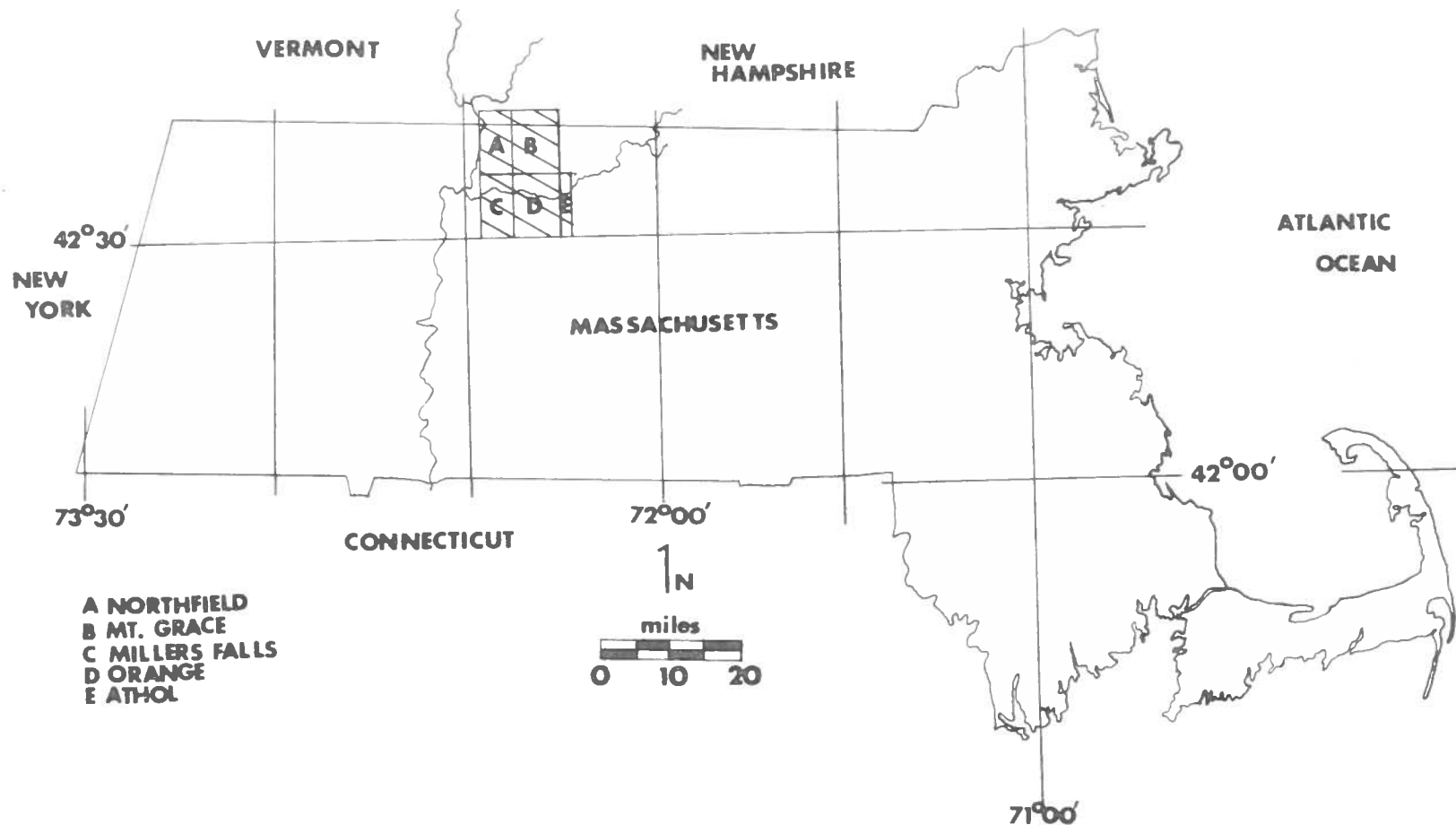


Figure 1. Index map of Massachusetts showing Orange area (ruled). Letters refer to quadrangles listed underneath.

Figure 2. Stratigraphic column (after Robinson, 1967, p. 19-20).

Age	Formation	Thickness	Description
Lower Devonian	Erving Formation	More than 3,000 feet	Hornblende-epidote amphibolite, interbedded quartz-plagioclase-biotite granulite, mica schist, and minor calc-silicate rock.
	Littleton Formation	0-2200 feet	Gray graphitic mica schist and minor quartzite.
-----UNCONFORMITY-----			
Silurian	Fitch Formation	0-800 feet	Discontinuous zones of calc-silicate granulite and minor sulfidic mica schist.
	Clough Formation	0-600 feet	Quartzite, quartz-pebble and quartz-cobble conglomerate, and minor mica schist and calc-silicate rock.
-----UNCONFORMITY-----			
Middle Ordovician	Partridge Formation	0-3,000 feet	Rusty-weathering sulfidic mica schist and gneiss with minor layers of amphibolite, fine-grained feldspar gneiss, and calc-silicate granulite.
	Ammonoosuc Volcanics	0-4,000 feet	Fine-grained feldspar gneiss and amphibolite. Mafic volcanics predominate in the lower part, felsic volcanics predominate in the upper part.
-----UNCONFORMITY-----			
Ordovician? Precambrian?	Gneisses		Coarse-grained gneisses and related rocks in cores of domes -- age uncertain. Includes Pelham Gneiss, Pauchaug Gneiss, Monson Gneiss, and Swanzey Gneiss.

The final phase of deformation was postmetamorphic normal faulting during the Triassic.

Metamorphism. The Orange area has been divided into kyanite and sillimanite zones of regional metamorphism (Pl. 1) (Robinson, 1963). The kyanite zone lies in the western part of the area; the sillimanite zone in the eastern part. The isograd is based on the presence of sillimanite in aluminous rocks. In the Warwick Dome (Pl. 1), no aluminous rocks occur. Here the isograd is drawn trending northwest because of sillimanite occurrences to the north in New Hampshire, and because sillimanite in the schists to the east becomes coarser and more abundant northward, presumably indicating increasing distance from the isograd.

The distribution of mineral assemblages in mica schists in the Partridge, Littleton and Erving Formations is presented in Table 1. All the rocks worked on in this study contain these assemblages, with or without other minerals such as plagioclase, graphite, ilmenite, apatite, and tourmaline. Estimated modes are presented in Table 2. Eight modes point-counted on the basis of 1200 points are also included in Table 2.

It can be seen from Table 1 that there are differences in the mineralogy of the schists of different units in the same metamorphic zone. For example, in the kyanite zone, assemblage 1 is rare in the Erving Formation, is very common in the Littleton Formation, and is common in the Partridge Formation. Robinson (1963) interpreted this variation to be due to original differences in bulk composition, the

Table 1. Distribution of mineral assemblages in mica schists.  
(after Robinson, 1963, Table 39).

- Assemblages: (1) quartz-muscovite-biotite-garnet-staurolite  
(2) quartz-muscovite-biotite-garnet-staurolite-  
kyanite or sillimanite  
(3) quartz-muscovite-biotite-garnet-kyanite or  
sillimanite

	Kyanite zone	Lower grade por- tion of sillimanite zone	Higher grade por- tion of silliman- ite zone
Erving Formation	(1) Rare (2) Common (3) Fairly Common		
Littleton Formation	(1) Very Common (2) Unknown (3) Unknown	(1) Common (2) Very Common (3) Fairly Rare	(1) Rare (2) Fairly Common (3) Very Common
Partridge Formation	(1) Common (2) Rare (3) Unknown	(1) Rare (2) Common (2) Common	(1) Unknown (2) Rare (3) Very Common



Erving Formation being either more magnesian or more aluminous or both.

It can also be seen from Table 1 that there is a variation in the mineralogy of the schists from the kyanite zone in the west to the sillimanite zone in the east. For example, in the Littleton Formation, assemblage 3 is unknown in the kyanite zone, is fairly rare in the lower grade portion of the sillimanite zone, and is very common in the higher grade portion of the sillimanite zone. Robinson (1963) interpreted this change to be due to progressive changes in metamorphic facies, i.e., shifts in tie-line orientations, rather than to shifts in bulk composition. Such progressive changes in facies would be reflected in the compositions of coexisting phases within a given assemblage. This can be shown most readily by graphical means.

The major variations in composition in the ferromagnesian phases listed in the assemblages can be graphically expressed in the system  $K_2O-FeO-MgO-Al_2O_3-SiO_2-H_2O$ . Treating  $H_2O$  as a mobile component and assuming that garnet is present as an additional phase due to  $MnO$  or  $CaO$  or both, the Thompson Projection (Thompson, 1957, p. 851) can be used to portray quartz and muscovite-bearing assemblages (Fig. 3) (Robinson, 1963). Assemblage 2 is of particular interest because the composition of the biotite in this assemblage, to the extent that its composition lies in the chemical system described, should be controlled by pressure, temperature, and activity of  $H_2O$ , and be independent of bulk composition. Thus, any rock with a bulk composition in the three-

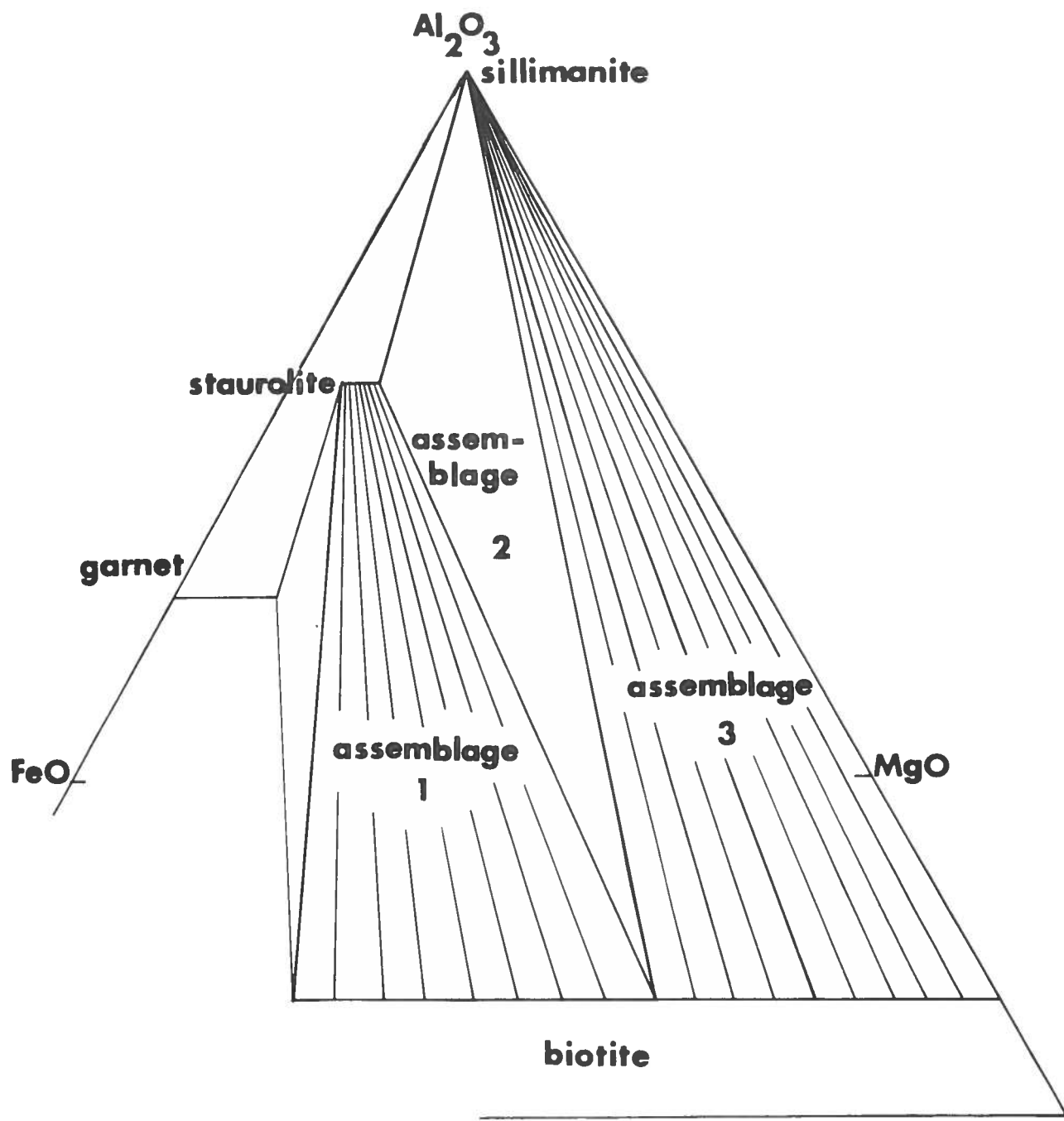


Figure 3. Mineral compatibilities with quartz and muscovite: Thompson AFM projection. Biotite compositions and staurolite Fe/Mg ratio are arbitrary. Assemblage 2 is the critical assemblage because any bulk composition within the three-phase triangle will have a biotite with the same Fe/Mg ratio under identical metamorphic conditions.

phase field biotite-stauroilite-aluminum silicate in Figure 3 will contain biotite with the same composition at the values of pressure, temperature, and activity of  $H_2O$  for which the diagram is drawn.

### Purpose of study

The purpose of this study was to use variations in biotite and garnet compositions as a means to a better understanding of the conditions and history of metamorphism of the rocks of the Orange area. The primary goal was the determination of the biotite compositions in rocks containing assemblage 2. A secondary goal was the determination of the garnet compositions in some of these same rocks. Development and evaluation of reliable laboratory procedures was a requisite first step. The ultimate goal was the deduction of metamorphic history by analysis of the phase equilibria.

### ACKNOWLEDGEMENTS

The author wishes to thank Peter Robinson, chairman of the thesis committee, for his many helpful suggestions and criticisms; Howard Jaffe for his advice on the mineralogic aspects of the problem; and Leo M. Hall, George E. McGill and Joseph H. Hartshorn for thoughtful editing of the manuscript. J. B. Lyons of Dartmouth College kindly supplied four analyzed biotites from New Hampshire. National Science Foundation Grant GA-467 awarded to Howard Jaffe and Peter Robinson, which paid for wet-chemical analyses of

the biotites and field and laboratory expenses, is gratefully acknowledged. The author also wishes to thank Walter Trzcienski for making electron microprobe data on three zoned garnets available.

## SCHIST SPECIMENS

### Collection

Most of the samples on which routine procedures were carried out are in the collection of Peter Robinson, University of Massachusetts. Sample locations are given in Appendix 1 and plotted on Plate 1. It should be emphasized that some of the samples are not in the critical assemblage and are indicated on Plate 1 by different symbols. Collection of samples in bulk large enough for separation and analysis of the biotites was carried on with the aid of Robinson during the summer and fall of 1966 and 1967.

### Petrography

Available thin sections were examined with the polarizing microscope and assemblages and modes of Robinson (1963) confirmed (Table 2). In samples for which there were no thin sections, hand-specimen identification was enough to identify the assemblage. Ten thin sections of specimens which were considered possible candidates for analysis were obtained. Eight of these, the final eight biotite analysis specimens, were point-counted on the basis of 1200 points (Table 2). This number gives a statistical reliability in that section of one percent for an estimated five percent of the mineral present with a 95 percent confidence (Van der Plas and Tobi, 1965, p. 88), not taking into account any error due to the

strongly foliated character of the specimens.

## BIOTITES

### Refractive indices

Measurement of beta  $\approx$  gamma indices of refraction of 40 selected biotites (Robinson, 1963) indicates that chemical variation in biotites in assemblage 2 is continuous. Based on optical curves (Winchell and Winchell, 1951, p. 374) assuming one-third extra aluminum in tetrahedral sites and little or no  $\text{Fe}_2\text{O}_3$ , Robinson (1963) demonstrated progressive shifts in the ratio  $\text{FeO}/(\text{FeO} + \text{MgO})$ . His data show an  $\text{FeO}/(\text{FeO} + \text{MgO})$  maximum in the vicinity of West Orange (0.76) (Pl. 1), decreasing to the west near Erving (0.53-0.58), and decreasing regularly to the northeast (0.55).

The question of reliability of optical measurements has been examined by several researchers. Winchell and Winchell (1951) reported variations in birefringence and gamma refractive index (approximately equal to beta) among the four end members, phlogopite, annite, siderophyllite, and eastonite, on the basis of 37 analyses of natural biotites. They apparently ignored the effects of  $\text{Fe}_2\text{O}_3$  and  $\text{TiO}_2$ . Heinrich (1946) had already found that the gamma refractive index was a curvilinear function of weight percent  $\text{FeO} + 2(\text{Fe}_2\text{O}_3 + \text{TiO}_2)$ , but with much scatter. In view of the fact that the Orange-area biotites are reddish-brown and that Hall (1941) found that reddish-brown colors are due to  $\text{TiO}_2$ , Winchell



and Winchell's (1951) curves must be applied with some caution. Eugster and Wones (1962) also found that the gamma refractive index depends on total iron content and its valence.

Difficulties in measuring the refractive indices of deeply-colored biotites are reported by Engel and Engel (1960). They find that such measurements are liable to considerable error and report the gamma indices of 35 biotites to  $\pm .004$ . Peikert (1963) reports a correlation coefficient of .804 between the gamma index and the Fe/Mg ratio of seven analyzed biotites, but these were from granitic rocks.

An attempt was made to determine the  $\beta \approx \gamma$  index of refraction of 53 biotites using the polarizing microscope (Table 2). Several results taken independently with plane-polarized sodium light and with plane-polarized white light agreed well within the limits of error, so most determinations were made using plane-polarized white light. Indices of refraction of the immersion oils were checked with the Abbe refractometer. Robinson (1963) used both a sodium lamp and white light and checked the matching oil itself on a Leitz-Jelley microrefractometer.

In spite of these precautions, however, there is a lack of agreement between these results and those of Robinson (1963) (Table 2; Fig. 4). The correlation coefficient between the two sets of data is only 0.62, and the mean standard deviation is 0.0052. This should be compared to the mean standard deviation found by Peikert (1963) of 0.0015 on 85 remeasured biotites from granitic rocks in Alberta. It is possible that with more care higher precision could be attained. However, even if precision were improved, accuracy may be low, and a more reliable method is highly

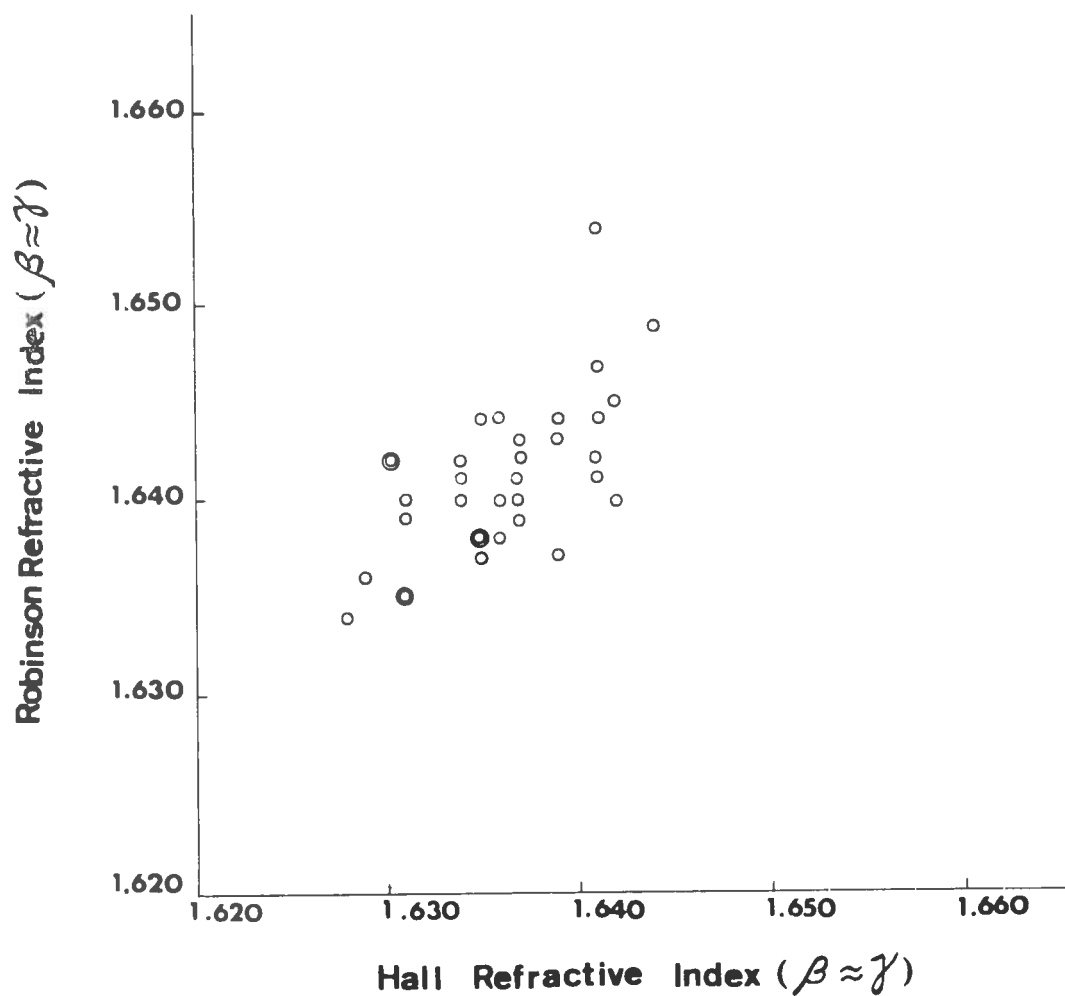


Figure 4. Comparison of refractive indices of 34 biotites determined by both Hall (this work) and Robinson (1963). The correlation coefficient is 0.62, but note that a systematic error is present. Double circles represent coincident measurements.

desirable.

It seems reasonable to conclude that dark color, curled edges, operator differences, or unknown factors combine to make optical index measurements imprecise, and poor indicators of the Fe/Mg ratio, at least in biotites of the chemical complexity studied here.

#### Measurement of Fe/Mg ratios by X-ray intensity method

Theoretical basis. The theoretical basis for the determination of heavy atom compositions of chlorites and biotites was proposed by Brown (1955). Brindley and Gillery (1956), Schoen (1962), and Petruk (1964) investigated the application of the method to chlorites. Gower (1957), Bradley and Grim (1961), and Franzini and Schiafino (1965) investigated the application of the method to biotites. Gottardi (1967) discussed a systematic error in the determination of inhomogeneous samples. All the methods have a theoretical basis in the structure of biotites and the interaction between X-radiation and the ions in the structure.

Biotites can be considered as 4-membered infinite sheet structures (Fig. 5): an octahedral sheet,  $Z_0$ , sandwiched between two tetrahedral sheets,  $Z_2$ , with a 12-fold sheet,  $Z_4$ , holding the layers together. Four groups of ionic substitutions are possible: interlayer substitutions (K-Na-Ca- $H_3O$ ), octahedral substitutions ( $Fe^{2+}$ -Mg-Mn- $Fe^{3+}$ -Al-Ti-vacancy), tetrahedral substitutions (Si-Al- $Fe^{3+}$ ), and anionic substitutions (OH-F-Cl-O) (Foster, 1960; Wones and Eugster, 1965). Any biotite will have some combination of these ions and trace elements in the various

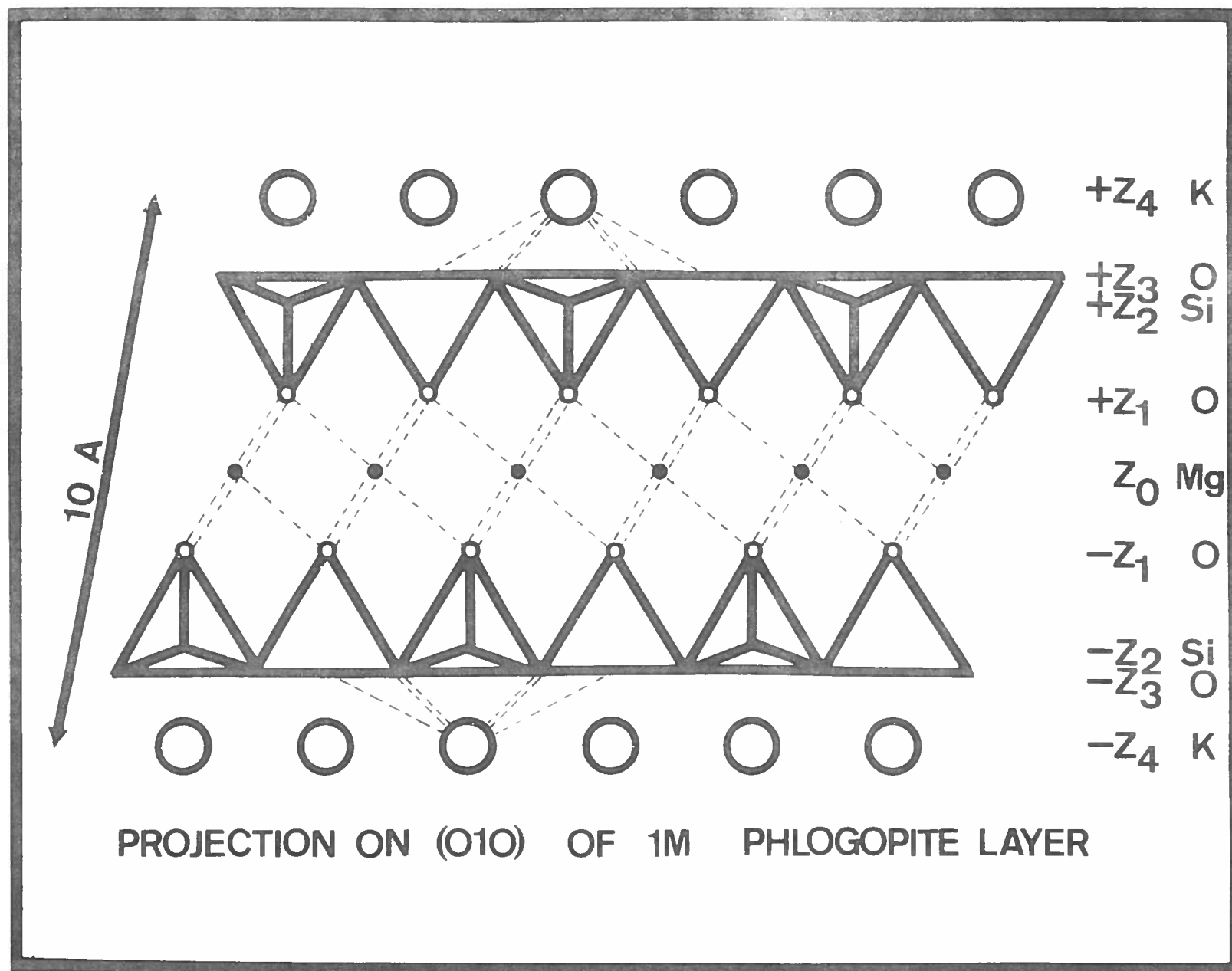


Figure 5. Idealized phlogopite structure (after Brown, 1955). Dashed lines indicate coordination around octahedral and 12-fold layers. Blank triangles are tetrahedra pointing away, triangles with interior lines are pointing toward observer.

sheets.

$\text{FeK}\alpha$  X-radiation of wavelength 1.9373 angstroms interacts with the electron clouds surrounding each ion and is diffracted with some intensity at the incident angle. The intensity of the diffracted beam is a function of the absorption,  $A$ ; the Lorentz-Polarization factor,  $LP$ ; and the square of the structure factor,  $F^2$ :  $I = K F^2 LP A$  (Franzini and Schiafino, 1965, p. 104). The structure factor is a function of the atomic scattering power, position in the unit cell and the order of the reflection.  $A$  and  $LP$  are functions of  $\theta$ , the incident angle.  $K$  is a constant depending on the experimental arrangement.

For the case of a basal reflection of a biotite ( $00l$ ), the structure factor is calculated from the following summation (Bradley and Grim, 1961, p. 218):

$$F_{00l} = 2 \sum f_a \cos 2\pi l z,$$

where  $f_a$  is the atomic scattering factor of atom  $a$ , and  $z$  is the vertical distance of the atom center from the origin. For this purpose the symmetry plane running through the octahedral sheet is considered the origin. The trigonometric term,  $\cos 2\pi l z$ , is needed to give the proper phase to the wave contributing to the intensity. This can be seen by reference to Figure 6. In the  $004$  reflection geometry, the waves from the octahedral and 12-fold atoms are in phase and reinforce each other. In the  $005$  reflection geometry, the waves from the octahedral atoms are out of phase and interfere destructively. Thus, for pure phlogopite, the structure-factor expression for the  $004$  and  $005$  reflections can be written:

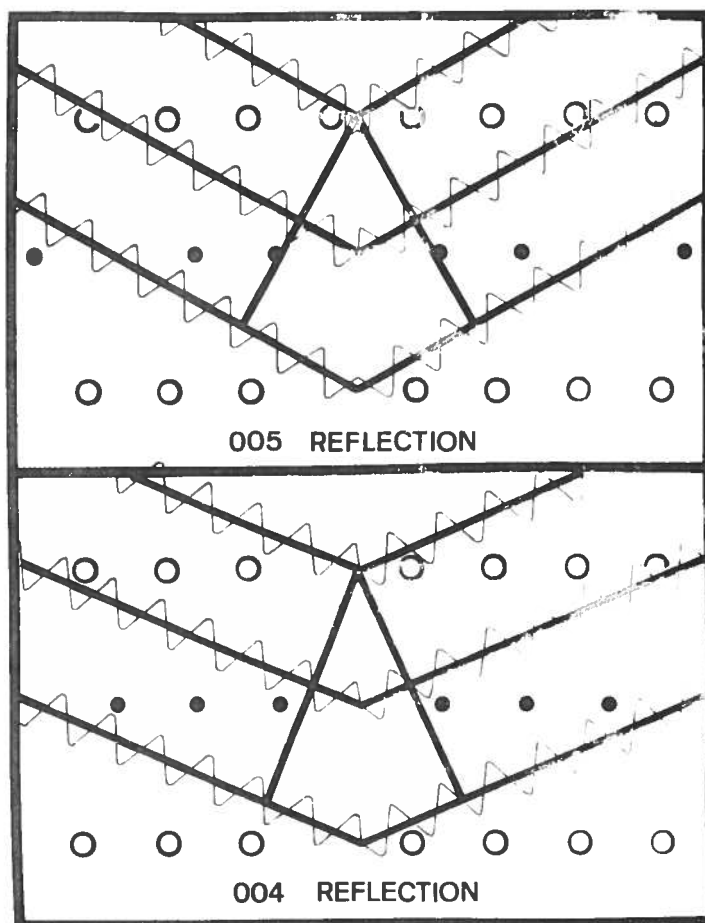


Figure 6. 004 and 005 reflection geometries. Destructive interference occurs in 005 reflection, constructive interference occurs in 004 reflection.



$$F_{004} = 6f_{Mg} \cos 0 + 2f_K (-1)^4 + 8f_{Si,Al} \cos 2\pi \lambda z_{Si} + 12f_O \cos 2\pi \lambda z_{O_A} + \\ 12f_O \cos 2\pi \lambda z_{O_B}$$

$$F_{005} = 6f_{Mg} \cos 0 + 2f_K (-1)^5 + 8f_{Si,Al} \cos 2\pi \lambda z_{Si} + 12f_O \cos 2\pi \lambda z_{O_A} + \\ 12f_O \cos 2\pi \lambda z_{O_B}.$$

Substitution of the  $z$  coordinates for Si, Al,  $O_A$ , and  $O_B$  from Franzini and Schiafino (1963, p. 301) allows the reduction of these equations to:

$$F_{004} = 6f_{Mg} + 2f_K + 8f_{Si,Al}(0.83) - 12f_O(1.36)$$

$$F_{005} = 6f_{Mg} - 2f_K - 8f_{Si,Al}(0.68) - 12f_O(1.50).$$

For pure annite, the only change is in the scattering factor for the octahedral atoms:

$$F_{004} = 6f_{Fe} + 2f_K + 8f_{Si,Al}(0.83) - 12f_O(1.36)$$

$$F_{005} = 6f_{Fe} - 2f_K - 8f_{Si,Al}(0.68) - 12f_O(1.50).$$

As Fe is substituted for Mg,  $F_{004}$  increases because  $f_{Fe}$  is much greater than  $f_{Mg}$ , and the sign of  $F$  is positive. Therefore the ratio of  $F_{004}^2/F_{005}^2$  increases, all other substitutions being equal, as Fe is substituted for Mg. The effect is the same for substitution of ions with  $f$  similar to that of Fe, in place of ions with  $f$  similar to Mg. One really measures the ratio of Fe, Mn, and Ti to Al, Li, and Mg in

the octahedral positions. Since Mn and Ti are commonly present in small amounts only, the structure factor ratio is primarily a function of percent octahedral Fe. Octahedral vacancies will produce an effect on intensities in the same direction as the substitution of Mg for Fe. Thus it is important to evaluate the extent of the vacancies by chemical analysis of similar biotites and to construct a calibration curve for biotites with similar percentages of vacancies (Franzini and Schiafino, 1965; Foster, 1960).

Application. In order to obtain good results with the X-ray method, the biotite samples had to be separated and partially purified. A small portion of each of the samples was crushed and then sieved. A mesh of liberation which was also convenient for use in the Frantz Iso-dynamic Magnetic Separator was established at between U. S. Bureau of Standards screens no. 80 and 100 (177-149 microns).

This mesh fraction was then run on the Frantz Separator at settings which varied with the sample, but were approximately 20 degrees side tilt and 25 degrees forward slope. Amperage was then varied, first to split off non-magnetic minerals, mostly muscovite and quartz, and then to split off the more magnetic fraction, predominantly garnet. All fractions were examined with the binocular microscope for traces of weathering and chlorite, and to establish mineral identities in the fraction.

The resulting purified sample was ground using an agate mortar and

pestle until visual inspection showed lack of recognizable cleavage flakes. A few drops of water were then mixed with the sample. Part of the sample was drawn off and centered on a glass slide. Heatlamp drying was then used to precipitate an oriented smear mount. The oriented specimen was preferred because only basal peaks were to be measured, and orientation enhanced their development. The randomly oriented mount proposed by Gower (1957) was not used, because possible superposition of hkl peaks could lead to large and unknown errors (Franzini and Schiafino, 1965, p. 101).

All specimens were run on a General Electric XRD-5 X-ray diffractometer. Both Cu and Fe radiation were tried, and since Fe yielded the best results all specimens were run using Fe radiation. The slit system used was as follows:  $0.1^\circ$  detector, medium-resolution soller, and  $1^\circ$  medium-resolution beam slit. Two thicknesses of Mn filter material of density  $.005 \text{ g/cm}^2$  and thickness  $.020 \text{ mm}$  were used. This compares favorably with the optimum thickness of  $.016 \text{ mm}$  of  $.012 \text{ g/cm}^2$  density Mn filter material recommended by Azaroff and Buerger (1958, p. 34). This thickness reduces  $K_\beta / K_\alpha$  to  $1/600$ . The experimental constants were: 8-second time constant, 100 counts/second range,  $0.2^\circ/\text{minute}$  chart speed, 8 milliamperes, 49 kilovolts. A complete scan was made from  $44.70^\circ 2\theta$  to  $45.70^\circ 2\theta$  for the 004 peak and from  $56.90^\circ 2\theta$  to  $57.90^\circ 2\theta$  for the 005 peak. This enabled background levels to be drawn on the chart records more accurately (Fig. 7).

Background levels were drawn in by eye on the chart tracings and

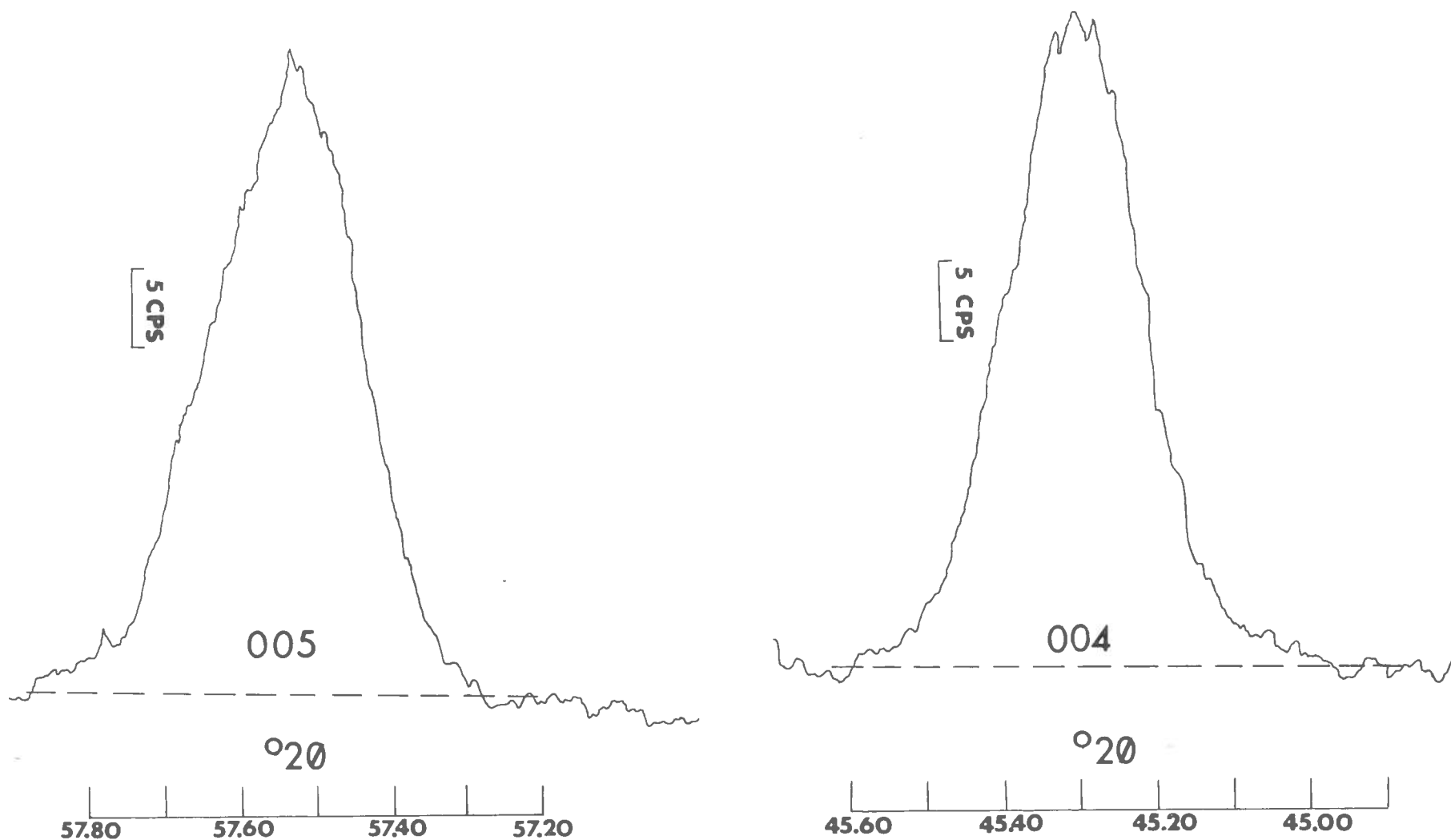


Figure 7. Diffractometer chart record of 004 and 005 peaks for biotite U94X. Peaks are of moderate intensity. Dashed lines are the estimated background levels.

areas were read off by a square-counting method. This method of graphical integration proved much more reproducible than measurement and comparison of peak heights. Reproducibility checks of three rerun samples show that intensity ratios can be reproduced to  $\pm 0.02$  (corresponding to 0.7% Fe), on peaks with moderate peak/background ratios. On smaller peaks, a reproducibility range of  $\pm 0.04$  (1.4% Fe) is probably more realistic.

The peak angle was used to determine the LP factor by the equation:  $LP = (1 + \cos^2 \theta) / \sin 2\theta$ . Values for this function were interpolated from Henry, Lipson, and Wooster (1961, Table 8, p. 262). This form of LP factor is applicable to the oscillating or rotating crystal method, or to perfectly oriented aggregates (Franzini and Schiafino, 1965, p. 105).

Using the integrated intensities, a structure factor ratio was then calculated according to the equation:

$$I_{004}/I_{005} = F_{004}^2/F_{005}^2 \times LP_{004}/LP_{005}.$$

The terms incident intensity, unit-cell volume, multiplicity factor are the same for both 004 and 005 and hence cancel out of the equation (see the formula by Brindley and Gillery, 1956, Appendix 1, or the formula by Schoen, 1962). The absorption factor was not evaluated, but because the 004 and 005 peaks occur within a limited range of  $\theta$ , and because the samples were relatively thick smear mounts, it is believed that the error is not serious (Franzini and Schiafino, 1965, p. 106).

### X-ray measurement of $d_{001}$

The possibility that substitution of Na for K might influence the basal d-spacing in biotites, as it does in muscovites (Evans and Guidotti, 1966), was tested by using new mounts of the eight analyzed biotites. Fluorite was used as an internal standard in appropriate amounts to give approximately equivalent heights for the biotite 005 and the fluorite 220 peaks. Each peak was run in both a forward and backward  $2\theta$  direction and the  $2\theta$  value of the 2/3-height midpoint of the two runs averaged. This  $2\theta$  value was subtracted from the  $2\theta$  of the 220 peak of fluorite ( $60.21^\circ 2\theta$ ) and the  $d_{005}$  of biotite was computed. There was no significant difference in d-spacing among the 8 specimens, even though the coexisting muscovites showed pronounced differences (Farrukh Ahmad, oral comm., 1969) (Table 3).

### Separation of biotites for wet-chemical analysis

Eight biotites were selected for wet-chemical analysis to serve as calibration standards and to provide information on the range of  $\text{Fe}_2\text{O}_3/\text{FeO}$ , octahedral vacancies,  $\text{TiO}_2$  content, etc. These biotites were selected from 40 sample localities as the most suitable on the basis of: (1) proof of assemblage, (2) freshness and purity, (3) wide geographic latitude and (4) wide range of biotite composition as indicated by X-ray and optical determinations. Thin sections of all specimens containing the biotites to be analyzed were obtained.

These eight samples were then sawed or broken to remove weathered

Table 3. Basal d-spacings of coexisting biotites and muscovites.  
Muscovite data by Farrukh Ahmad, 1969.

Sample Number	<u>Muscovite</u>		<u>Biotite</u>	
	5 X d <sub>00.10</sub>	Inferred* 100 Na/(Na+K)	5 X d <sub>005</sub>	Analyzed 100 Na/(Na+K)
4F5AY	9.9550	19.0	9.8625	4.9
50Y	9.9610	15.7	9.8625	6.1
U94X	9.9220	31.3	9.8625	7.2
36Y	9.9695	13.5	9.8585	4.4
M53X	9.9485	21.4	9.8605	6.3
G24Y	9.9385	25.2	9.8625	5.7
1C7X	9.9320	27.5	9.8585	6.9
Q67X	9.9505	20.5	9.8625	6.3

\*Muscovite 100 Na/(Na+K) inferred from curve of  
Evans and Guidotti (1966, p. 39).

surfaces and carefully inspected for chlorite veins. The samples were then crushed and sieved. A magnetic separation was made to purify the samples to the same degree as the X-rayed samples. The previously described X-ray procedure was then followed for all samples. All magnetic fractions were visually inspected for traces of chlorite or weathered material and to check purity and assemblage.

The partially purified sample was then passed through two heavy-liquid separations using bromoform ( $d=2.89$ ) and methylene iodide ( $d=3.33$ ). This effectively diminished quartz, staurolite, garnet, plagioclase, graphite, and ilmenite in the sample, except where the impurities were small and locked with the biotite. The heavy-liquid separations were also successful in concentrating staurolite, even if staurolite was present in only minute amounts and was not readily detected in thin section.

Final purification involved four more passes on the magnetic separator. Each pass reduced the sample by about ten percent, thus extremes in composition on both sides of the mean were subtracted out in approximately equal amounts. Even if some degree of inhomogeneity was present, the separation procedure should not affect the mean composition as deduced by analysis.

The purity of the final sample was determined by a fragment counting technique. One thousand random grains of each sample were counted to determine purity. The eight samples averaged 99.5 percent pure, with a range from 98.8 percent to 99.8 percent pure. The fragment purities of



each sample are listed in Table 4, column A. Most of the impurities consisted of grains of biotite with quartz.

An attempt was made to evaluate the numerous opaque inclusions within the biotite flakes themselves by a photographic technique. Representative grains were photographed in immersion oils under the polarizing microscope (Figs. 8-15). The photographs were enlarged so that the biotites were 240 times their actual size. A transparent square grid with points at 1/10-inch intervals was constructed on acetate. The grid was large enough to cover the largest flakes in any of the photographs. More than 1,000 points on the grid corners were identified and counted as biotite or opaque inclusions for each sample (except 36Y for which 837 points were counted), and percentages of opaque inclusions determined (Table 4, column B). Since the biotites are non-opaque this technique integrates over a considerably greater thickness than the inclusions themselves. Thus another dimension must be obtained to get a true picture of volume percentage of inclusions. This can be gained by thin-section examinations, since the thin sections were purposely taken at right angles to the schistosity, and hence to the mica cleavage in the rock. In edgewise views in thin sections, the biotites all have fewer apparent inclusions than the biotite plates in immersion oils. The inclusion impurity by volume can be evaluated from the inclusion impurity by area. Let  $n$  be the inclusion impurity by area.  $\sqrt{n}$  represents the side of a square of area equal to  $n$ .  $(\sqrt{n})^3$  represents the volume of a cube with sides equal to  $\sqrt{n}$ . Since  $n$  is a fraction of 100, the total area of which  $n$  is a fraction is equivalent to a square of sides equal to

Table 4. Purity of biotite samples submitted for analysis.

Sample	A Fragment Purity (%)	B Inclusions by Area (%)	C Inclusion Purity by Volume $100 - \frac{B}{10}$	D Final Purity (%) A X C
4F5AY	99.7	5.5	98.71	98.4
50Y	99.8	3.0	99.48	99.3
U94X	99.6	6.3	98.42	98.0
36Y	99.3	3.2	99.39	98.7
M53X	99.8	2.0	99.72	99.5
G24Y	98.8	6.0	98.53	97.4
1C7X	98.9	1.1	99.88	98.8
Q67X	99.7	0.5	99.96	99.7

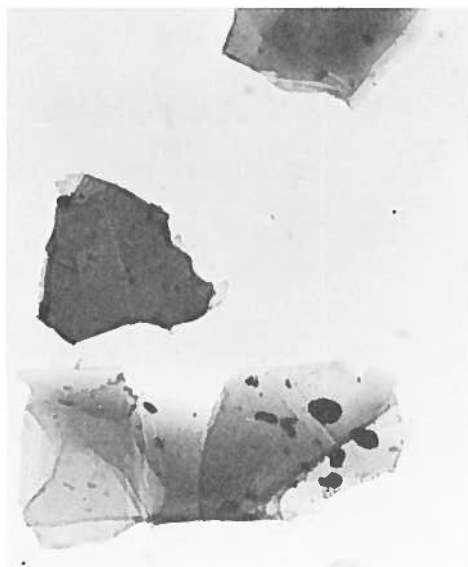


Figure 8. Sample 4F5AY X60

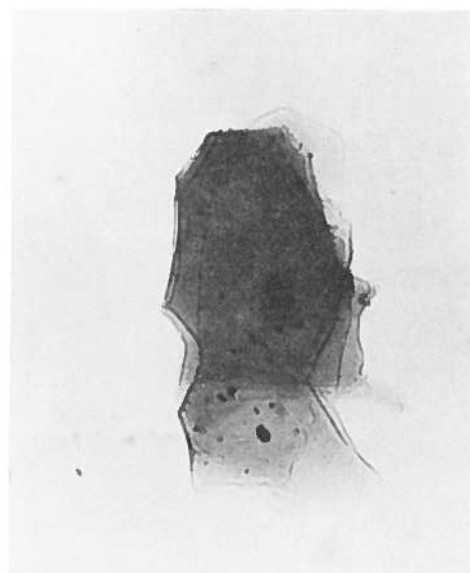


Figure 9. Sample 50Y X60

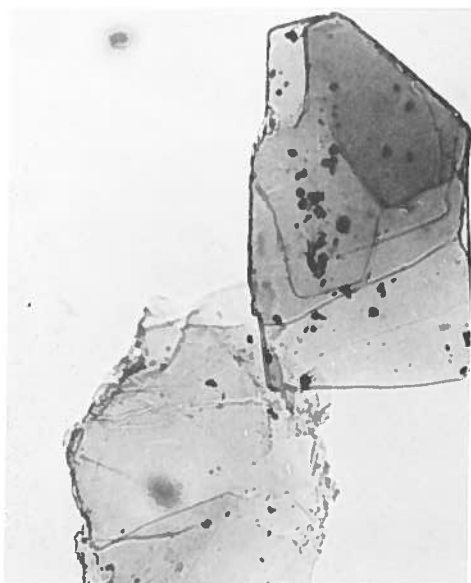


Figure 10. Sample U94X X60



Figure 11. Sample 36Y X60

Figures 8-11. Photomicrographs of biotites in immersion oil of refractive index = 1.540.

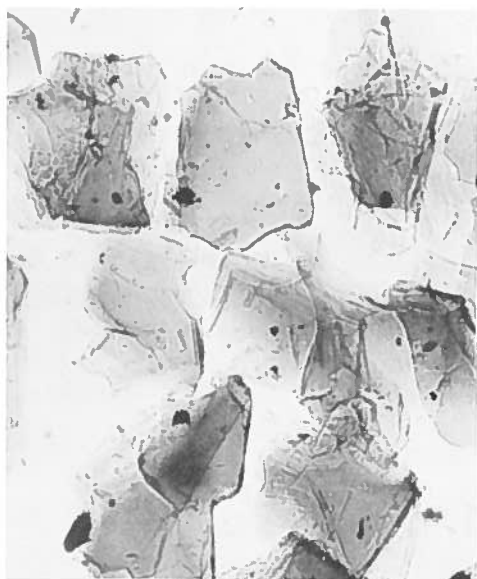


Figure 12. Sample M53X X60



Figure 13. Sample G24Y X60

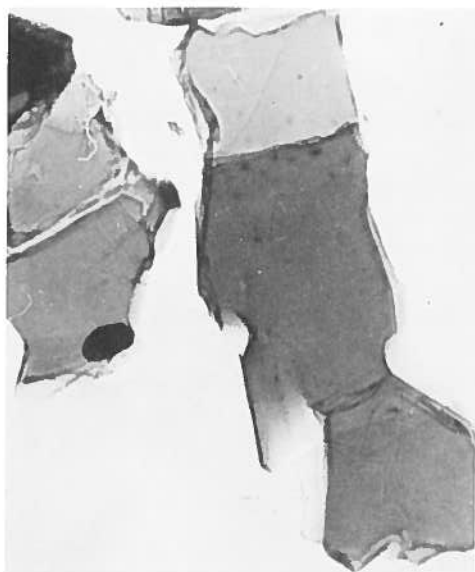


Figure 14. Sample 1C7X X60



Figure 15. Sample Q67X X60

Figures 12-15. Photomicrographs of biotites in immersion oil of refractive index = 1.540.

$\sqrt{100} = 10$ .  $10^3 = 1,000$  is then the volume of which  $(\sqrt{n})^3$  is a fractional part. Dividing  $(\sqrt{n})^3$  by 1,000 then gives the fractional impurity by volume. Multiplying by 100 converts the fraction to percent. Thus the percent volume impurity is  $0.1 (\sqrt{n})^3$ . The product of fragment purity and inclusion purity gives the final percent purity (Table 4, column D). This is a minimum figure, because the inclusion impurity assumed in the third dimension is greater than the actual impurity.

All the inclusions encountered are either graphite or ilmenite, both occurring as plates oriented parallel to the micaceous cleavage of the biotites. The great majority of the inclusions are graphite, as determined by hardness tests with a needle. Since it was deemed all but impossible to separate out the inclusions, an attempt was made to correct for the inclusions by getting carbon analyses of all the samples.

#### Composition of analyzed biotites

The results of the chemical analyses of the eight biotite samples as reported by the Japan Analytical Chemistry Research Institute are given in Table 5. These analyses were recalculated to atomic ratios using a method based on reported  $H_2O(+)$  and F values, rather than on ideal  $O(OH)$  contents (Foster, Wones and Eugster, 1963, p. 306). The method of calculation is indicated by the following equations:  $E = W n C/M$ ;  $R = 24 E / C \sum E$ , where E is gram equivalent, W is weight percent of oxide, n is number of cations in oxide, C is cationic charge, M is molecular weight and R is atomic ratio. F and Cl are treated in the same manner as the cations,

Table 5. Results of chemical analyses.

33

	4F5AY	50Y	U94X	36Y	M53X	G24Y	1C7X	Q67X
SiO <sub>2</sub>	35.68	35.69	35.76	36.34	35.75	35.56	35.49	36.22
TiO <sub>2</sub>	1.82	1.94	1.59	2.43	1.55	1.67	1.63	1.62
Al <sub>2</sub> O <sub>3</sub>	19.87	19.70	20.13	19.53	20.48	19.73	19.68	20.02
Fe <sub>2</sub> O <sub>3</sub>	2.04	1.91	1.58	2.95	1.28	2.21	1.92	1.60
FeO	17.29	17.38	17.64	19.01	18.05	19.20	19.40	16.75
MnO	0.02	0.06	0.02	0.03	0.02	0.01	0.01	0.02
MgO	9.78	10.80	10.09	6.63	9.45	8.13	8.19	10.60
CaO	0.09	0.22	0.09	0.11	0.07	0.08	0.07	0.06
Na <sub>2</sub> O	0.29	0.36	0.41	0.26	0.39	0.33	0.41	0.38
K <sub>2</sub> O	8.59	8.42	8.07	8.63	8.74	8.37	8.47	8.57
H <sub>2</sub> O(+)	4.24	4.00	4.37	4.41	4.18	4.43	4.37	3.90
H <sub>2</sub> O(-)	0.45	0.62	0.32	0.55	0.42	0.53	0.32	0.38
C	0.12	0.07	0.09	0.06	0.12	0.03	0.19	0.05
Li <sub>2</sub> O	0.03			0.01	0.03	0.01	0.03	0.02
SrO	0.01		0.01	0.01	0.01	0.01	0.01	0.01
BaO	0.01		0.01	0.01	0.01	0.01	0.01	0.01
F	0.10				0.09	0.10	0.10	0.09
Cl	0.00				0.01	0.01	0.01	0.02
S	0.01		0.01	0.01	0.01	0.01	0.01	0.01
Rb <sub>2</sub> O	0.05				0.12	0.09	0.09	0.05
Total	100.49	101.17	100.19	100.98	100.78	100.52	100.41	100.38
O ≡ F, Cl	-.04				-.04	-.04	-.04	-.04
	100.45	101.17	100.19	100.98	100.74	100.48	100.37	100.34

Analyst: Shiro Imai, Japan  
Analytical Chemistry  
Research Institute

except that W is weight percent of the element,  $n = 1$ ,  $C = 1$ , and M is the atomic weight of the element. Hydrogen is treated as any other cation. The summation over all E includes the cations and the anions. The calculated atomic ratios are given in Table 6. In Table 7, the atomic ratios are recalculated assuming an ideal biotite formula with 11 (O) and all  $\text{Fe}^{3+}$  calculated as  $\text{Fe}^{2+}$ . This was done as a check on the  $\text{H}_2\text{O}$  analysis and to try to determine if part of the ferric iron might be explained by weathering.

The carbon contents are assumed to be due entirely to graphite inclusions or amorphous carbon. All analyses contain carbon, although no carbonaceous inclusions are observable in 50Y. A graphite-muscovite concentration of specimen U94X, which is relatively rich in carbonaceous material, showed no graphite peaks when X-rayed, but the evidence is inconclusive. Correlation between carbon analyses and estimated abundances of carbonaceous material in hand specimens is poor.

Sulfur is ignored for the purposes of calculation because it represents only 0.01 weight percent and shows no variation from one sample to another. Correlation between sulfur analyses and recognized sulfide content of hand specimens (recognized only in 36Y) is poor.

Octahedral vacancies. The number of octahedral vacancies is in the general range expected by comparison with Foster (1960) and Franzini and Schiafino (1965). The decrease in occupancy is in the direction of increasing iron (Fig. 16, top), but the decrease is more abrupt than that

Table 6. Calculated atomic ratios per 12 (O, OH, F).

	4F5AY	50Y	U94X	36Y	M53X	G24Y	1C7X	Q67X
Si	2.664	2.657	2.661	2.717	2.668	2.669	2.670	2.700
Al <sup>IV</sup>	1.336	1.343	1.339	1.283	1.332	1.331	1.330	1.300
Al <sup>VI</sup>	0.411	0.385	0.426	0.436	0.468	0.414	0.415	0.458
Ti <sup>4+</sup>	0.102	0.108	0.089	0.136	0.087	0.094	0.092	0.091
Fe <sup>3+</sup>	0.114	0.107	0.088	0.166	0.072	0.125	0.109	0.090
Fe <sup>2+</sup>	1.079	1.081	1.097	1.188	1.126	1.204	1.220	1.044
Mn <sup>2+</sup>	0.001	0.004	0.001	0.002	0.001	0.001	0.001	0.001
Mg	1.087	1.197	1.118	0.738	1.050	0.909	0.918	1.177
Li	0.009			0.003	0.009	0.003	0.009	0.006
Ca	0.007	0.017	0.007	0.009	0.006	0.006	0.006	0.005
Na	0.042	0.052	0.059	0.038	0.056	0.048	0.060	0.055
K	0.818	0.799	0.765	0.822	0.832	0.801	0.812	0.815
Rb	0.002				0.006	0.004	0.004	0.002
F	0.024				0.021	0.024	0.024	0.021
Cl	---				0.001	0.001	0.001	0.003
OH	2.109	1.985	2.167	2.197	2.078	2.216	2.191	1.940
O	9.867	10.015	9.833	9.803	9.899	9.759	9.784	10.037
Inter-layer	0.869	0.868	0.834	0.869	0.900	0.860	0.882	0.877
Octa-hedral	2.804	2.883	2.819	2.669	2.813	2.750	2.763	2.866
Octahed. Vacancy	0.196	0.117	0.181	0.331	0.187	0.250	0.237	0.134
Fe/Fe+Mg	0.523	0.498	0.515	0.647	0.533	0.594	0.592	0.491
% Fe of filled VI sites	42.55%	41.22%	42.06%	50.70%	42.57%	48.34%	48.09%	39.54%



Table 7. Calculated atomic ratios per 11(0) exclusive of H<sub>2</sub>O and assuming all ferric iron is due to weathering.

	4F5AY	50Y	U94X	36Y	M53X	G24Y	1C7X	Q67X
Si	2.692	2.667	2.691	2.761	2.687	2.713	2.709	2.708
Al <sup>IV</sup>	1.308	1.333	1.309	1.239	1.313	1.287	1.291	1.292
Al <sup>VI</sup>	.460	.402	.477	.510	.502	.487	.481	.473
Ti <sup>4+</sup>	.103	.109	.090	.139	.088	.096	.094	.091
Fe <sup>2+</sup>	1.207	1.194	1.200	1.376	1.207	1.352	1.349	1.128
Mn <sup>2+</sup>	.001	.004	.001	.002	.001	.000	.000	.001
Mg	1.100	1.203	1.132	0.751	1.059	0.924	0.932	1.181
Li	.009			.003	.009	.003	.009	.006
Ca	.007	.018	.007	.009	.005	.006	.006	.004
Na	.042	.052	.060	.038	.057	.049	.061	.055
K	.827	.803	.775	.836	.838	.815	.825	.818
Rb	.002				.005	.005	.005	.003
F	.024				.021	.024	.024	.021
Cl	.000				.001	.001	.001	.002
H	2.134	1.994	2.194	2.235	2.096	2.255	2.225	1.945
Inter-layer	.878	.873	.842	.883	.905	.875	.897	.880
Octa-hedral	2.881	2.911	2.900	2.780	2.866	2.862	2.865	2.880
Octahed. Vacancy	.119	.089	.100	.220	.134	.138	.135	.120
Fe/Fe+Mg	.523	.498	.515	.647	.533	.594	.591	.489
% Fe of filled VI sites	41.90	41.00	41.37	49.50	42.11	47.23	47.08	39.16

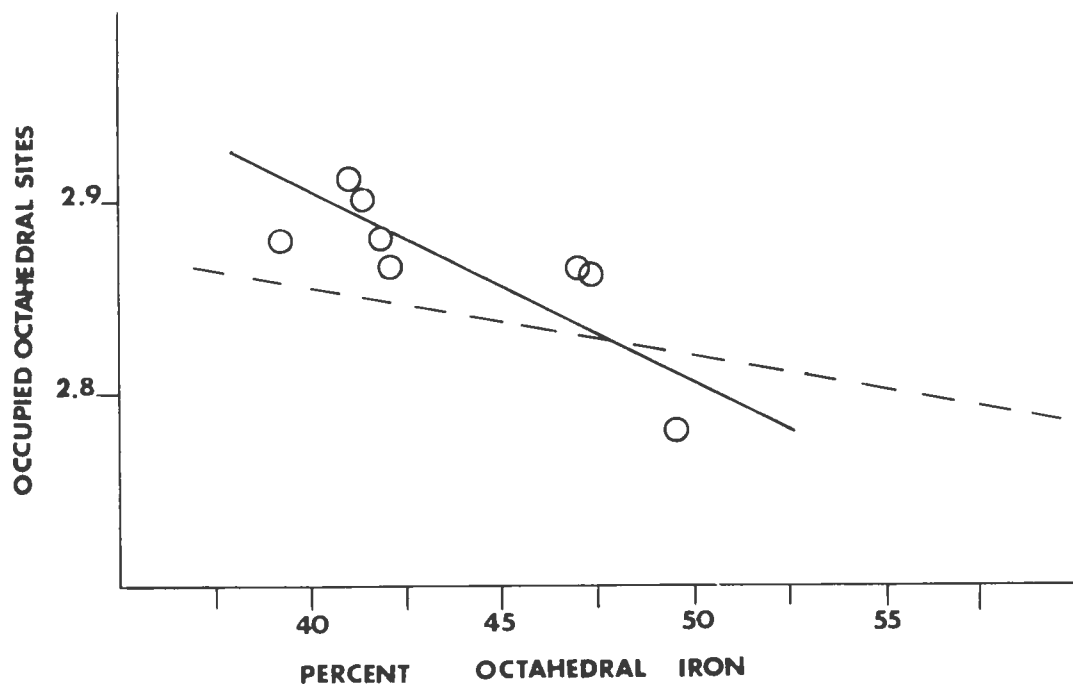
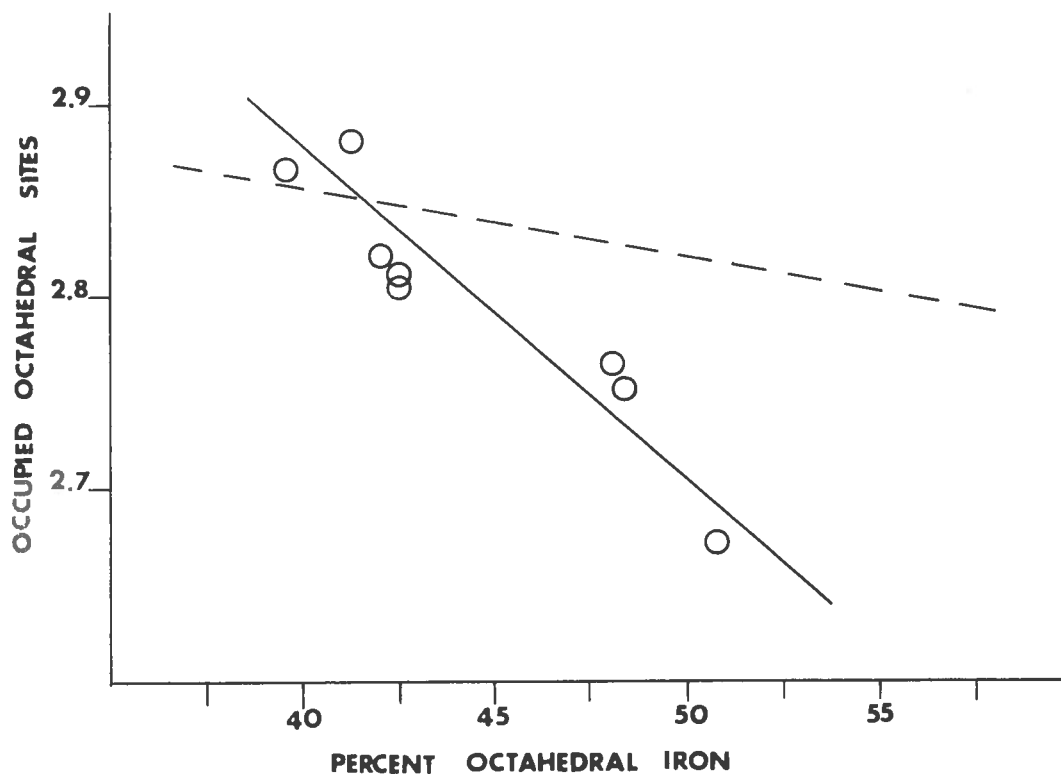


Figure 16. Octahedral vacancies as a function of percent iron calculated in the usual manner (top) and recalculating all ferric as ferrous iron and ignoring H<sub>2</sub>O analysis (bottom). Dashed line is curve assumed by Franzini and Schiafino (1965).

predicted by Franzini and Schiafino (1965, p. 103). This is not surprising, because their assumed values are approximations based on all biotites while the biotites considered here are members of a limited assemblage from one area and are thus of restricted chemical composition.

It is fortunate that the relationship between iron percent of filled octahedral sites and occupied octahedral sites is essentially linear, because only to the extent that these two variables are correlated can the structure-factor ratio method accurately predict percent iron.

Because all but sample 50Y contain carbonaceous matter indicating formation in a reducing environment, the content of  $\text{Fe}_2\text{O}_3$  suggested that some of the samples were weathered (particularly 36Y) in spite of the care taken to avoid this. For this reason the analyses were recalculated assuming an ideal biotite formula and considering all  $\text{Fe}^{3+}$  as  $\text{Fe}^{2+}$  (Table 7). The octahedral occupancy is improved in all cases, but substantial vacancies are still observed. The recalculation also improves the agreement with the curve assumed by Franzini and Schiafino (1965) (Fig. 16, bottom graph) and suggests that some of the apparent vacancies might be explained by weathering.

Octahedral aluminum. The limit of crystalline solubility of Al in phlogopite is reported by Crowley and Roy (1964) as one atom per three octahedral sites. In the eight analyzed biotites from the Orange area the content of Al ranges from 0.385 to 0.468 atoms per three octahedral sites. The extra octahedral aluminum is probably the result of some combination of three coupled substitutions:  $\text{K (Fe, Mg)} = \text{Al}^{3+}; 3 (\text{Fe, Mg})$

$= 2\text{Al}^{3+}$ ;  $(\text{Mg}, \text{Fe})^{2+} \text{Si}^{4+} = \text{Al}^{3+}\text{Al}^{3+}$  (Wones, 1967, p. 58). The first substitution produces interlayer vacancies and increases the octahedral Al content. The second substitution produces octahedral vacancies and increases the octahedral Al content. According to Wones (1967) this is the substitution that best explains octahedral vacancies. The third substitution would increase both the octahedral and tetrahedral Al, without producing any vacancies. This substitution produces siderophyllite from annite and eastonite from phlogopite (Winchell and Winchell, 1951).

These three substitutions can be evaluated graphically by plotting octahedral vacancy vs. Si deficiency vs. interlayer vacancy (Fig. 17). The compositions of the biotites with respect to these Al variations are indicated in the figure. Some of the octahedral charge deficit may be made up by  $\text{Fe}^{3+}$  or  $\text{Ti}^{4+}$ , as well as by  $\text{Al}^{3+}$ . There seems to be some correlation between octahedral Al and octahedral vacancies, (Table 7) when analyses are calculated on an anhydrous basis.

It is interesting to note that the composition assumed by Robinson (1963) with respect to the third substitution is very close to the right one. The effect of the other substitutions on refractive index measurements is unknown. It can fairly safely be assumed that the second substitution will lower the index, however, even if part of the trivalent cations are  $\text{Fe}^{3+}$ , because of the production of an octahedral vacancy. As discussed above, this substitution will also lower  $F_{004}/F_{005}$ .

Ferric/ferrous ratio. An average of 9.6 percent of the iron in the specimens analyzed is in the ferric state, with a range from 6.4 to

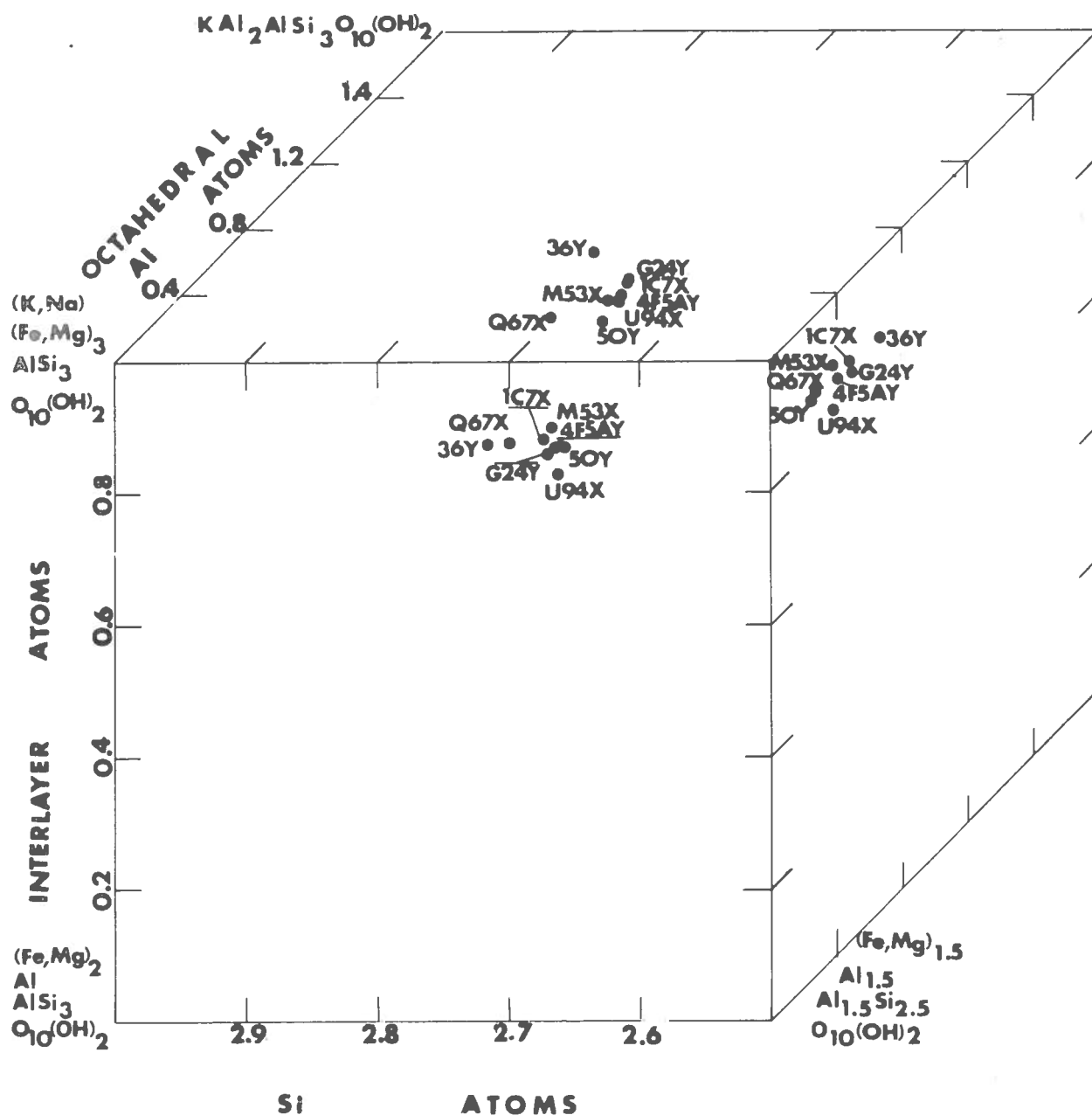


Figure 17. Ranges in octahedral aluminum composition due to the three substitutions explained in the text.

13.0 percent. Considering the difficulty in obtaining accurate  $\text{Fe}^{3+}$  percentages during analysis, there is some doubt whether the range is significant, reflects only the analysis error, or reflects different degrees of weathering. This is especially true considering the fact that all analyses showed C. Only two of the specimens, M53X and 36Y, have enough difference in ferric/ferrous ratio to have been considered different in the groupings by Phinney (1963). Neither one is very anomalous, however, and neither contains anomalously low or high C contents.

A comparison of ferric/ferrous ratio with percent total iron shows weak linearity (Fig. 18). A similar positive correlation was found by Chinner (1960), Peikert (1963), and Hounslow and Moore (1967).

Ti content. It is uncertain whether the Ti in the biotites is in the 3+ or 4+ state. The 4+ state is assumed for lack of data, in accord with common practice in the literature for purposes of calculation of atomic ratios. Ti is almost as important an octahedral constituent as is  $\text{Fe}^{3+}$ , but the two bear only a weak linear relationship to one another (Fig. 19). The Ti content does not seem to be a simple function of iron percent. Sample 36Y is anomalously high in Ti (as well as  $\text{Fe}^{3+}$ ), but the range in Ti content over the samples is even more restricted than the range in  $\text{Fe}^{3+}$  content. 36Y may be anomalous because of a higher proportion of ilmenite inclusions, but the Ti and  $\text{Fe}^{3+}$  may also reflect differences in bulk composition, retrograding, or weathering.

If all the  $\text{TiO}_2$  in the chemical analyses is assumed to be combined with  $\text{FeO}$ , the volume percent of ilmenite inclusions that would result can

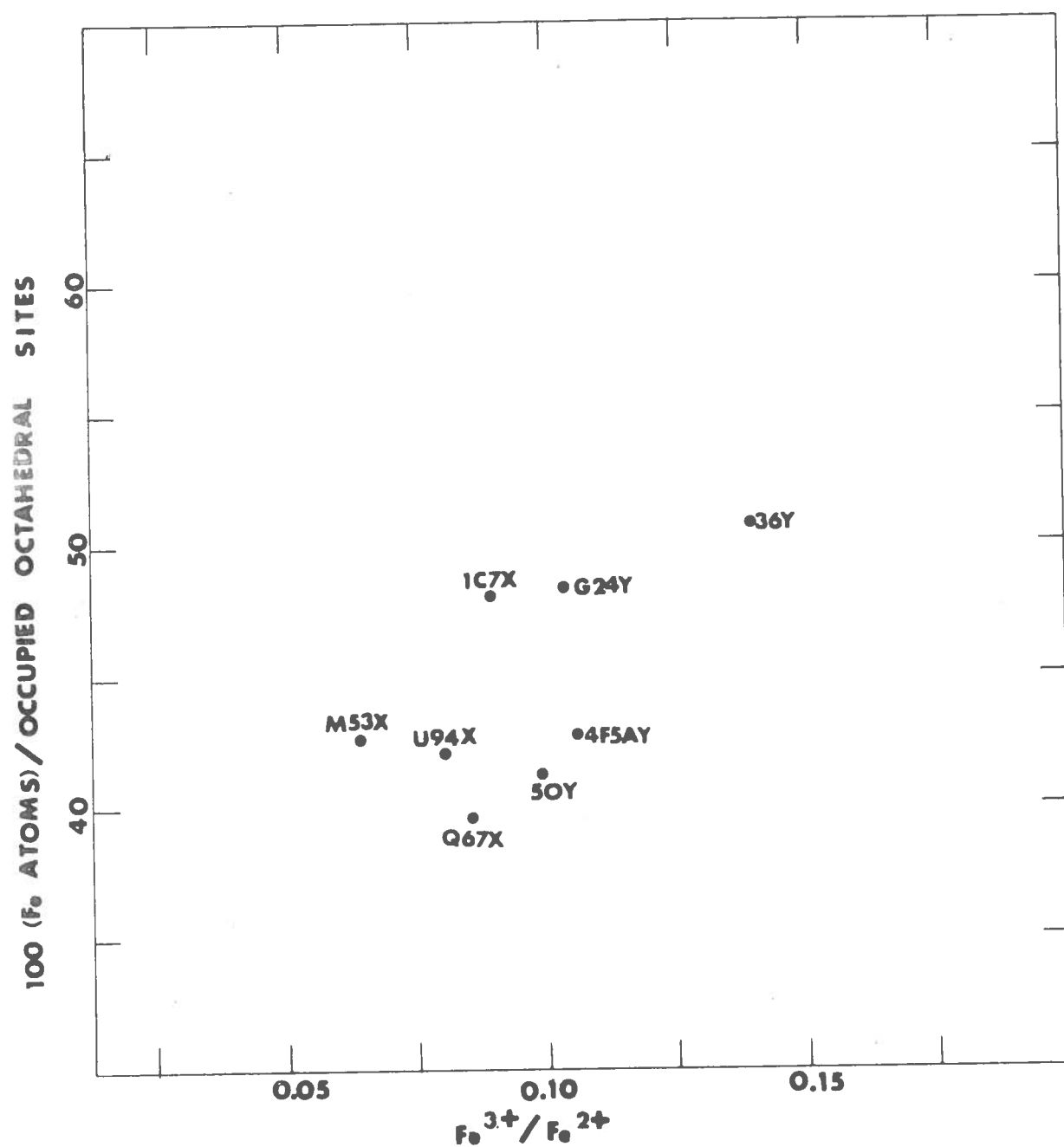


Figure 18. Ferric/ferrous ratio as a function of percent total iron.

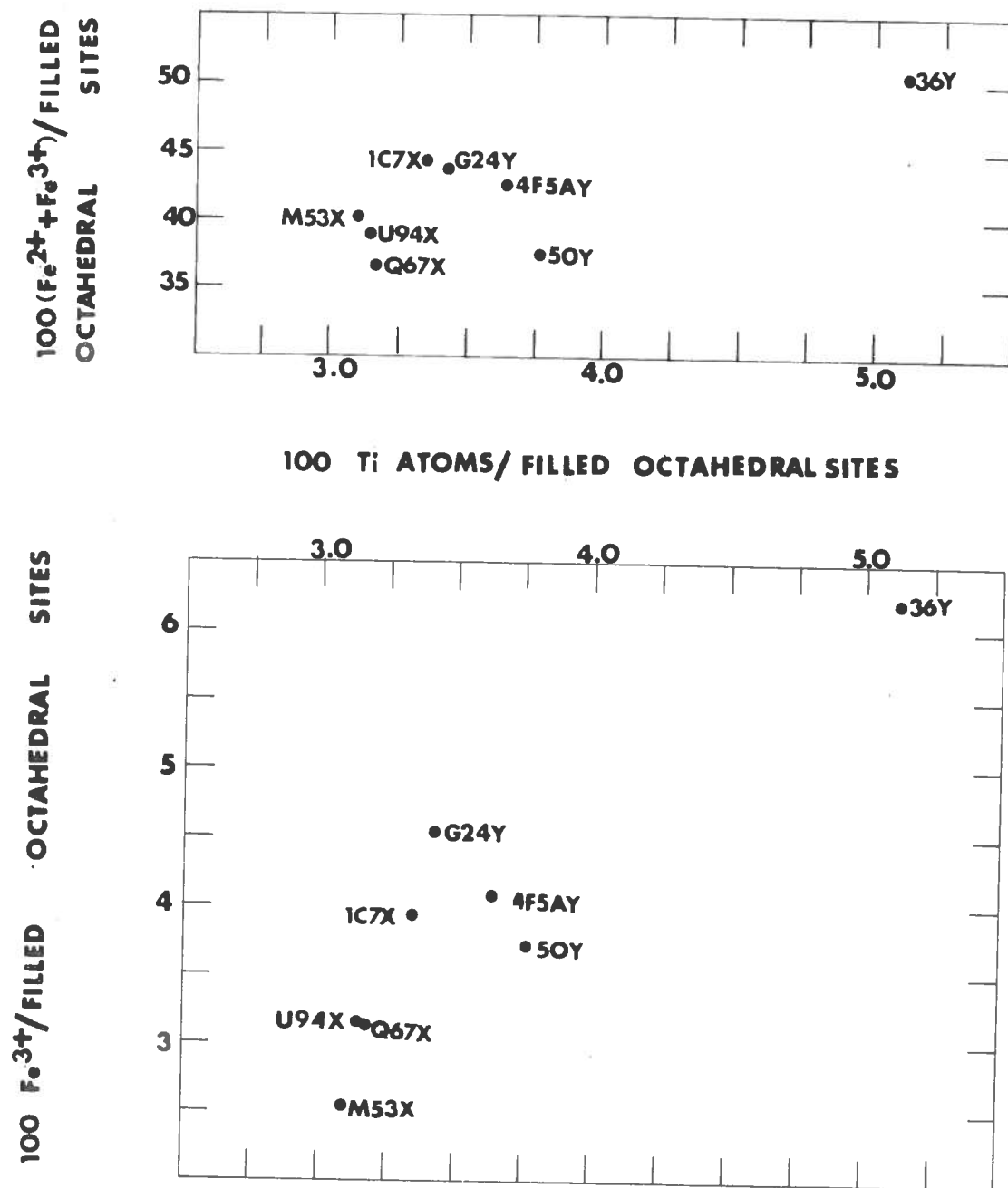


Figure 19. Comparison of percent of filled octahedral sites occupied by Ti with amounts of ferric and total iron.



be calculated (Table 8, column 6). It can be seen that although in some samples (4F5AY, U94X, and G24Y) there is more estimated impurity than calculated ilmenite, in other samples the additional  $\text{TiO}_2$  must be in the biotite itself. If the assumption is made that all the  $\text{TiO}_2$  is combined with  $\text{Fe}_2\text{O}_3$  in hemo-ilmenite inclusions (Table 8, column 6), then the calculated value of mole-percent  $\text{FeTiO}_3$  is much too low for the probable temperatures and oxygen fugacities of the Orange area (Robinson, 1963; Lindsley, 1965), unless such ilmenite has subsequently been weathered. When the chemical analyses for carbon are converted into volume-percent graphite (Table 8, column 3), the volume percents are always much lower than the point-counted impurities (Table 8, column 1). It seems most likely that the grain-counting method overemphasizes the impurity of the specimens, that most of the inclusions are graphite, and that the bulk of the  $\text{TiO}_2$  is in the biotite structure itself.

Mn content. The Mn content is almost negligible in the biotites and amounts to only 0.1 percent of the octahedral atoms. Variations are so small as to be almost beyond the limits of detection of wet chemical analysis. Such Mn as exists in the rock is thus almost wholly tied up in garnet (Pl. 2), unless significant amounts of Mn also exist in the staurolite. This is not probable, however, as Hounslow and Moore (1967) concluded on the basis of 35 staurolite analyses from the literature that Mn in staurolites is always less than 5 mole percent Mn end member, and is usually considerably less.

K/Na ratio. There is a small range in  $100 \text{ Na}/(\text{Na}+\text{K})$  from 4.4 to 7.2, but this is apparently not reflected in the  $d_{001}$  spacings (Fig. 20).

Table 8. Calculated volume percent of graphite and ilmenite.

Sample	1* Volume percent Impurities	2 Weight percent Carbon	3 Volume percent Graphite	4 Weight percent TiO <sub>2</sub>	5 Volume percent Ilmenite	6 Percent FeTiO <sub>3</sub> in Hemo- ilmenite**
4F5AY	1.29	0.12	0.16	1.82	1.18	0.64
50Y	0.52	0.07	0.09	1.94	1.25	0.67
U94X	1.58	0.09	0.12	1.59	1.03	0.67
36Y	0.61	0.06	0.08	2.43	1.60	0.62
M53X	0.28	0.12	0.16	1.55	1.00	0.71
G24Y	1.47	0.03	0.04	1.67	1.09	0.60
1C7X	0.12	0.19	0.26	1.63	1.07	0.63
Q67X	0.04	0.05	0.07	1.62	1.04	0.67

Values used in calculations as follows:

	Molar volume, cc	Molecular weight, g
biotite	$4.66 (\text{Fe}/\text{Fe} + \text{Mg}) + 149.66$	$94.59 (\text{Fe}/\text{Fe} + \text{Mg}) + 417.32$
ilmenite	31.95	151.75
graphite	5.298	12.011

Source: Robie and Waldbaum (1968)  
Troger (1956) for density  
of ilmenite.

\*These are the values in Table 4, column C, subtracted from 100.

\*\*This is the calculated mole percent FeTiO<sub>3</sub> on the assumption that all Fe<sub>2</sub>O<sub>3</sub> is combined with all TiO<sub>2</sub> in a hemo-ilmenite.

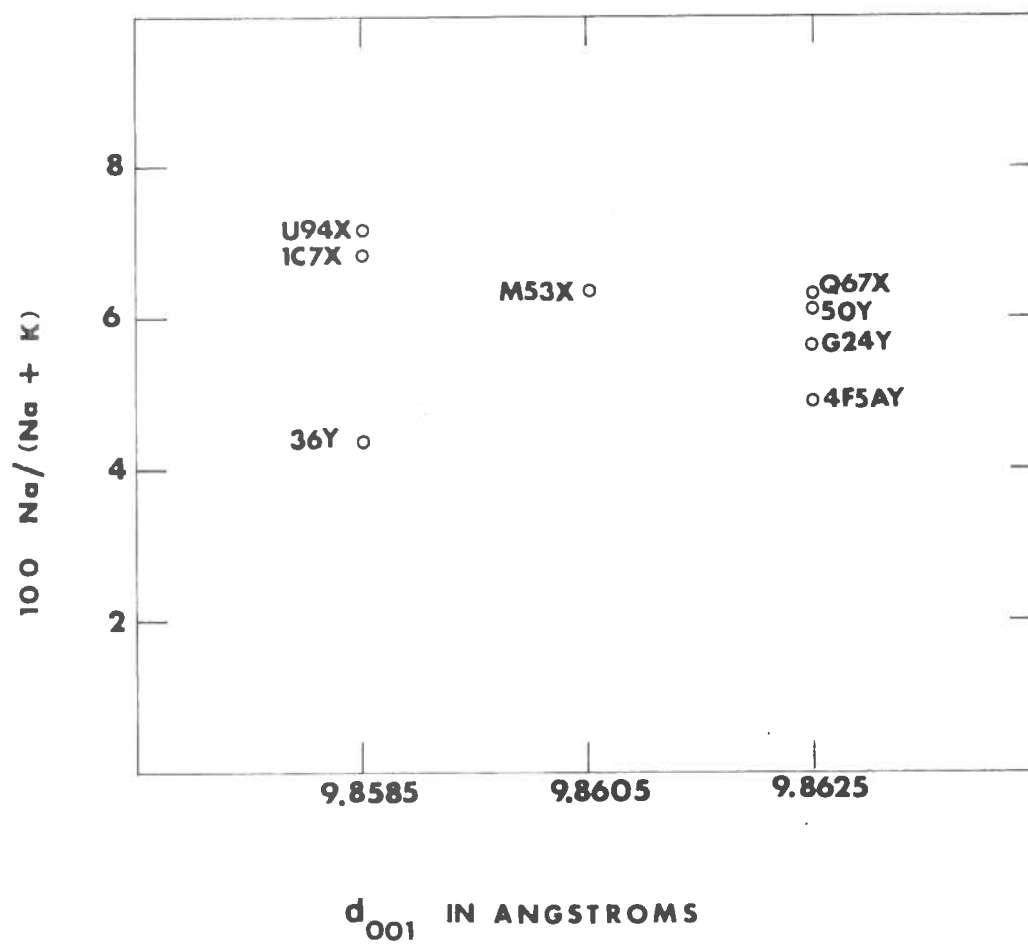


Figure 20. Sodium content of biotites as a function of basal d-spacing.

Either the variation is too small to be measurable by the X-ray method or the d-spacings do not bear a simple relationship to the amount of interlayer Na substitution. This confirms the results of Rutherford (1969, p. 384), who found no measurable shift in d-spacing in synthetic biotites with up to 20 mole percent Na biotite.

Since basal d-spacing data on coexisting muscovites and biotites were available, a plot was made of the  $\text{Na}/(\text{Na} + \text{K})$  ratio in muscovites and biotites (Fig. 21). The muscovite  $\text{K}/(\text{Na} + \text{K})$  ratio was determined by extrapolation of the curve of Evans and Guidotti (1966, p. 39). The biotites all contain significantly less Na than the coexisting muscovites. There is a fairly regular fractionation between the muscovites and biotites.

Octahedral Fe. At least 95 percent of the occupied octahedral sites can be expressed in terms of Fe, Mg, and Al. Recalculation to 100 percent and plotting on a triangular diagram (Fig. 22) shows that the major variation in the octahedral layer is in the ratio of Fe/Mg. Thus the percent iron or the ratio  $\text{Fe}^{3+} + \text{Fe}^{2+} / (\text{filled octahedral sites})$  is the most important single variable, as well as the most easily measured. The range of octahedral iron is from 1.186 to 1.353 atoms per 3.000 octahedral sites or from 39.5 to 50.7 percent of the filled octahedral sites.

The Ti content is not included in the ratio because the valence is not known and ionic substitutions such as proposed by Franzini and Schiafino (1965), which would class  $\text{Ti}^{4+}$  as a light atom, are not easily evaluated. In fact, Wones (1967, p. 60) disagrees with Franzini and

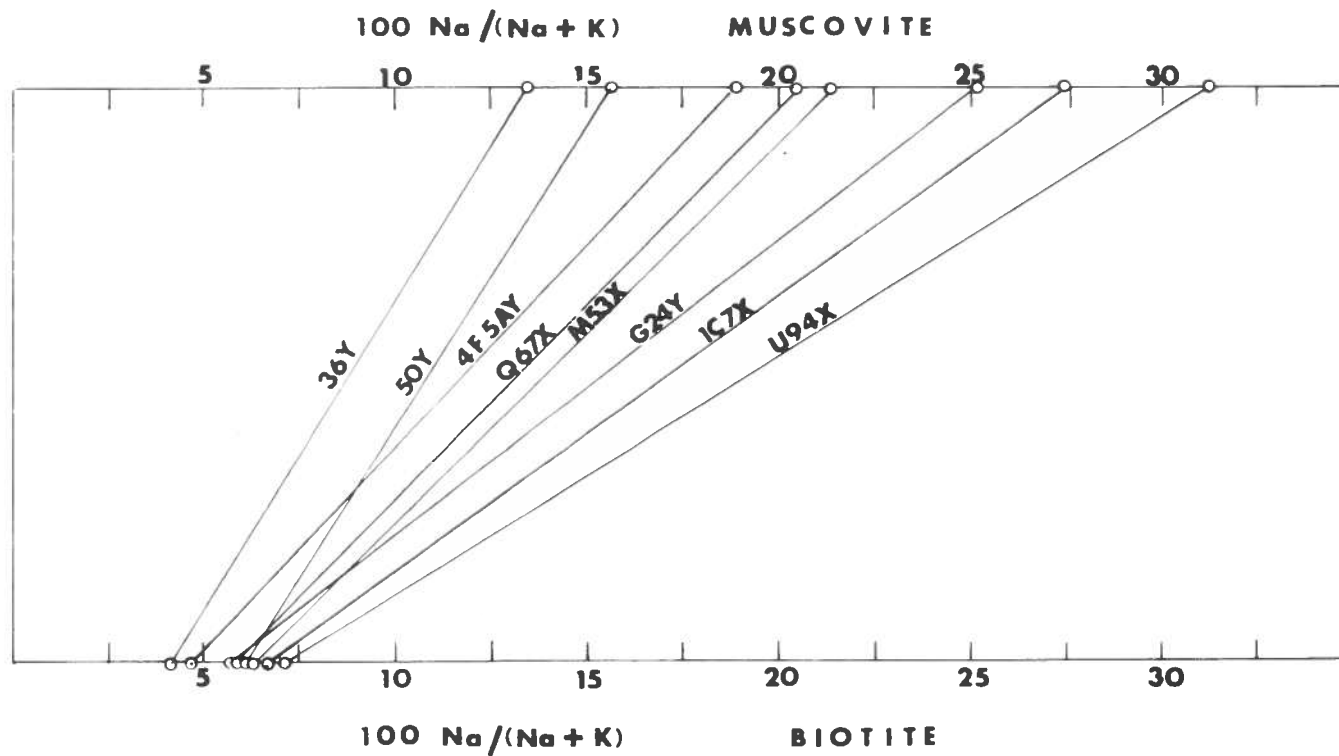


Figure 21. Comparison of Na/K ratio of coexisting biotites and muscovites. Muscovite data by Ahmad (oral comm., 1969). (See Table 3).

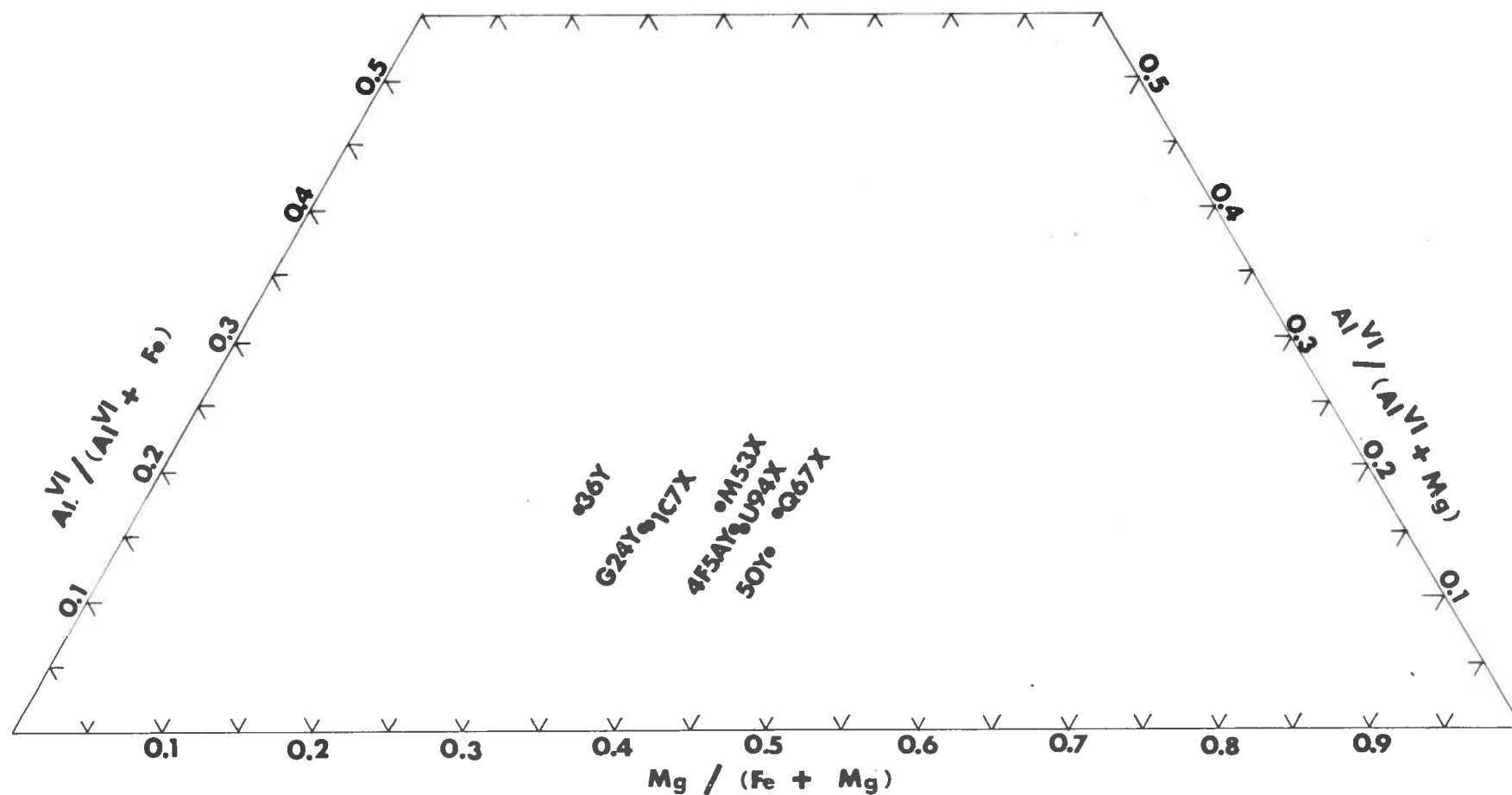


Figure 22. Relative variation in octahedral Al, Fe, and Mg in analyzed biotites. The main variation is in Fe/Mg, but a small variation also exists in Al/Fe + Mg.

Schiafino (1965, p. 105) on the likely valence of titanium. Since titanium accounts for no more than 5 percent of the octahedral sites, and the maximum variation in titanium is 2.0 percent, even a small error would be relatively constant and included in the scatter on the calibration curve.

#### Comparison of X-ray method with wet-chemical analyses

It is believed that seven of these eight biotites are a representative sample of the biotites in assemblage 2 in the Orange area (U94X is in assemblage 1), and that the compositions of other specimens are not likely to vary much from the compositional ranges of the specimens analyzed. This is the assumption behind the calibration curve used to extend these compositional results to the rest of the population.

The results of the chemical analyses were used to calibrate the X-ray method by plotting iron percent of filled octahedral sites vs. measured structure-factor ratios (Fig. 23). Four more analyzed biotites were kindly lent by Dr. J. B. Lyons of Dartmouth College for use in calibration. These analyses, computed atomic ratios, and structure-factor ratios are given in Appendix 2.

It can be seen from the plot that all biotites from the Orange area and two of the other four biotites plot close to a straight line of steep slope. The line drawn represents the mean of the two regression lines computed as least squares using these ten biotites. The standard deviation of the ten biotites is 1.7 percent iron, and none is farther off the line than 3.0 percent iron. It can thus be concluded that the

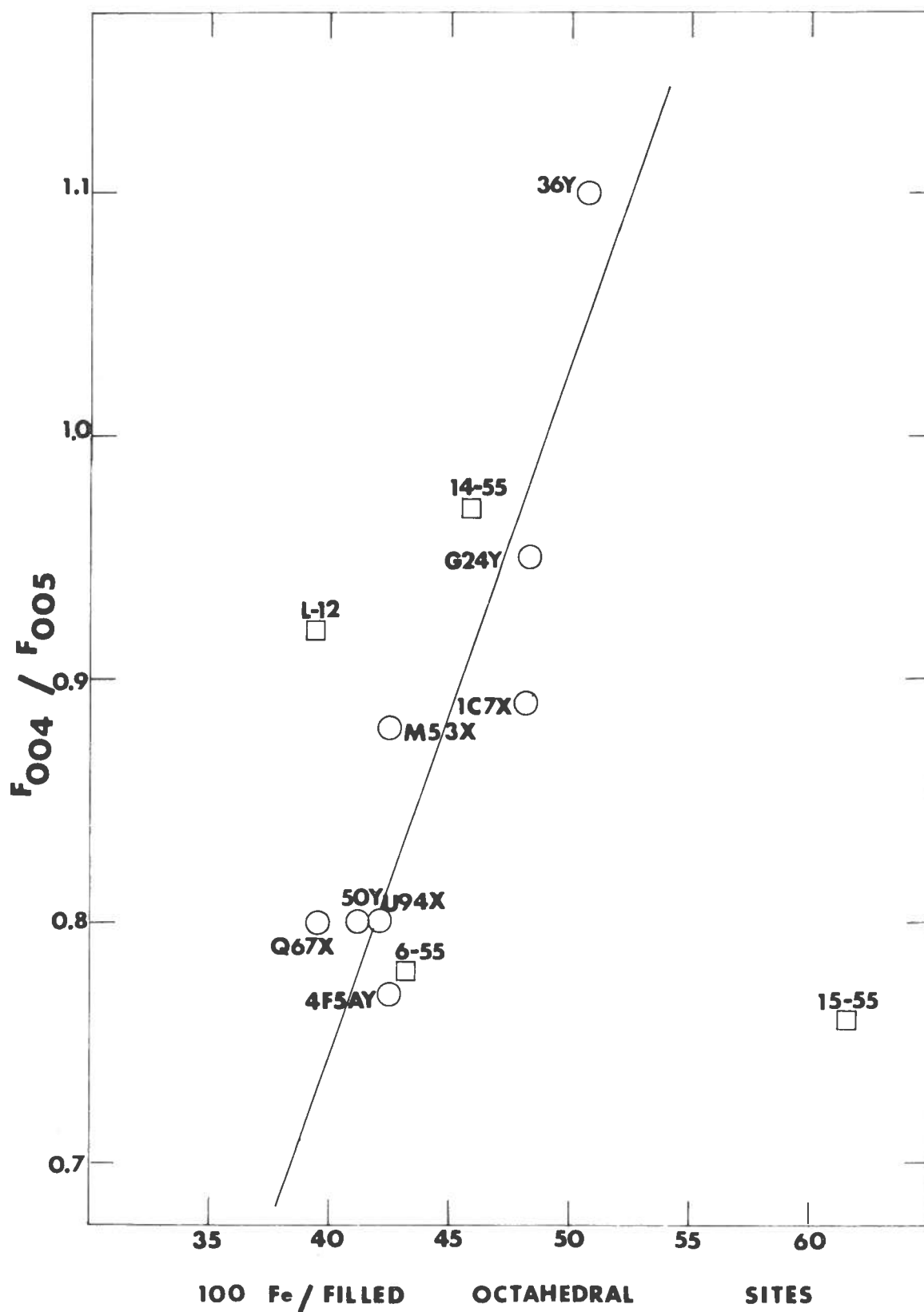


Figure 23. Calibration curve for X-ray determinative method of biotites. Squares are Dartmouth samples; circles are samples analyzed from the Orange area.



measurement of structure-factor ratios of the biotites in the Orange area in the critical assemblage is a reliable predictor of percent octahedral iron, to about 2 percent Fe, in spite of the problems of variations in octahedral vacancy and Ti, interlayer, and tetrahedral substitutions.

Sample 15-55 falls off the calibration curve because it has chlorite in it. The analysis is low in potassium and high in water. It is not known why sample L-12 falls so far off the calibration curve. It is very low in iron and high in aluminum. The accuracy of the analyses of the Dartmouth samples is not known, and the assemblages are different. It should be emphasized that this calibration curve (Fig. 23) is probably only reliable for biotites of composition similar to those from assemblage 2 in the Orange area, and could not be safely applied to other samples.

#### Comparison of refractive indices with wet-chemical analyses

The beta  $\approx$  gamma refractive indices of the eight analyzed biotites are plotted as a function of Fe percent of occupied octahedral sites in Figure 24. The lower plot shows refractive indices of biotites from the same locations as the analyzed biotites (but not the identical specimens) measured by Robinson (1963). Both plots are linear, but the scatter is large and a line cannot be drawn which is everywhere 3 percent Fe or less from the data points. Neither curve agrees with Winchell and Winchell's (1951) curve for biotites with one-third extra octahedral Al, but they did not take octahedral vacancies into account. It is interesting to note, however, that Winchell and Winchell's (1951) curve is intermediate between the other two curves. This suggests that Robinson (1963) and Hall (this work) may have systematic errors in opposite directions. The author

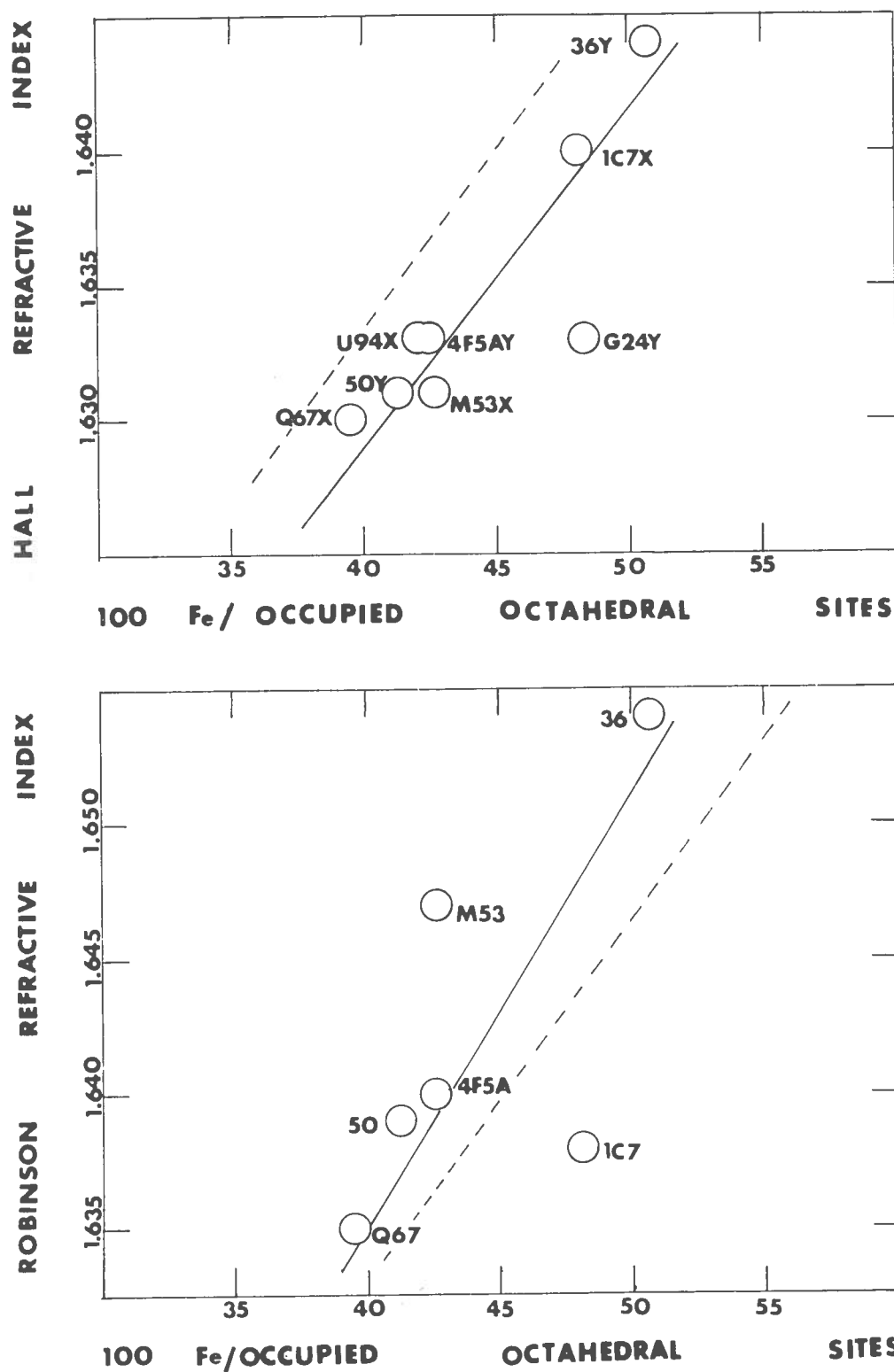


Figure 24. Comparison of beta (gamma) refractive indices of biotites measured by Hall (above) and Robinson (below) with analyses. Robinson's samples are from the same location and assemblage as analyzed biotites, but are not identical specimens. Dashed line is curve of Winchell and Winchell (1951) for biotites with 1/3 extra octahedral Al.

believes that his generally low results are due to readings taken on partially curled edges. On such a grain the index would be intermediate between gamma and alpha, and hence would read lower in most orientations.

Considering the lack of reproducibility and the scatter, it is believed that the optical-index method represents a crude measure of relative percent iron. The structure-factor ratio method is preferred, however, for both its accuracy and its objectivity.

#### Results of X-ray measurements of biotite compositions calibrated by analyzed standards

Using the calibration curve (Fig. 23), percent octahedral Fe was determined for the 27 other biotites listed in Table 2. The experimental data and octahedral Fe are presented in Table 9.

Some measure of the reliability of the X-ray results is given in Table 9 in the column headed Relative 004 Peak Intensity. The units are arbitrary, but are a measure of the area under the peak, excluding the background. A peak with an intensity of greater than 100 is considered to have a moderate peak/background ratio, one with an intensity less than 100 a low peak/background ratio, and one with an intensity greater than 200 a high peak/background ratio. The variation is always observed to occur in pairs. That is, low 004 peaks are associated with low 005 peaks. The ratio of intensities is not affected. The problem with low peaks lies in picking the crest for the LP factor and the relatively more important choice of background level.

Table 9. X-ray data on biotites.

Formation	Assemblage	Sample	$F_{004}/F_{005}$	Relative 004 Peak Intensity	Percent Fe of Occupied Octahedra
Partridge	2)	1F8A	0.86	173.9	44
	2)	4F5AY	0.77	145.5	42.5
	2)	36Y	1.10	108.0	50.7
	2)	891A	0.92	88.2	46
Clough	2)	418A	1.03	436.8	50
Littleton, Kyanite Zone	1)	464	0.93	78.2	46
	1)	233	0.82	166.0	43
	1)	L10	0.98	48.1	48
	1)	828	0.88	104.8	45
	1)	908	0.94	291.5	47
	1)	836	0.93	168.5	46
	1)	239B	0.88	93.7	45
	1)	796B	0.90	311.4	45
	1)	529A	0.92	135.1	46
	1)	U94X	0.80	185.4	42.1
	*)	13	0.94	179.6	47
	1)	558C	0.96	124.0	47
Littleton, Lower Sillimanite Zone	2)	131A	0.78	175.1	42
	2)	314	0.99	67.7	48
	2)	M53X	0.88	176.2	42.6
	2)	6D6	0.98	364.0	48
	2)	B06	0.93	138.8	46
Littleton, Higher Sillimanite Zone	2)	A23	0.95	129.3	47
	2)	G23	0.89	122.3	45
	2)	G24Y	0.95	138.6	48.3
	2)	A76A	0.89	60.9	45
	2)	1C7X	0.89	107.2	48.1
	2)	7B9	0.98	280.2	48
	2)	680	1.00	84.5	49
	2)	Q67X	0.80	86.1	39.5
Erving, Kyanite Zone	2)	X77D	0.79	148.5	42
	2)	230	0.86	82.9	44
	2)	50A	0.82	270.8	43
	2)	50Y	0.80	119.8	41.2

\*Assemblage quartz-muscovite-biotite-garnet.

It is believed that the main cause of variation from one sample to another is in the preparation of the smear mount. Thick, well-ground samples with minimum surface roughness produce the most intense peaks and hence the most reliable results.

## GARNETS

### Measurement of compositional zoning by milliprobe X-ray fluorescence

Semiquantitative X-ray fluorescence procedures were used to gain compositional information on eight coarse-grained garnets from six localities. The specimens were analyzed for Fe and Mn by means of milliprobe X-ray fluorescence at points along a traverse through the approximate center of the crystal, in order to determine the nature and extent of garnet compositional zoning.

Specimens 36 and 50A were analyzed in sawed rock slices. The other six specimens were separated and mounted in a transparent acrylic Bakelite medium by means of a hydraulic press. Bakelite is preferred because it shows no Fe or Mn above the level of background. Also, since the medium is transparent, the center of the crystal can be determined easily and with some accuracy.

The garnets showed euhedral dodecahedral crystal form and rested on one of the diamond-shaped faces during mounting in the Bakelite. The center of the garnet was taken to lie in the plane which came closest to dividing the vertical (011) faces into two equal halves. The garnets in the Bakelite were sawed close to this plane and then ground down the

rest of the way. All garnets were first visually inspected with the binocular microscope and positioned in the milliprobe holder so as to minimize cracks, inclusions, and roughness in the path of the traverse.

An assortment of beam-collimating slits was tried with varying success. The best slit for the purpose was made from the cylindrical tip of a hypodermic needle of 0.5 mm diameter, packed in a commercial 1 mm collimating slit by means of lead foil. Both the Fe and Mn readings were made using Cr radiation and an LiF analyzing crystal. The X-ray tube was operated at 49 kilovolts and 49 milliamperes. The counter tube voltage was kept at 1.55 kilovolts. All the calibration standards and all the garnets were run under conditions as similar as possible except that garnet 36, run during the beginning of the determinations, was run with a 1 mm collimating slit.

It was empirically determined that 100-second counts for Mn and 10-second counts for Fe were sufficient to establish reproducible results with moderate peak/background ratio. Complete scans were made across the garnets through the centers. At 0.1 mm intervals, counts were made of both FeK and MnK radiation. From these counts background levels as determined by readings on the Bakelite were subtracted. The resulting data were plotted as counts vs. distance (Pl. 2).

Six analyzed standards (Table 10) were used to compute calibration curves for Fe and Mn. In addition, electron-microprobe analyses by W. Trzcienski on some of the same garnet specimens were used (Table 11). For the mineral standards other than garnet, the Fe and Mn contents were

Table 10. Counting statistics and analyses of garnet standards.

1725		T59B		1553		7A8B		Y42B	Rhod
CPSMn	CPSFe	CPSMn	CPSFe	CPSMn	CPSFe	CPSMn	CPSFe	CPSMn	CPSMn
1.5	123	3.9	106	2.3	128	2.2	112	1.8	157
1.7	118	3.8	111	2.2	136	1.8	114	2.0	163
1.6	127	4.0	109	2.1	137	1.5	114	1.9	156
1.7	116	3.6	108	2.0	132	1.8	110	1.7	165
1.8	123	4.0	107	2.1	124	1.9	116	1.9	164
1.6	118	3.6	104	2.0	123	1.6	108	1.8	155
1.6	116	3.8	109	1.9	127	1.5	110	1.9	155
1.7	123	4.0	105	1.8	128	1.6	108	1.8	168
1.7	120	3.5	114	1.7	125	1.8	107	1.6	165
1.6	125	3.8	108	1.6	120	2.2	103	2.3	161
Ave 1.64	121	3.8	108	1.97	128	1.79	111	1.87	161

## Analyses in Weight Percent\*

	1725	T59B	1553	7A8B	Y42B	Rhod
SiO <sub>2</sub>	40.01	49.0	39.62	44.1	50.8	
Al <sub>2</sub> O <sub>3</sub>	21.80	8.4	22.00	12.0	3.8	
FeO	19.99	19.5	19.61	20.2	26.3	
MnO	0.28	1.2	0.30	0.3	0.5	60.1
MgO	12.72	17.4	12.78	9.3	15.3	
CaO	3.67	0.7	3.79	9.0	0.0	
Na <sub>2</sub> O	--	0.8	--	1.9	0.4	
Density g/cc**	3.85	3.24	3.85	3.31	3.32	3.60
Moles MnO/ 1000 cc	1.54	5.47	1.54	1.32	2.32	306
Moles FeO/ 1000 cc	107.0	87.7	105.1	93.0	121.5	

\*Analyses from following sources:

1725 - garnet (H. H. Schmidt, eclogite, Norway)  
 1553 - garnet (H. H. Schmidt, eclogite, Norway)  
 Rhodochrosite - (H. W. Jaffe, partial analysis)  
 Y42B - anthophyllite (C. Klein, microprobe analysis)  
 T59B - anthophyllite (C. Klein, microprobe analysis)  
 7A8B - hornblende (C. Klein, microprobe analysis)

\*\*Densities from Deer, Howie and Zussman (1965), p. 28 for garnets, p. 171 for hornblende; Troger (1956), p. 71 for anthophyllites; Winchell and Winchell (1951), p. 108 for rhodochrosite.

Table 11. Composition of zoned garnets by electron microprobe.

(Analyses by W. Trzcienski)

	50ABR*	50ABM*	50ABC*	908AR	908AC	680R	680M	680C
SiO <sub>2</sub>	34.92	34.46	35.10	37.18	35.98	35.76	35.03	35.81
Al <sub>2</sub> O <sub>3</sub>	20.26	20.76	20.57	21.83	19.89	21.50	20.71	21.02
FeO	40.65	40.10	39.76	37.41	33.11	34.08	34.90	34.34
MnO	0.31	0.71	0.96	0.21	3.71	0.25	0.93	1.84
MgO	1.84	1.29	1.14	2.81	1.55	2.63	1.96	2.59
CaO	0.37	0.79	1.21	0.54	2.00	2.58	2.75	0.78
Total	98.35	98.11	98.72	99.98	96.24	96.79	96.27	96.37
Mole Percent Alman- dine	90.91	90.87	89.73	86.36	78.48	80.52	81.44	82.12
Spess- artine	0.70	1.63	2.19	0.49	8.90	0.60	2.20	4.45
Gross- ular	1.06	2.29	3.50	1.60	6.07	7.81	8.22	2.39
Pyrope	7.33	5.21	4.58	11.56	6.54	11.07	8.15	11.04

\*R = Rim of the garnet

M = Approximately 1/2 the distance between R and C

C = Core of the garnet



recomputed to moles  $\text{FeO}/10^4$  cc mineral and moles  $\text{MnO}/10^4$  cc mineral using the densities listed in Table 10. These values were then plotted against counts/second FeK and counts/second MnK. The moles/volume scales were recomputed to mole percent almandine and mole percent spessartine.

Linearity in the Mn calibration plot is quite good and the intercept is near zero (Fig. 25). Much more scatter is evident in the Fe calibration curve (Fig. 26), and the intercept is not at zero. The reason for this is not clear. It is possible that for major components (greater than 50 mole percent) absorption effects become important and the relationship is not linear but exponential. A calibration curve has been drawn for the Fe points but without a great deal of confidence.

Absolute almandine contents as read off the curve are probably only good to within 5 or more mole percent almandine. Absolute spessartine contents are probably good to within 1 or 2 mole percent spessartine. Relative variations (as in a single zoned crystal) are probably more accurate, because small changes in slope result from large changes in absolute values for the standards and the errors in density assumptions and chemical analyses would not be so serious.

#### Composition of zoned garnets

At least a suggestion of Fe/Mn zoning is present in all ten specimens, but it varies considerably in degree (Pl. 2). The most common result is an Mn-rich, Fe-poor center varying more or less regularly to Fe-rich, Mn-poor edges. The garnets vary dramatically in composition from one specimen to another.

Specimens 908A, 908B and 908C are three garnets from the same hand

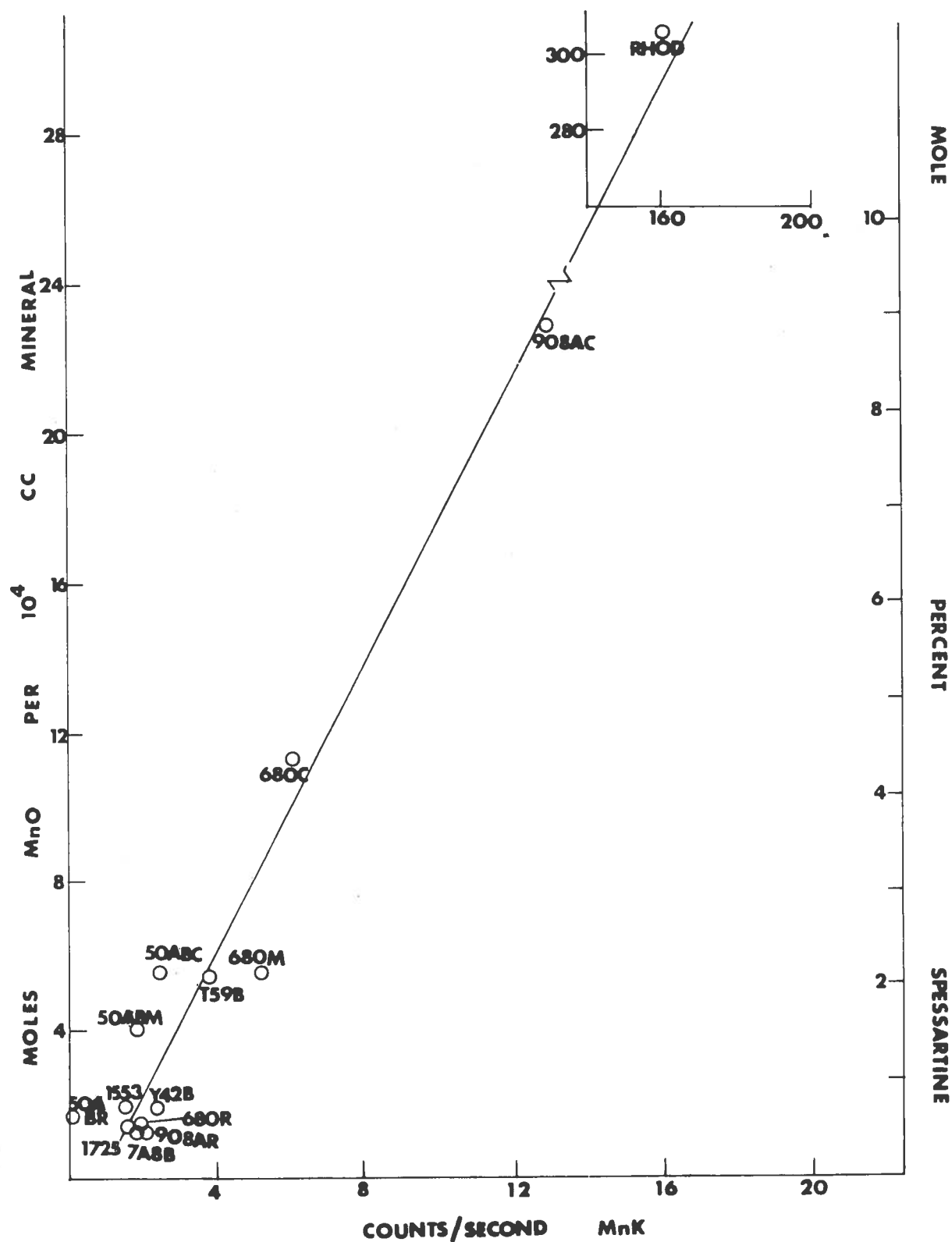


Figure 25. Calibration curve for X-ray fluorescence determination of mole percent spessartine in garnet. Samples are numbered as in Tables 10 and 11.

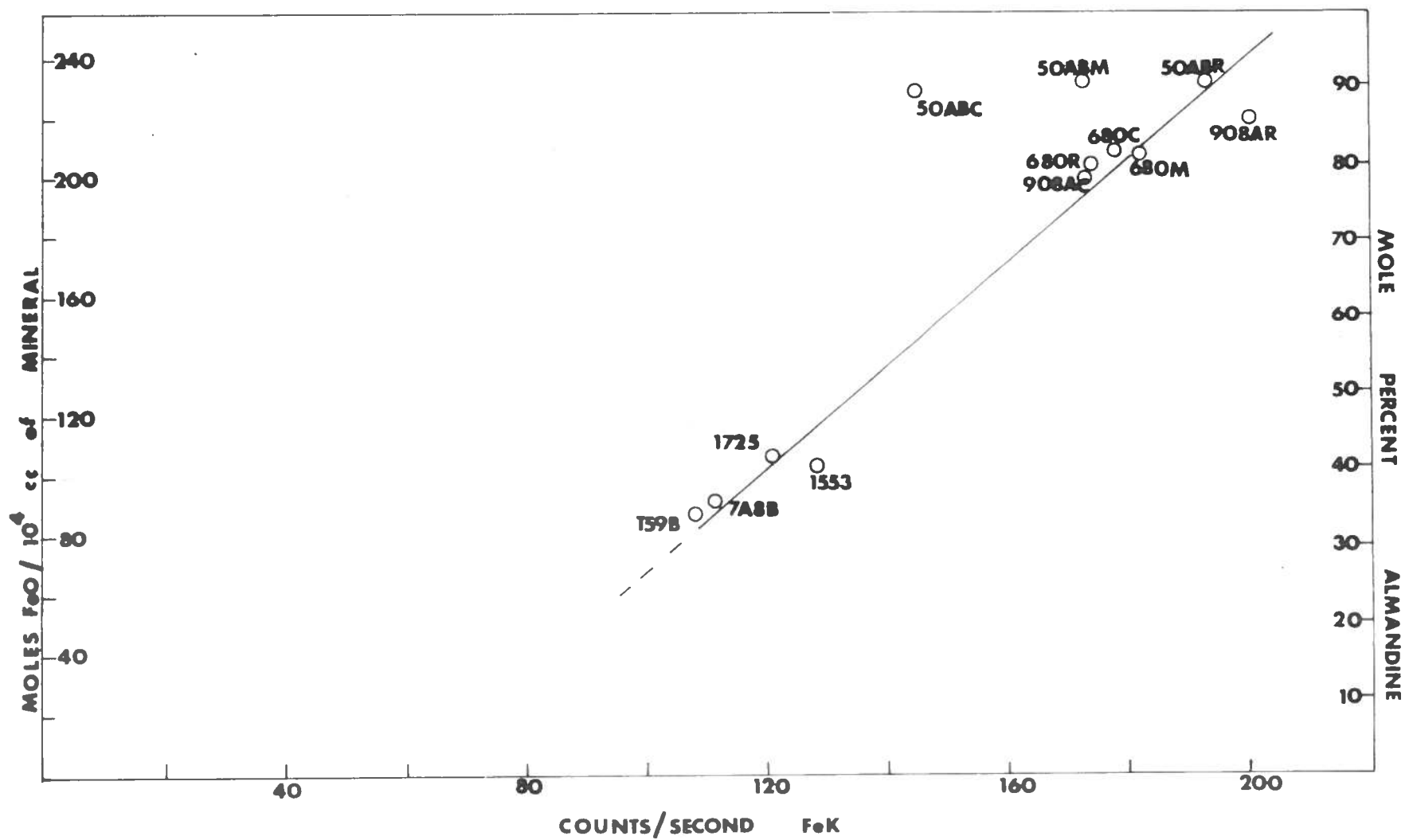


Figure 26. Calibration curve for X-ray fluorescence determination of mole percent almandine in garnet. Sample numbers are explained in Tables 10 and 11.

specimen in assemblage 1. The center compositions have a mean of approximately 78 mole percent almandine and 9.1 mole percent spessartine with ranges from 72 to 80 and 8.3 to 9.8 respectively. The edge compositions have a mean of approximately 94 mole percent almandine and 0.9 mole percent spessartine, with a range from 91 to 99 and 0.8 to 1.0 respectively. All these garnets show excellent compositional zoning, with the typical bell-shaped Mn-curve and corresponding Fe-low characteristic of zoned garnet profiles (Hollister, 1966).

Specimen 50A shows good zoning in the Fe profile, but the Mn peak is displaced from the center. This may be partly due to the influence of the surrounding minerals, as this specimen was analyzed in a sawed rock slice and the thickness of the garnet was unknown. The medium at the left side of the profile was higher in Fe than the medium at the right side so that the profile does not appear symmetrical. The center composition is 34 mole percent almandine and 8.8 mole percent spessartine. The edge composition is 60 mole percent almandine and 6.3 percent spessartine. The edge compositions are possibly unreliable because of the influence of the minerals in the surrounding rock.

Specimen 50AB is a large garnet from the same rock as 50A, but mounted in Bakelite. The Mn content is not nearly so high as 50A but good zoning in both Fe and Mn is evident. The center composition is 55 mole percent almandine and 1.3 mole percent spessartine, and the edge composition is 88 mole percent almandine and 0 mole percent spessartine. Both 50A and 50AB have center compositions notably low in almandine,

as indicated by the milliprobe. Microprobe analyses indicate the center compositions are notably high in almandine (Table 11). This single specimen accounts for most of the scatter in the Fe calibration (Fig. 26). There seems to be no good reason to suspect either the milliprobe or the microprobe results and the reason for this discrepancy is still unknown.

Specimen 418C shows very slight Mn zoning and what appears to be a slight reverse zoning in Fe. The center composition is approximately 83 mole percent almandine and 2.8 mole percent spessartine and the edge composition is approximately 75 mole percent almandine and 1.8 mole percent spessartine.

The garnet profile of specimen A76A is obscured by a large quartz inclusion just under the surface that was found after the profile was run. However, a generalized decrease in Fe can still be seen near the right side of the profile. The Mn, if anything, shows a very slight increase, but not more than 0.7 percent. The center composition is very approximately 90 mole percent almandine and 1.2 mole percent spessartine. The edge composition is very approximately 99 mole percent almandine and 0.5 mole percent spessartine.

Specimens 680 and 680R are the same garnet run twice along approximately the same profile to check the reproducibility of the technique. Excellent Mn zoning is present but the Fe profiles are not so clear. A suggestion of reverse Fe zoning can be seen in 680R, and also in 680 if the mean edge composition is used. 680 has a center composition of 80 mole percent almandine and 3.8 mole percent spessartine and an edge composition of very approximately 75 mole percent almandine and 1.0 mole percent

spessartine. 680R has a center composition of 80 mole percent almandine and 4.4 mole percent spessartine and an edge composition of 75 mole percent almandine and 0.5 mole percent spessartine.

Specimen 36 was run using a 1-mm slit so that no absolute compositional data was obtained. There is, however, an indication of zoning in the Fe profile. The 1-mm slit is probably too coarse to make this profile reliable for anything more than a rough indication of trend. The profile for specimen 36 emphasizes the importance of employing a 0.5-mm slit and taking longer counts.

It is interesting to compare the profiles from the milliprobe with those obtained by electron microprobe. Figure 27 illustrates the results in mole percent obtained with the microprobe. The Mn profiles match very closely, with 50AB least well-zoned, 680 moderately well-zoned, and 908A very well-zoned. The absolute spessartine values also agree very closely as expected from the calibration curves. The Fe profiles show agreement as to direction, with 908A and 50AB showing normal zoning and 680 showing reverse zoning, but the milliprobe profiles show a larger range in Fe content. Again the wide discrepancy between milliprobe and microprobe for 50AB is pronounced and not yet understood.

The microprobe values also give results for grossular and pyrope contents. In all the garnets, these profiles are almost mirror images of each other. In 908A and 50AB, the grossular content is higher in the center and decreases toward the edges, and the pyrope content is lower in

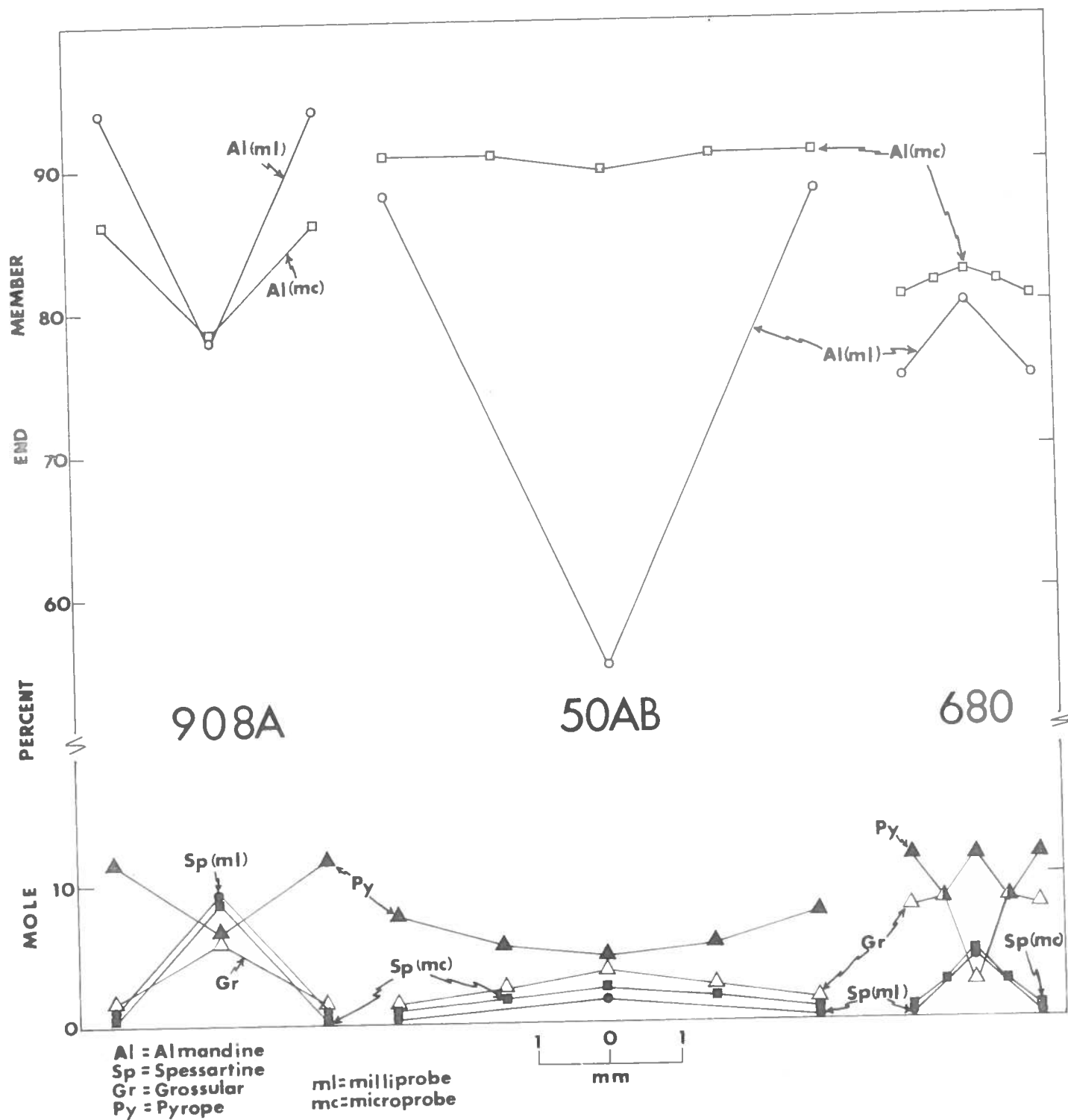


Figure 27. Comparison of fluorescence milliprobe and electron microprobe results on same garnet specimens. Grossular and pyrope contents were analyzed for by microprobe method only. Note broken scale.

the center and increases toward the edges. In 680, however, the grossular content is lowest in the center, increases to the midpoints and decreases at the edges. The pyrope content is highest in the center, decreases to the midpoints and increases to the edges. These are the only reversals encountered in the profiles.



## METAMORPHIC PETROLOGY

Regional variation in octahedral Fe content of biotite

The octahedral Fe contents of the biotites as listed in Table 9 are plotted on Plate 1 and contoured using an interval of two percent. It is felt that using the eight analyzed samples improves the control so that a two percent interval is not an overinterpretation of the data. Thirteen of the samples are not in the critical assemblage but are in assemblage 1 or 3 (Fig. 3). These samples could thus be used to control the contouring, because for given metamorphic conditions the percent Fe must increase in the order 3, 2, 1. A reasonable, smooth pattern with no abrupt gradients was obtained, which increased confidence in the method.

The general results of the contouring are similar to those reported by Robinson (1963), who found a high around West Orange and decreasing refractive indices to the west and northeast. The results of the present analysis show that a second region of high Fe content exists in the northeast. This high has the form of a ridge trending northwest, and may have a smaller arm on the southern flank trending in the same direction. The four specimens analyzed from the general area confirm this result. The causes of this variation in Fe content must involve metamorphic reactions due to changes in conditions of metamorphism.

### Analysis of phase equilibria

A number of researchers have attempted to relate progressive change in chemical composition of minerals to changes in metamorphic grade. Kretz (1959) found an equilibrium distribution of Mg and Mn between garnet and biotite in Grenville gneisses. Engel and Engel (1960) concluded that lines of equal metamorphic grade could readily be drawn upon increments of change of elements or element ratios such as Mn/Fe or Fe/Mg in biotites and garnets of the northwest Adirondacks. Frost (1962) was able to predict metamorphic grade from Fe/Mg distribution coefficients of coexisting garnet-biotite pairs. Turekian and Phinney (1962) were unable either to demonstrate equilibrium distribution of trace elements between garnet-biotite pairs or to predict laws governing trace-element distribution on the basis of a single parameter such as ionic radius. Phinney (1963) also postulated a lack of diffusion equilibrium over distances of a few centimeters to account for crossing tie lines of 23 sets of garnet-biotite pairs. Tie lines were crossed even among groups of pairs with similar Mn content of garnet and  $\text{Fe}^{3+}/\text{Fe}^{2+}$  ratio of biotite. Green (1963) found that Fe/Mg ratios of coexisting almandine, staurolite, and biotite decreased in that order but he was unable to relate compositional changes to relative distance from the staurolite or sillimanite isograd in northern New Hampshire. Albee (1965b) analyzed the distribution of Fe, Mg, and Mn between 70 garnet-biotite pairs and found that the distribution coefficient for

Mg/Fe depends on metamorphic grade, Mn content of garnet, and on the detailed mineral assemblage. Albee (1965c) also noted that the distribution coefficients of each mineral pair for Mn/Mg + Fe are similar within an assemblage. Butler (1967) found an increase of tetrahedral aluminum in biotites from the Moine schists, but no apparent relationship between garnet-biotite pairs with increasing grade.

It is reasonable to conclude that equilibrium may or may not be maintained between garnet-biotite pairs. The zoned garnets in the Orange area prove that equilibrium is not maintained over short distances. If this were not so, the garnets would be homogeneous throughout. This complication, coupled with those caused by reactions occurring outside the system presented on the Thompson Projection, makes analysis of the phase relationships more difficult, because a changing effective bulk composition is involved. Perhaps similar compositional inhomogeneities were involved in some of the above investigations.

The biotite compositions and point-counted modes of the rocks from which the analyzed biotites were obtained can be used to analyze the phase equilibria on the projection developed by Thompson (1957). All assemblages containing quartz and muscovite can be plotted on this projection if additional components (MnO, CaO) are invoked to explain the occurrence of garnet. If the Fe/Mg ratio of the biotites in assemblage 2 increases with increasing grade of metamorphism, the compositions of the biotites plotted on the projection should reflect the increase. As presented in Figures 28-30, biotites from assemblage 2 from the kyanite zone are in fact less Fe-rich than biotites from the sillimanite zone,

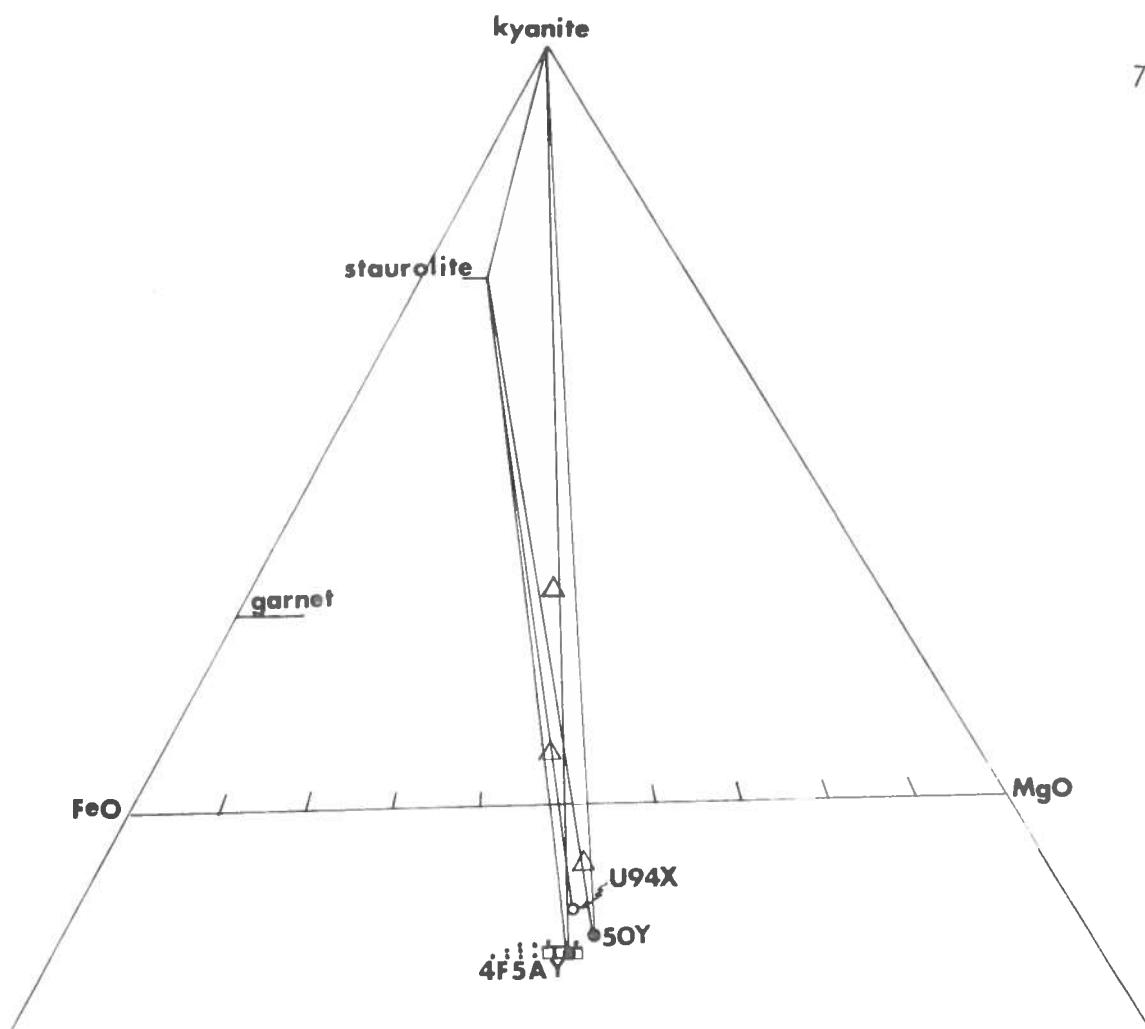


Figure 28. Thompson projection for kyanite-zone specimens. Large circles are chemically analyzed biotites; closed circles from assemblage 2, and open circle from assemblage 1. Squares and dots are X-ray determined biotites; squares from assemblage 2, dots from assemblage 1. All X-ray samples have undetermined Al contents, separation of symbols is for clarity only. Triangles are effective bulk compositions determined using modes (Table 2).

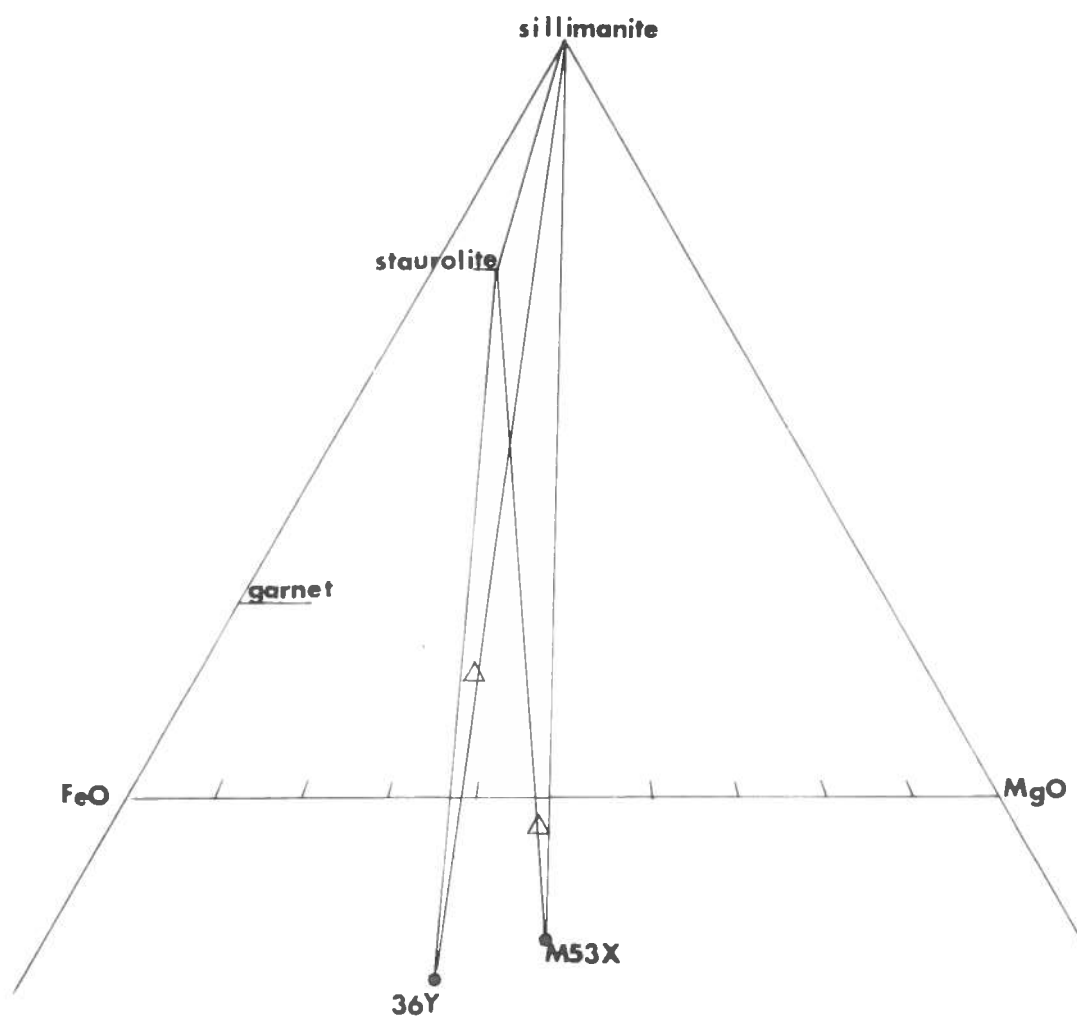


Figure 29. Thompson projection for specimens from lower grade portion of sillimanite zone showing biotite compositions (circles) and effective bulk compositions (triangles). The effective bulk compositions were determined using modes (Table 2).

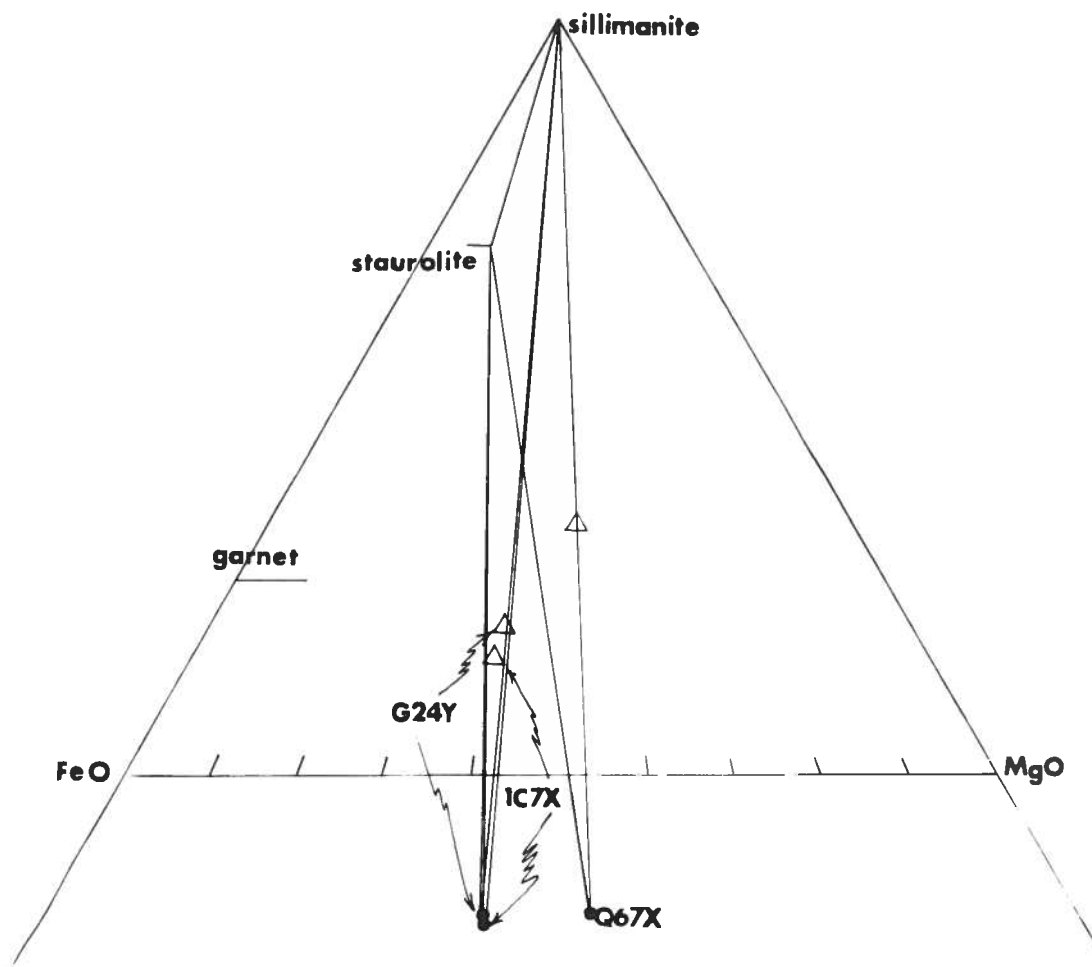


Figure 30. Thompson projection for specimens from the higher grade portion of the sillimanite zone showing biotite compositions (circles) and effective bulk compositions (triangles). The effective bulk compositions were determined using modes (Table 2).

even though there is overlap in the compositions of biotites from the lower and higher grade portions of the sillimanite zone. The only exception is Q67X, which is lower in Fe than even the kyanite-zone specimens. This might be explained if Q67X is not really in assemblage 2 but is in assemblage 3. There is only a trace of staurolite in thin section and some question may be raised as to its equilibrium with biotite.

The biotites indicate that a reaction has taken place: Mg-rich biotite + staurolite + muscovite + quartz = Fe-rich biotite +  $\text{Al}_2\text{SiO}_5$  +  $\text{H}_2\text{O}$ . If this is the case, the modes should indicate an increase of sillimanite and a decrease in staurolite and muscovite as the reaction proceeds, assuming a constant bulk composition. However, inspection of Table 2 shows that this is not so. Even within the same formation the pattern is not consistent with constant effective bulk composition.

The effective bulk compositions within the three-phase triangles can be approximated by using the point-counted modes and molar volumes listed in Table 12. Dividing the modal percentages of staurolite, kyanite or sillimanite, and biotite by the molar volumes (for biotite the molar volumes have been corrected for Fe/Mg ratio) and recalculating to 100 gives approximate molar percentages of the phases. These have been plotted in Figures 28-30. Even with errors in the modal analysis and volume assumptions, the effective bulk compositions vary considerably both with respect to Fe/Mg and Al. This is true even within a given

formation.

Original systematic changes in bulk composition is a possible but unlikely explanation because the Partridge and Littleton Formations would be required to show parallel changes in lithology (Robinson, 1963). It is more likely that other reactions changing the effective bulk composition occurred with the reaction changing the biotite Fe/Mg ratio. Without analyses of all the phases, particularly the staurolites, the nature of these other reactions is elusive.

Another reaction which may be invoked to account for the appearance of  $\text{Al}_2\text{SiO}_5$  in the Littleton formation in the sillimanite zone, and which may also partly account for the shifting effective bulk composition is the following: Na-rich muscovite = K-rich muscovite + sillimanite + Ab-component in feldspar. This would be very effective in changing the amount of Al in the effective bulk composition, but could not account for a change in effective Fe/Mg. Another possible reaction is the following: staurolite + muscovite = almandine-component in garnet + sillimanite + biotite. This reaction would tend to decrease Fe/Mg and would also affect the effective Al content in a complicated manner.

The wide variation in Na content of muscovites (Fig. 21) suggests that the first reaction may be important. However, the plagioclase modal amounts are very low. It would be difficult to explain, for example in G24Y, 3.1 percent sillimanite produced with only 0.2 percent plagioclase. The actual zoning observed in some garnets is consistent with the second reaction, but this zoning occurs even where there is no Al-silicate.



Consideration of the garnets requires the addition of other components to the Thompson Projection. Using MnO as a fourth coordinate, projection from the  $\text{Al}_2\text{SiO}_5$  corner to the MgO-FeO-MnO plane gives a diagram on which phase compositions can be plotted. All assemblages in this projection have as essential phases quartz, muscovite, and kyanite or sillimanite. Figure 31 is such a projection with the compositions of the coexisting biotites and garnet edges plotted (note that the MnO scale is much distorted to show the tie lines more clearly). The garnet edge compositions are plotted under the assumption that the edges are all that is in equilibrium with the biotite. For the garnets, because data on Mg/Ca is not available for all the garnets, the third coordinate is Mg and Ca.

The tie lines cross very near to one another (50A is an exception) even though 908A is not even in assemblage 2. If the trend is real, it suggests that there is an approximately equal effective bulk composition (with respect to Mn) even among different formations and assemblages. It also indicates garnet-biotite pairs equilibrated by the reaction: Fe-poor garnet + Fe-rich biotite = Fe-rich garnet + Fe-poor biotite. These results are based, however, on only semiquantitative results and exact microprobe analyses of the pairs would be necessary to confirm them.

#### Composition of biotites and metamorphic grade

The biotites vary principally in Fe/Mg. Robinson (1963) suggested that this variation was due to the following reaction:

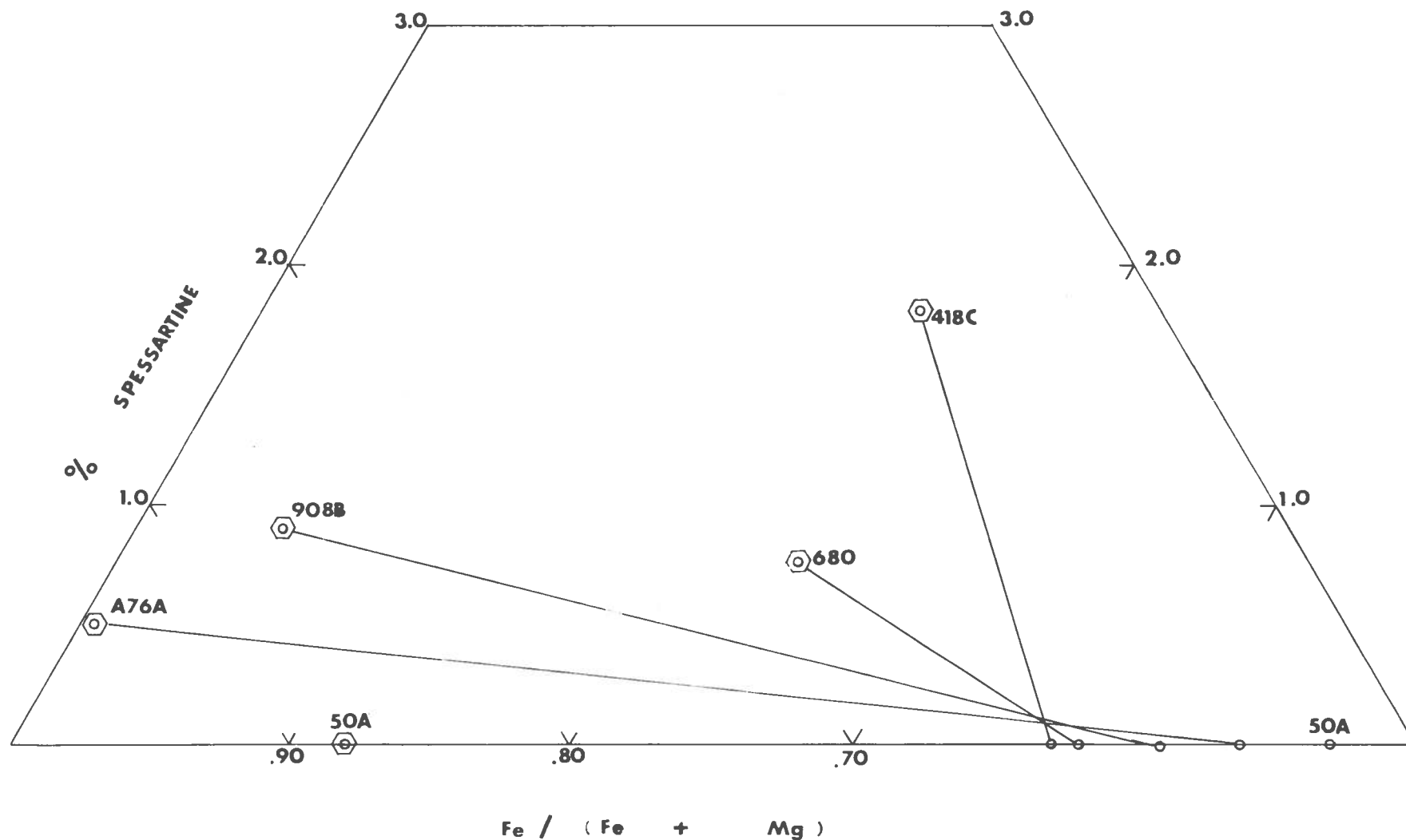


Figure 31. Distorted and enlarged MnO-FeO-MgO diagram showing compositions of biotites (circles) and coexisting garnet edge compositions (hexagons). For the garnet edges, Ca is treated as Mg because Ca/Mg ratios are unknown. Note distorted, greatly enlarged MnO scale.

Mg-rich biotite + staurolite + muscovite + quartz = Fe-rich biotite + kyanite or sillimanite +  $H_2O$ .

This is a sweeping reaction and can proceed in two ways. Either the staurolite changes in composition with the biotite or the staurolite remains fixed in composition and the change in biotite is reflected solely in the relative amounts of the phases. If the first case pertains, there is no hope of quantitative phase analysis without chemical analyses of the staurolites, because a balanced reaction could not be written. If the second case pertains, assumption of a reasonable but fixed staurolite composition allows an estimate of the controls of metamorphism. In order to make such an estimate at all quantitative it is necessary to have accurate data on the volume of water at high temperatures and pressures, and on the  $\Delta S$  of dehydration reactions and  $\Delta S$  for changes in coordination of aluminum (Thompson, 1955, p. 83; Albee, 1965, p. 516).

The temperatures and pressures under consideration must have been greater than 622°C and 5.5 kilobars, the triple point for the aluminosilicates (Gilbert, Bell, and Richardson, 1968, p. 135). No direct data on the  $\Delta S$  of hydration and the volume of water at these high pressures is available, but a reasonable approximation is possible. Fyfe, Turner, and Verhoogen (1958, p. 118) approximated the  $\Delta S$  of dehydration reactions for pressures up to 2.5 kilobars and temperatures up to 800°C based on the difference in entropy between ice and water. Even at these relatively low pressures, however, the data are probably

good only to within a few entropy units. The data on molar volumes of water by Kennedy and Holser (1966, p. 377-379) can be interpolated to give reasonable values for the conditions considered.

The slope of the univariant line representing the reaction must satisfy the following equation in the case where  $P_{H_2O} \cong P_{total}$  (Albee, 1965, p. 517):

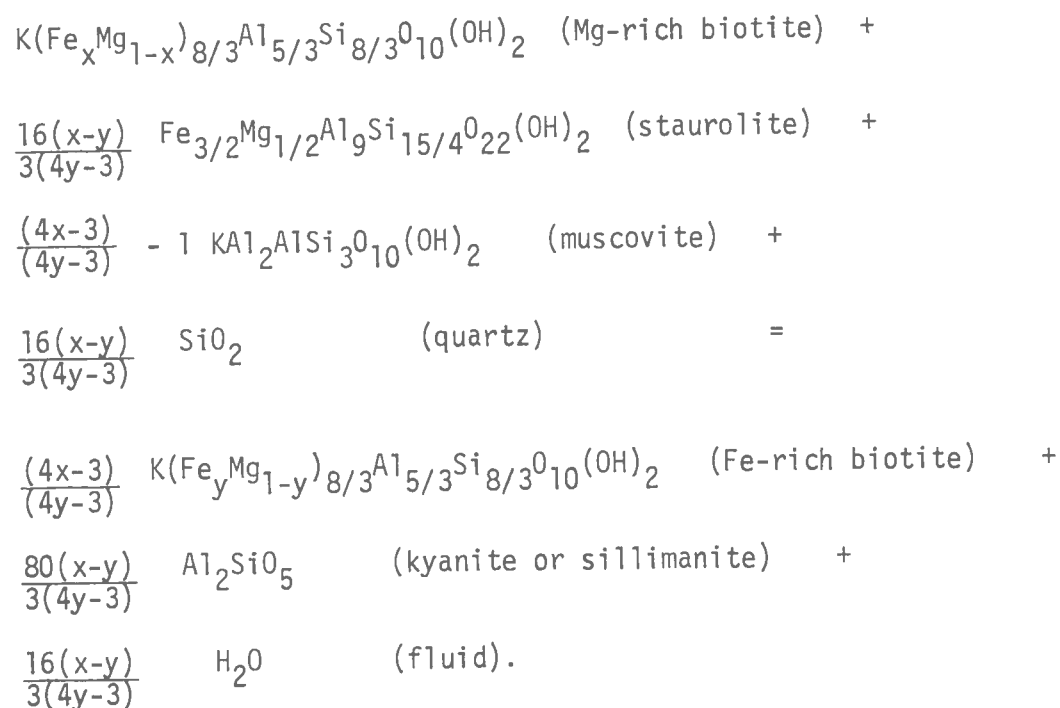
$$\frac{dP_s}{dT} = \frac{\Delta S/nH_2O}{\Delta V_s/nH_2O + V_{H_2O}} ,$$

where  $dP_s/dT$  is the slope,  $\Delta S$  is the change in entropy,  $\Delta V_s$  is the change in volume of the solids,  $V_{H_2O}$  is the molar volume of water at the pressure and temperature in question, and  $nH_2O$  is the number of moles of water produced in the reaction.

Extrapolation of the data in Fyfe, Turner, and Verhoogen and Kennedy and Holser gives reasonable but very approximate values for the  $\Delta S$  of dehydration and  $V_{H_2O}$  at 5.5 kilobars and 650°C in the general range at which the reactions must have occurred. Much higher temperatures at the moderate activities of water suggested by the hydrous phases present (Robinson, 1963) would lead to partial melting in rocks of appropriate composition.

The approximations used here are  $V_{H_2O} = 26.6$  cc/mole,  $\Delta S$  of dehydration = 606 decijoules/degree/mole. These values are appropriate to temperatures and pressures in the general range considered. The staurolite formula assumed is essentially that of Smith (1968, p. 1139), with

Fe/Mg = 3 as the mean value from the range of observed staurolite analyses reported by Hounslow and Moore (1967). The formula is  $Al_{18}Fe_3MgSi_{15/2}O_{44}(OH)_4$ . The equation can be balanced as follows:



The coefficients are, of course, determined by the stoichiometry.

The volumes of the phases used for the calculations are presented in Table 12. The volume of biotite is further corrected for Fe/Mg ratio by using the analytic function  $4.66 (Fe/Fe + Mg) + 149.66$ . This assumes linearity between the end-member volumes and ignores volume of mixing, but these are likely to be small in solid phases. In the reaction producing kyanite, the volume of the solid products is:

Table 12. Assumed molar volumes.

Kyanite	$\text{VI}$ $\text{Al}_2\text{SiO}_5$	<u>Volume, cc/mole</u> 44.11
Sillimanite	$\text{VI IV}$ $\text{Al Al SiO}_5$	49.91
Staurolite	$\text{IV}$ $(\text{Fe,Mg})_2\text{Al}_9\text{Si}_{15/4}\text{O}_{22}(\text{OH})_2$	223
Quartz	$\text{SiO}_2$	22.69
Muscovite	$\text{VI IV}$ $\text{KAl}_2\text{AlSi}_3\text{O}_{10}(\text{OH})_2$	140.55
Annite	$\text{IV}$ $\text{KFe}_3\text{AlSi}_3\text{O}_{10}(\text{OH})_2$	154.32
Phlogopite	$\text{IV}$ $\text{KMg}_3\text{AlSi}_3\text{O}_{10}(\text{OH})_2$	149.66
Biotite	$\text{IV}$ $\text{K}(\text{Fe,Mg})_3\text{AlSi}_3\text{O}_{10}(\text{OH})_2$	$4.66(\text{Fe}/\text{Fe}+\text{Mg}) + 149.66^*$

\*This equation is applicable to a biotite of any Fe/Mg ratio, assuming a linear extrapolation between annite and phlogopite. Volume of mixing effects are ignored, but are likely to be small.

Source: Robie, et. al. (1966, p. 69, 70).

$$\frac{(4x-3)}{(4y-3)} \text{ moles} \times (4.66y + 149.66) \text{ cc/mole Fe-rich biotite} +$$

$$\frac{80(x-y)}{3(4y-3)} \text{ moles} \times 44.11 \text{ cc/mole kyanite.}$$

The volume of the solid reactants is:

$$1 \text{ mole} \times (4.66x + 149.66) \text{ cc/mole Mg-rich biotite} +$$

$$\frac{16(x-y)}{3(4y-3)} \text{ moles} \times 223 \text{ cc/mole staurolite} +$$

$$\frac{(4x-3)}{(4y-3)} 1 \text{ moles} \times 140.55 \text{ cc/mole muscovite} +$$

$$\frac{16(x-y)}{3(4y-3)} \text{ moles} \times 22.69 \text{ cc/mole quartz.}$$

Subtracting and simplifying gives:

$$\Delta V_s = -83.61 (x-y)/(4y-3)$$

Division by  $16(x-y)/3(4y-3)$ , the  $n_{H_2O}$ , gives  $\Delta V_s = -15.68 \text{ cc}$ . Notice that although the  $\Delta V_s$  is dependent on product and reactant biotite compositions, when the  $\Delta V_s$  is normalized to one mole of  $H_2O$ , the term in  $x$  and  $y$  drops out. This is because the stoichiometry of the reaction requires that the number of moles of  $H_2O$  produced be dependent on the initial and final biotite composition. The normalized  $\Delta V_s$  is then completely independent of initial and final biotite compositions. The amount of the change in biotite composition per one mole of water depends on the initial composition of the biotite, as indicated in Figure 32.

The part of  $\Delta S$  attributable to changes in the coordination of Al from VI to IV must be approximated from a consideration of reactions in which

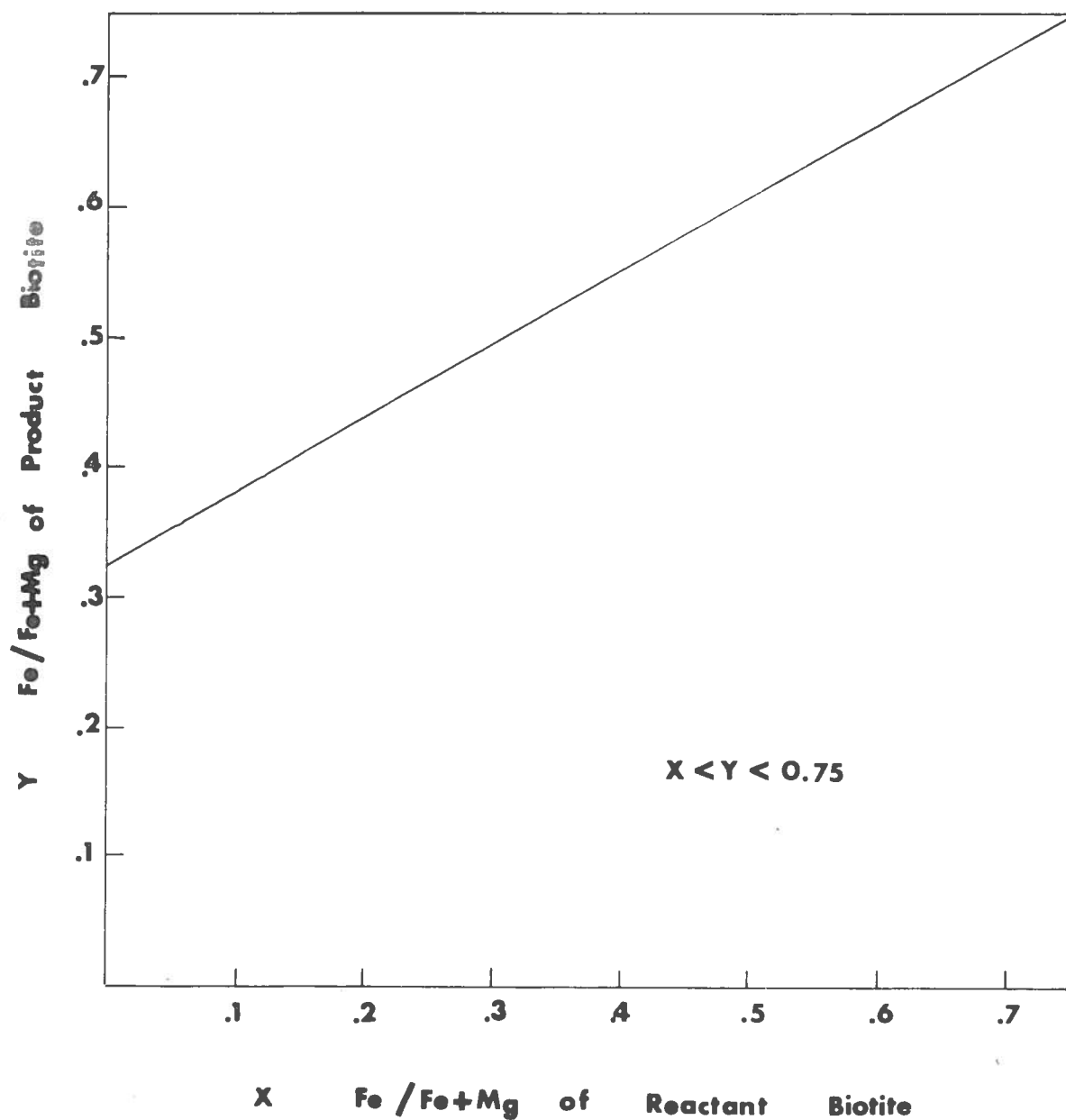


Figure 32. Fe/Fe + Mg of product biotite as a function of Fe/Fe + Mg of reactant biotite per mole of  $H_2O$  produced in reaction  $Mg\text{-rich biotite} + \text{staurolite} + \text{muscovite} + \text{quartz} = \text{Fe-rich biotite} + Al_2SiO_5 + H_2O$ . Intersection of compositions at 0.75 is fixed by assumed Fe/Mg of staurolite. Y-intercept is 0.321.



the  $\Delta S$  is attributable to changes in the coordination of Al. This is the approach used by Albee (1965a) but there are errors in his calculations. For 19 reactions,  $\Delta S^\circ$  was computed, using the data in Robie and Waldbaum (1968). These computed  $\Delta S$  values are listed in Table 13. It will be noted that there is a large range in  $\Delta S$  values, even where the major contribution is due to change in coordination of Al. For example, in reaction 5 (Table 13), kyanite = sillimanite,  $\Delta S = 123$  dj/deg mole Al VI  $\rightarrow$  IV, and for reaction 19, jadeite + quartz = albite,  $\Delta S = 352$  dj/deg. mole Al VI  $\rightarrow$  IV. This suggests that it is important to consider the type of crystallographic site in which Al is situated as well as the coordination (Table 14).

For the reaction under consideration in this work, the total octahedral Al going to tetrahedral Al is:

$$\frac{1}{3} - \frac{1(4x-3)}{3(4y-3)} \quad \text{for the kyanite-producing reaction, and:}$$

$$\frac{1}{3} - \frac{1(4x-3)}{3(4y-3)} - \frac{80(x-y)}{3(4y-3)} \quad \text{for the sillimanite-producing reaction.}$$

For the kyanite-producing reaction, the algebraic expression above is always less than one, and the tetrahedral Al is greater in the product. This excess tetrahedral Al can be shown to be always 0.25 for any x and y per mole of H<sub>2</sub>O produced. This means that some octahedral Al is being converted to tetrahedral Al in Fe-rich biotite. This change in Al site is most closely approximated by the change in reactions 7, 8, and 15, in which octahedral Al goes to a mica-like tetrahedral site (Table 14).

Table 13.  $\Delta S^\circ$  Values of reactions involving change in coordination of Al.

	$\Delta S^\circ$ per Al <sup>VI→IV*</sup>
(1) $K_2O + 3 \text{ corundum} + 2 \text{ ice} + 6 \text{ quartz} = 2 \text{ muscovite}$	-35
(2) $K_2O + \text{corundum} + 2 \text{ ice} + 6 \text{ periclase} + 6 \text{ quartz} = 2 \text{ phlogopite}$	-24
(3) $\text{muscovite} + 3 \text{ clinoenstatite} = \text{phlogopite} + \text{sillimanite} + 2 \text{ quartz}$	62
(4) $K_2O + \text{kaolinite} + 2 \text{ corundum} + 4 \text{ quartz} = 2 \text{ muscovite}$	64
(5) $\text{kyanite} = \text{sillimanite}$	123
(6) $K_2O + \text{diaspore} + \text{gibbsite} + 2 \text{ corundum} + 6 \text{ quartz} = 2 \text{ muscovite}$	140
(7) $K_2O + \text{kaolinite} + 2 \text{ kyanite} + 2 \text{ quartz} = 2 \text{ muscovite}$	150
(8) $K_2O + \text{diaspore} + \text{gibbsite} + 6 \text{ periclase} + 6 \text{ quartz} = 2 \text{ phlogopite}$	151
(9) $2 \text{ kyanite} + 2 \text{ enstatite} + \text{quartz} = \text{cordierite}$	157
(10) $3 \text{ kyanite} + 2 \text{ enstatite} = \text{cordierite} + \text{corundum}$	178
(11) $\text{diopside} + \text{corundum} = \text{Ca-Al pyroxene} + \text{periclase} + \text{quartz}$	190
(12) $2 \text{ sillimanite} + 2 \text{ enstatite} + \text{quartz} = \text{cordierite}$	190
(13) $K_2O + \text{corundum} + 6 \text{ quartz} = \text{microcline}$	230
(14) $\text{muscovite} + K_2O + 3 \text{ periclase} + 6 \text{ quartz} = \text{phlogopite} + 2 \text{ microcline}$	235
(15) $K_2O + 2 \text{ talc} + \text{corundum} = 2 \text{ phlogopite} + 2 \text{ quartz}$	276
(16) $\text{muscovite} + \text{quartz} = \text{sillimanite} + \text{microcline} + \text{ice}$	303
(17) $2 \text{ jadeite} = \text{albite} + \text{nepheline}$	337
(18) $3 \text{ sillimanite} + 2 \text{ enstatite} = \text{cordierite} + \text{corundum}$	337
(19) $\text{Jadeite} + \text{quartz} = \text{albite}$	352

\*All values are in decijoules/degree mole Al. Data are from Robie and Waldbaum (1968), and are applicable strictly only to 298.15°K and 1 atmosphere. The values are calculated as the  $\Delta S^\circ$  of the reaction as written divided by the number of moles of aluminum changing from octahedral to tetrahedral coordination.

Table 14. Types of Al transition in reactions 1 through 19 (Table 13).

<u>OCTAHEDRAL</u>	<u>TETRAHEDRAL</u>	<u><math>\Delta S^\circ</math></u>
(1) corundum	muscovite	-35
(2) corundum	phlogopite	-24
(3) muscovite	sillimanite	62
(4) kaolinite and corundum	muscovite	64
(5) kyanite	sillimanite	123
(6) diaspore, gibbsite, and corundum	muscovite	140
(7) kaolinite and kyanite	muscovite	150
(8) diaspore and gibbsite	phlogopite	151
(9) kyanite	cordierite	157
(10) kyanite	cordierite	178
(11) corundum	pyroxene	190
(12) sillimanite	cordierite	190
(13) corundum	feldspar	230
(14) muscovite	feldspar	235
(15) corundum	phlogopite	276
(16) muscovite	sillimanite or feldspar	303
(17) pyroxene	feldspar and nepheline	337
(18) sillimanite	cordierite	337
(19) pyroxene	feldspar	352

A reasonable approximation for this transition is 200 decijoules per degree-mole Al VI  $\rightarrow$  IV.

For the sillimanite-producing reaction, the algebraic expression is also always less than one, and the excess product tetrahedral Al can be shown to be always 5.25 for any x and y per mole of H<sub>2</sub>O produced. The 0.25 part of this Al is like that in the kyanite-producing reaction; the  $\Delta S$  is reasonably approximated by 200 dj/deg-mole Al. For the rest of the product Al, 5.00 moles, the transition is closest to reaction 5, kyanite = sillimanite, and thus 125 dj/deg-mole Al is a better value.

For the kyanite-producing reaction, the total entropy change due to Al changing from octahedral to tetrahedral sites, when normalized to one mole of product H<sub>2</sub>O, is  $0.25 \times 200 = 50$  dj/deg. For the sillimanite-producing reaction the  $\Delta S$  is  $(0.25 \times 200) + (5.0 \times 125) = 50 + 725 = 775$  dj/deg.

Using the  $\Delta S$  values,  $\Delta S$  of dehydration as above,  $\Delta V_s$  as above, and  $V_{H_2O}$  of 22.6 cc/mole, the slopes can be calculated from the Albee equation:

Kyanite-producing reaction

$$\frac{dP_s}{dT} = \frac{50 + 606}{-15.68 + 22.6} = \frac{656}{6.92} = 94.8 \text{ bars/degree.}$$

Sillimanite-producing reaction

$$\frac{dP_s}{dT} = \frac{775 + 606}{13.31 + 22.6} = \frac{1381}{35.91} = 38.5 \text{ bars/degree.}$$

The result of this analysis is to be expected from the original

assumption that staurolite remains fixed in composition. It is also strictly only applicable to a constant pressure and temperature for the assumed  $V_{H_2O}$  and  $\Delta S$  of hydration. The reaction lines will curve somewhat as  $V_{H_2O}$  and  $\Delta S$  change with pressure and temperature. The curvature will be small, however, as both  $V_{H_2O}$  and  $\Delta S$  show small increments for large changes in pressure and temperature at the high pressures along the kyanite-sillimanite isograd.

It is of interest to note that the slope for the reaction producing kyanite is much steeper than the slope for the reaction producing sillimanite. This leads to the situation illustrated in Figure 33. The lines of constant biotite composition are closer together in the sillimanite zone. This indicates that for the same rise in temperature, at constant pressure, the reaction in the sillimanite zone will produce a more Fe-rich biotite and more sillimanite will be produced. This is a plausible partial explanation for the abundant coarse-grained sillimanite in the Littleton Formation in the sillimanite zone and the lack of kyanite in the Littleton Formation in the kyanite zone. On Plate 1, all the biotites in assemblage 2 with percent octahedral Fe of 48 or greater occur in the sillimanite zone. The lowest percent Fe, in Q67X, may be explained if it is assumed that the rock is not really in assemblage 2, but is in assemblage 3 as discussed above. All the biotites in assemblage 2 in the kyanite zone have percent octahedral Fe of 45 or less. However, this is only a partial explanation, and some of the sillimanite may also be due to other reactions occurring simultaneously.

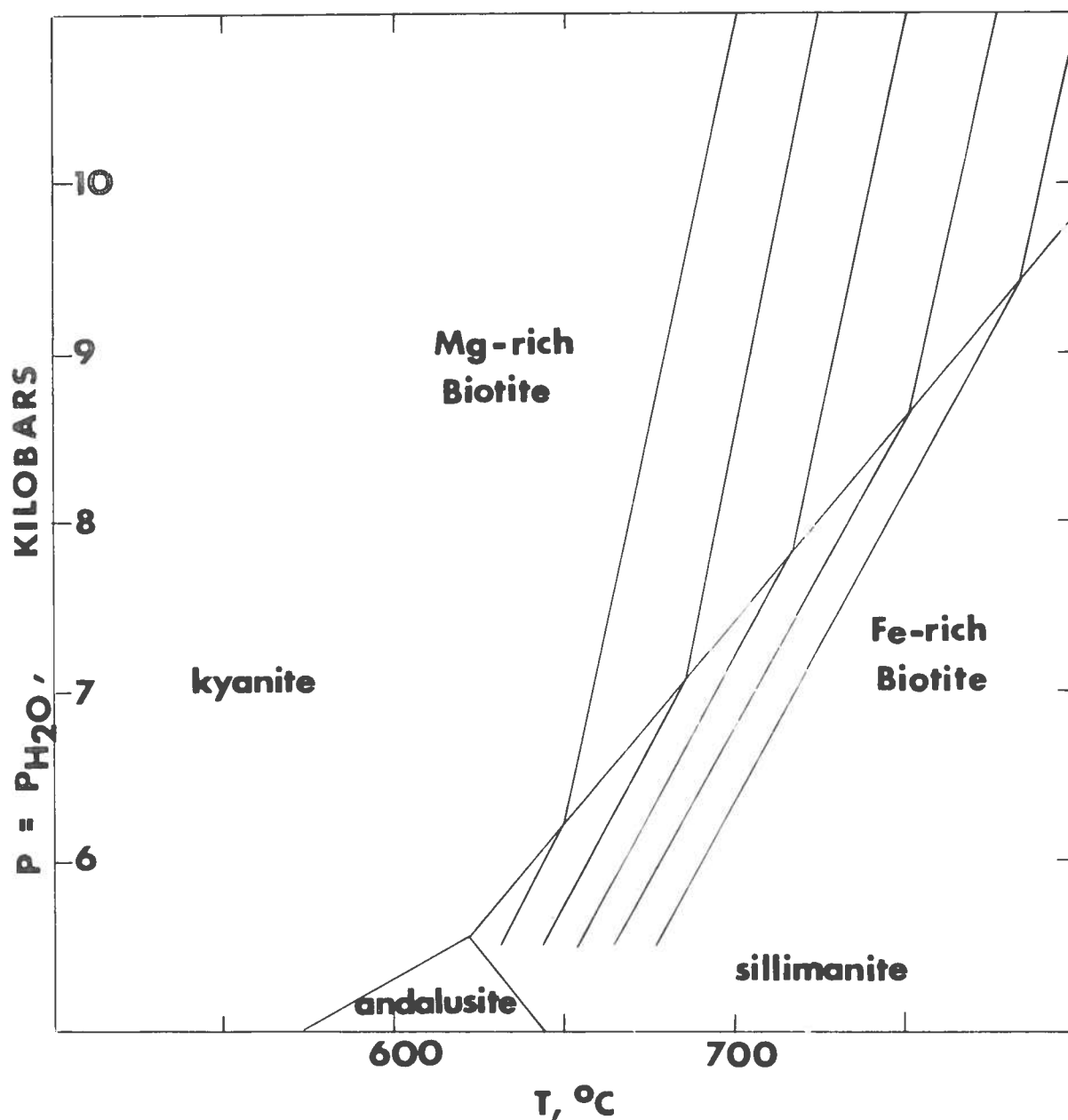


Figure 33.  $P_{\text{H}_2\text{O}}$ ,  $T$  diagram of  $\text{Al}_2\text{SiO}_5$  and biotite reaction lines.

Slopes shown are strictly only for 5.5 kb and 650 $^{\circ}\text{C}$ , but curvature is expected to be slight. Note large change of slope where biotite equilibria intersect kyanite-sillimanite transition. Slope of reaction lines in sillimanite zone is 38.5 bars/degree; in the kyanite zone the slope is 94.8 bars/degree.

Effect of pressure, temperature and activity of  $H_2O$ . The effects of pressure, temperature, and pressure of  $H_2O$  on dehydration reactions in general were discussed by Thompson (1955). For the particular reaction considered here, the effects of these variables are shown diagrammatically in Figure 34. The upper surface shown is the plane in which  $P = P_{H_2O}$  (the maximum value of  $P_{H_2O}$ ), where the activity of  $H_2O$  is 1.00. On this surface, increasing the pressure at constant temperature favors Mg-rich biotite; increasing the temperature at constant pressure favors Fe-rich biotite. If however,  $P_{H_2O}$  is not constrained to be equal to  $P_{total}$ , but instead is allowed to decrease below  $P_{total}$ , the  $a_{H_2O}$  will also decrease, and the effect of pressure on the reaction will depend on the  $a_{H_2O}$ . At high  $a_{H_2O}$  (path A), increasing pressure at constant temperature will favor Mg-rich biotite. At low  $a_{H_2O}$  (path B), increasing pressure favors Fe-rich biotite. Probably of greater importance is the effect of increasing  $a_{H_2O}$  at constant temperature and pressure (path C). Increasing  $a_{H_2O}$  at constant pressure and temperature favors Mg-rich biotite.

$fO_2$  by ferric/ferrous ratio. The ferric/ferrous ratio of biotites internally defines the  $fO_2$ , in the terminology of Eugster and Wones (1962). The ratio of  $Fe^{3+}/Fe^{3+} + Fe^{2+}$  of the analyzed biotites has a mean of 0.096 with a range from .064 to .130. If the ferric content is really indicative of the composition of the biotites during metamorphism, and is not, in part, a result of weathering, then the ferric/

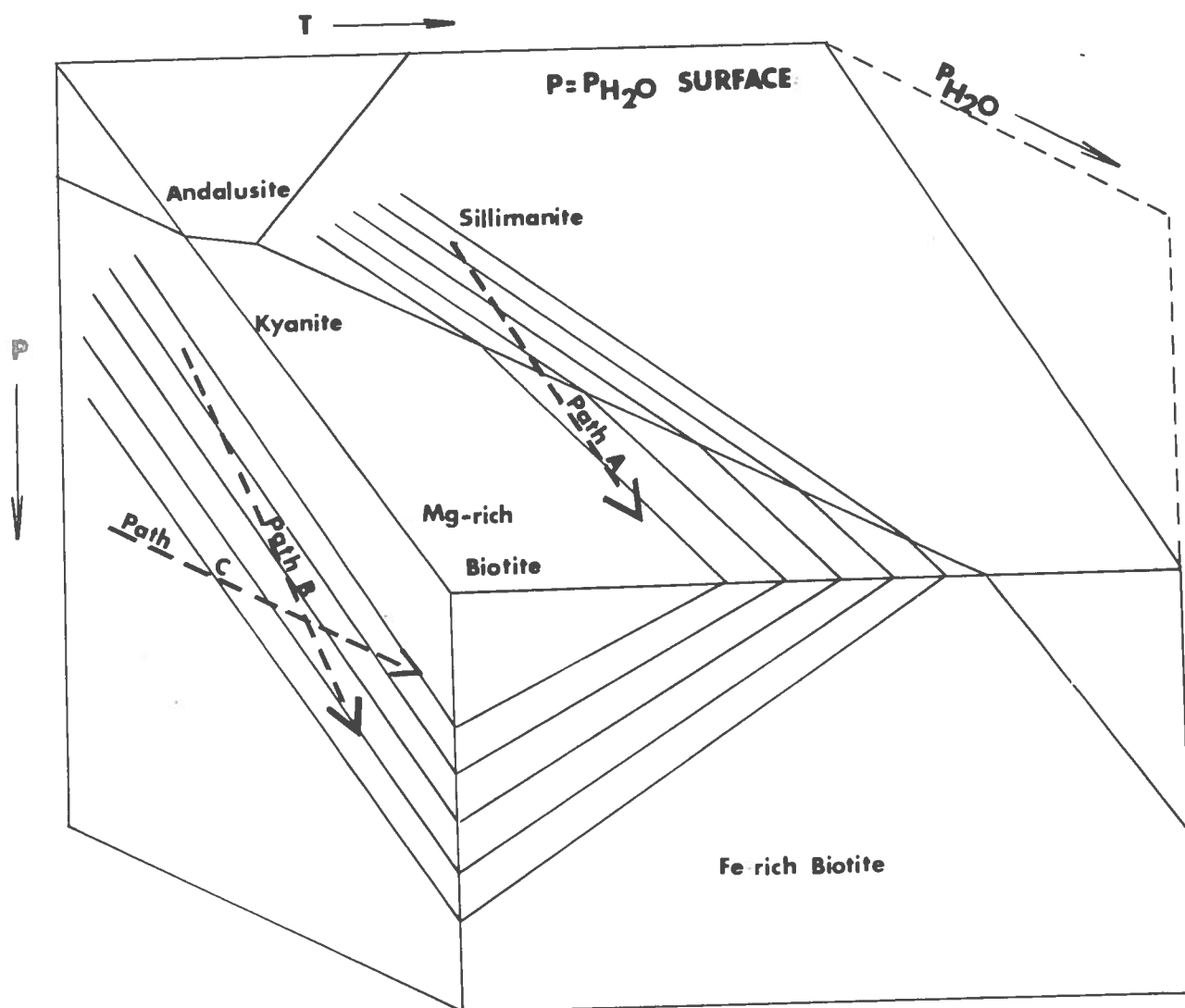


Figure 34.  $P$ - $T$ - $P_{H_2O}$  diagram modified from Thompson (1955). Surface shown is  $P = P_{H_2O}$  which corresponds to Fig. 35. Path A is high  $a_{H_2O}$  path; path B is low  $a_{H_2O}$  path. On the  $P = P_{H_2O}$  surface,  $a_{H_2O}$  is 1.00. Path C shows effect of increasing  $a_{H_2O}$  at constant  $P$  and  $T$ .



ferrous ratio would indicate oxygen fugacities approximating those of the Ni-NiO buffer. The oxygen fugacity of the Ni-NiO buffer is determined by the analytical expression (Wones and Eugster, 1965, p. 1230):

$$\text{Log } f_{\text{O}_2} = \frac{-24,709}{T} + 8.94 + \frac{0.046(P-1)}{T}$$

Work by French (1966, p. 237), however, indicates that graphite is not stable with the Ni-NiO buffer assemblage above about 450°C at 5.5 kbars  $P_{\text{fluid}}$ . Estimates of the temperature and pressure of metamorphism of the Orange area (Robinson, 1963) indicate that this temperature is much too low. If, on the other hand, the buffer assemblage which represents the oxygen fugacities in quartz-fayalite-magnetite (QFM), a maximum temperature of about 625°C at 5.5 kbars  $P_{\text{fluid}}$  is compatible with the presence of graphite. Thus, oxygen fugacities equal to or lower than those of the QFM buffer seem more reasonable.

The analytical expression for the QFM buffer assemblage is:

$$\text{Log } f_{\text{O}_2} = \frac{-27,300}{T} + 10.30 + \frac{0.092(P-1)}{T} \quad (\text{Wones and Eugster, 1965, p. 1230}).$$

In view of the presence of graphite or carbonaceous material in nearly all the specimens and the equilibrium conditions described above, it seems very probable that the ferric content of the analyzed biotites, in particular 36Y, is due to slight weathering.

#### Origin of garnet zoning

The zoning in the garnets can be analyzed by plotting the compo-

sitions of the edges and centers of the garnets as in Figure 35 and drawing growth vectors from the centers to the edge points. In effect this diagram is a distorted triangle with the coordinates almandine, spessartine, and pyrope-grossular. It is assumed that the major portion of the garnets falls within these compositional limits (as the microprobe analyses indicate).

The compositions plotted are those from the milliprobe analyses. The pyrope-grossular component is found by difference, so the accuracy of the values is questionable. The trends, however, seem fairly clear. It is probable that Mg is more important than Ca in the pyrope-grossular component on the basis of the microprobe results (Table 11) and analyses of garnets from similar metamorphic assemblages (Miyashiro, 1953; Sturt, 1962; Albee, 1965; Harte and Henley, 1966). This is especially true since the coexisting biotites contain large amounts of Mg, and no Ca-rich phase appears abundantly in these rocks.

The types of zoning observed from center to edge in the nine garnet specimens fall into three fairly distinct classes: (1) those garnets which get richer in Fe, poorer in Mn, and much poorer in Mg and Ca; (2) those garnets which get richer in Fe, poorer in Mg and Ca, and much poorer in Mn; and (3) those garnets which get richer in Mg and Ca and poorer in Fe and Mn.

In the first class are garnets 50A, 50AB, and A76A. These garnets get only slightly lower in Mn, but considerably higher in Fe toward the edges. The microprobe results for 50AB show Fe only slightly increasing. However, they do indicate only a slight decrease in Mn.

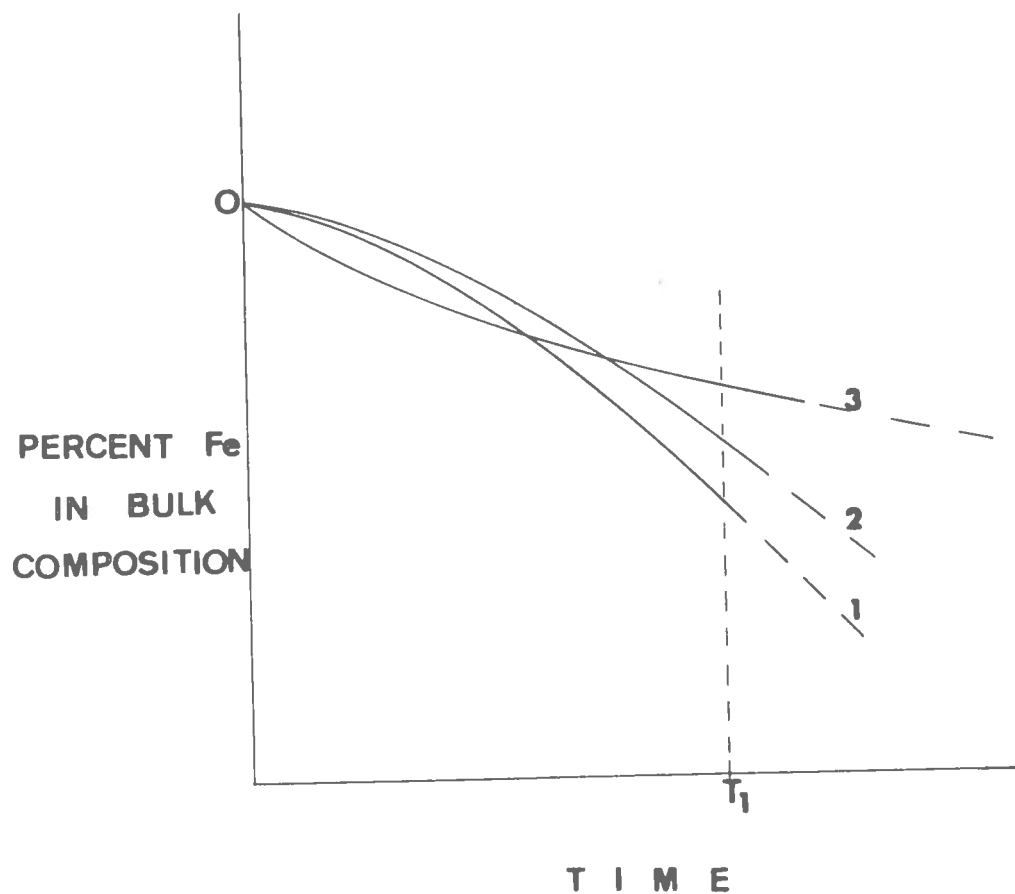


Figure 35. Possible changes in percent Fe in bulk composition due to zoning of three kinds: (1) strong Fe-zoning, (2) moderate Fe-zoning and (3) reverse Fe-zoning. 0 is original bulk composition. Time  $T_1$  is arbitrary time at which percent Fe in bulk composition increases in order 1, 2, 3.

The Mg-Ca component must therefore show a decrease with garnet growth. Ca depletion was suggested as a major factor in garnet zoning by Hollister (1966, p. 1650) and was also found by Harte and Henley (1966). In garnets 50AB and A76A, Ca zoning may be important due to the original very low Mn content.

Type 2 zoning is shown by garnets 908A, 908B, and 908C. This type of zoning is characterized by strong Mn depletion. The milliprobe results also indicate lowering in Mg and Ca, but this is not found in the microprobe results. Iron increases markedly.

Type 3 zoning is shown by garnets 680 and 418C. A reversal of the Fe trend is clear in both milliprobe and microprobe results. Mn zoning is also present, and is especially well-developed in 680.

The bell-shape of the Mn profiles in 908A, 908B, 908C, 50AB, and 680 is similar to that found by Hollister (1966) and Harte and Henley (1966). These authors considered the Mn depletion to be a fractionation process that depleted the area immediately surrounding the garnet in Mn. Hollister (1966) even derived a mathematical model of the process. Because of the good fit of his model-predicted and observed curves, Hollister believed the following to be true: (1) complete removal of garnet from a homogeneous reservoir during crystallization, and (2) a nearly constant fractionation factor between garnet and reservoir. The fractionation factor is the weight-fraction of Mn in the infinitesimally thin outer edge of the garnet divided by the weight-fraction of Mn in the rock exclusive of garnet. Zoning necessarily requires a large

fractionation factor for Mn between garnet and the other Mn-bearing phases. As Mn is subtracted from the system, both weight-fractions decrease, but the ratio remains constant. The causes for this large fractionation factor are presumably crystal chemical in nature and may involve crystal field effects. Since temperature changes apparently have a large effect on fractionation factors (Hollister, 1966), and the bell-shaped curves indicate a constant factor, it can be surmised that the garnets grew at constant temperature or during small temperature changes.

The petrologic consequence of garnet zoning is to subtract the garnet from the equilibrium system, thus changing the bulk composition of the system in a manner analogous to igneous zoning of plagioclases. As closely as the milliprobe can measure, however, the garnet compositions do not come to zero Mn at the edges. Close inspection of the profiles by Hollister (1966) or Harte and Henley (1966) shows that their garnets do not reach zero Mn either, so that the garnet edge is still in the system. This point is of importance in the analysis of phase equilibria.

The presence of zoning in the garnet allows speculation concerning the change in effective bulk composition. Strongly Fe-zoned garnets 50A, 50AB, and A76A have coexisting biotites with percent Fe of 43 and 45. Moderately Fe-zoned garnets 908A, 908B, and 908C have percent Fe of coexisting biotites of 47 (even though in assemblage 1). Reverse Fe-zoned garnets 680 and 418C have percent Fe of coexisting biotites

of 49 and 50. A possible explanation for this is indicated in Figure 36. The biotite composition is a partial reflection of the bulk composition on the Thompson Projection (Figs. 28-30). If the zoning is type 1 (strong Fe-zoning), the bulk composition should get less Fe-rich as the garnets grow, but at an ever-increasing rate (assuming a constant rate of growth). If the zoning is type 2 (moderate Fe-zoning) the bulk composition should get less Fe-rich at an ever-increasing rate as the garnets grow, but not so fast as in type 1. If the zoning is type 3 (reverse Fe-zoning), the bulk composition should get less Fe-rich at an ever-decreasing rate. The end result at time  $T_1$  (Fig. 36) should be garnets with zoning 1, 2, and 3 and bulk compositions (biotite compositions) increasing in the order shown. For this to happen, the Mg in the garnet must not be as zoned as the Fe, because the Fe/Mg ratio must decrease on the Thompson projection. It is of interest to note that Chinner (1965) found biotite compositions controlled by the same reaction in Glen Cova, Scotland, but that the modes were compatible with a constant bulk composition. That is, staurolite decreased and kyanite increased as the Fe/Mg ratio in biotites increased. Unlike the garnets in the Orange area, however, the garnets at Glen Cova were unzoned. Even though they were "...checked for inhomogeneity...on the X-ray microanalyzer...none showed any zoning for Fe or Mn." (Chinner, 1965, p. 133).

#### Conditions of metamorphism of the Orange area

The mineralogic data presented above allow a generalized evaluation of the conditions of metamorphism of the Orange area, at least to the

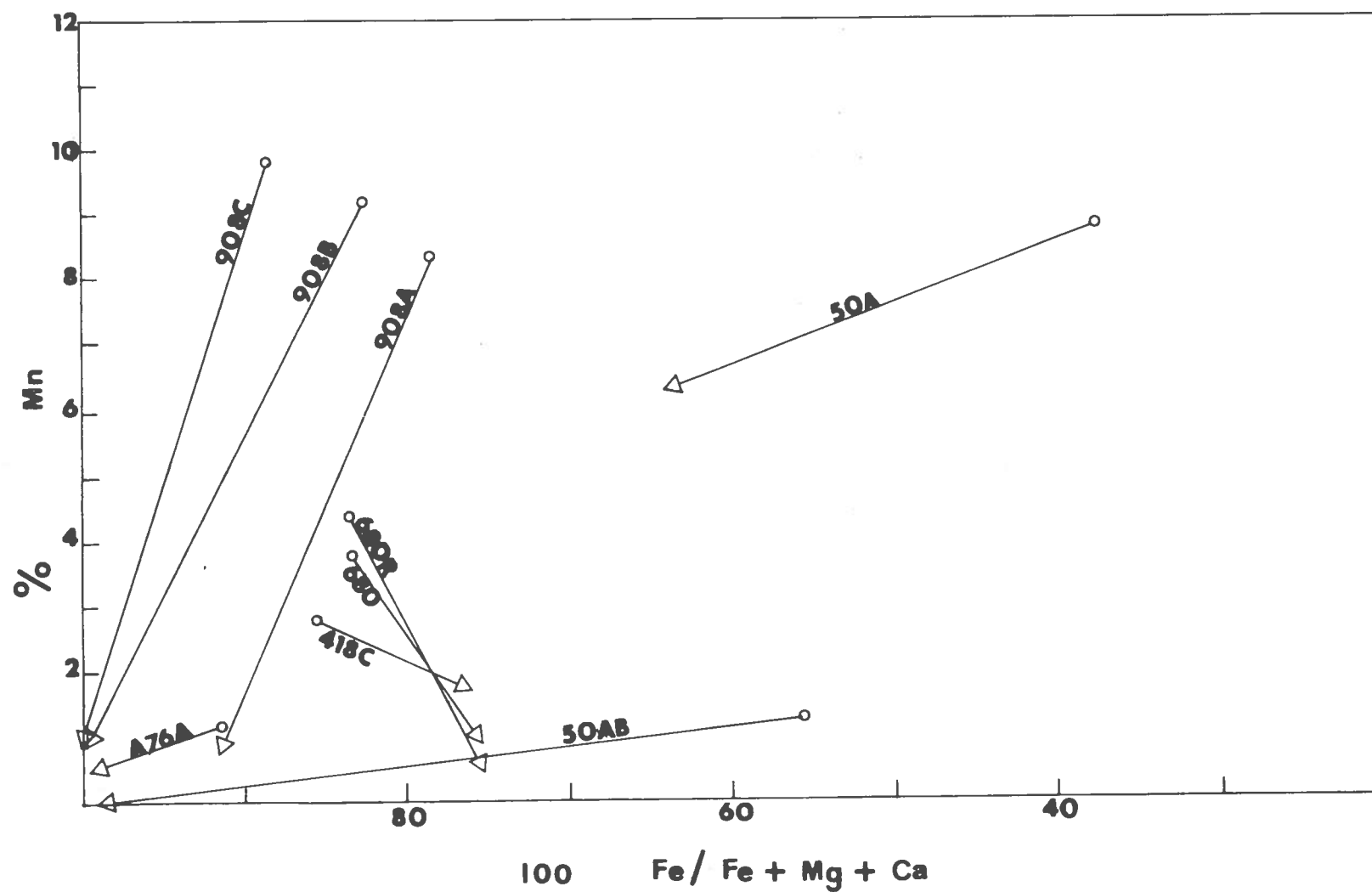


Figure 36. Change in garnet compositions from centers (circles) to edges (triangles). In effect diagram is a distorted triangle with corners Mn, Fe, and Ca + Mg.

extent of indicating probable directions of increase of the variables. Because the  $\text{Al}_2\text{SiO}_5$  polymorphs are kyanite and sillimanite, pressures and temperatures must have been greater than 5.5 kilobars and  $622^\circ\text{C}$ , the triple point for the alumino-silicates (Gilbert, Bell, and Richardson, 1969). The mapped variations in Fe/Mg ratio in biotites in the critical assemblage (Pl. 1) suggest that there were two ridges of generally higher temperatures or lower activities of  $\text{H}_2\text{O}$  extending northwestward from the generally higher grade region to the southeast. Conditions in these areas were appropriate for the production of a relatively Fe-rich biotite in the critical assemblage. The large deviations of the biotite compositional contours from the generalized trend of the kyanite-sillimanite boundary suggest that there were local variations in activity of  $\text{H}_2\text{O}$  less regular than the probable distribution of isotherms and isobars. Relations between biotite compositional contours and the geologic map suggest that these variations in activity of  $\text{H}_2\text{O}$  may have been controlled by local structural and lithologic features.



## REFERENCES CITED

- Albee, A.L., 1965a, A petrogenetic grid for the Fe-Mg silicates of pelitic schists: *Am. Jour. Sci.*, v. 263, p. 512-537.
- 1965b, Distribution of Fe, Mg, and Mn between garnet and biotite in natural mineral assemblages: *Jour. Geology*, v. 73, p. 155-164.
- 1965c, Phase equilibrium in three assemblages of kyanite-zone pelitic schists, Lincoln Mtn. quadrangle, central Vermont: *Jour. Petrology*, v. 6, p. 246-301.
- Azaroff, L.V., and Buerger, M.J., 1958, *The powder method*: New York, McGraw-Hill, 342 p.
- Bradley, W.F., and Grim, R.E., 1961, The mica clay minerals, in Brown, G.M., ed., *The X-ray identification and crystal structures of clay minerals*: London, Mineralogical Society, Clay Minerals Group, p. 208-241.
- Brindley, G.W., and Gillery, F.H., 1956, X-ray identification of chlorite species: *Am. Mineralogist*, v. 41, p. 169-186.
- Brown, G.M., 1955, The effect of isomorphous substitutions on the intensity of basal reflections of the mica-chlorite type structures: *Mineralog. Mag.*, v. 30, p. 657-665.
- Butler, B.C.M., 1967, Chemical study of minerals from the Moine Schists of the Ardnamurchan Area, Argyllshire, Scotland: *Jour. Petrology*, v. 8, p. 233-267.
- Chinner, G.A., 1965, The kyanite isograd in Glen Cova, Angus, Scotland: *Jour. Petrology*, v. 1, p. 178-217.
- Crowley, M.S., and Roy, Rustum, 1964, Crystalline solubility in the muscovite and phlogopite groups: *Am. Mineralogist*, v. 49, p. 348-362.
- Deer, W.A., Howie, R.A., and Zussman, J., 1966, *An introduction to the rock-forming minerals*: New York, John Wiley and Sons, 528 p.
- Engel, A.E.J., and Engel, C.F., 1960, Progressive metamorphism and granitization of the major paragneiss, northwest Adirondack Mtns., New York: Part II; *Mineralogy: Geol. Soc. America Bull.*, v. 71, p. 1-58.
- Eugster, H.P., and Wones, D.R., 1962, Stability relations of the ferruginous biotite, annite: *Jour. Petrology*, v. 3, p. 82-125.

- Evans, B.W., and Guidotti, C.V., 1966, The sillimanite-potash feldspar isograd in western Maine, U.S.A.: *Beitr. Mineralogie u. Petrographie*, v. 12, p. 25-62.
- Foster, M.D., 1960, Interpretation of the composition of trioctahedral micas: U.S. Geol. Survey Prof. Paper 354-B, p. 11-49.
- Wones, D.R., and Eugster, H.P., 1963, The atomic ratios of natural ferruginous biotites with reference to "The stability relations of the ferruginous biotite, annite" A discussion: *Jour. Petrology*, v. 4, p. 302-306.
- Franzini, M. and Schiaffino, L., 1963, On the crystal structure of biotites: *Zeitschr. Kristallographie*, v. 119, p. 297-309.
- 1965, On the X-ray determination of the iron-magnesium ratio in biotites: *Zeitschr. Kristallographie*, v. 122, p. 100-107.
- French, B.M., 1966, Some geological implications of equilibrium between graphite and a C-H-O gas phase at high temperatures and pressures: *Reviews of Geophysics*, v. 4, p. 223-253.
- Frost, M.J., 1962, Metamorphic grade and iron-magnesium distribution between co-existing garnet-biotite and garnet-hornblende: *Geol. Mag.*, v. 99, p. 427-438.
- Fyfe, W.S., Turner, F.J., and Verhoogen, John, 1958, Metamorphic reactions and metamorphic facies: *Geol. Soc. America Mem.* 73, 259 p.
- Gilbert, M.C., Bell, P.M., and Richardson, S.W., 1969, The andalusite-sillimanite transition and the aluminum silicate triple point: *Carnegie Inst. Washington, Geophys. Lab. Ann. Rept. Director*, 1967-1968, p. 135-137.
- Gottardi, G., 1967, On a systematic error in the determination of the iron content of chlorites and biotites: *Am. Mineralogist*, v. 52, p. 1573-1575.
- Gower, J.A., 1957, X-ray measurement of the iron-magnesium ratio in biotites: *Am. Jour. Sci.*, v. 225, p. 142-156.
- Green, J.C., 1963, High-level metamorphism of pelitic rocks in northern New Hampshire: *Am. Mineralogist*, v. 48, p. 991-1024.
- Hall, A.J., 1941, The relation between color and chemical composition in the biotites: *Am. Mineralogist*, v. 26, p. 29-33.
- Harte, B., and Henley, K.J., 1966, Occurrences of compositionally zoned almanditic garnets in regionally metamorphosed rocks: *Nature*, v. 210, p. 689-692.

- Heinrich, E.W., 1946, Studies in the mica group: The biotite-phlogopite series: *Am. Jour. Sci.*, v. 244, p. 836-853.
- Henry, N.F., Lipson, H. and Wooster, W.A., 1961, The interpretation of X-ray diffraction photographs: New York, St. Martins Press, 282 p.
- Hollister, L.S., 1966, Garnet zoning: An interpretation based on the Rayleigh Fractionation Model: *Science*, v. 154, p. 1647-1651.
- Hounsflow, A.W., and Moore, J.M., 1967, Chemical petrology of Grenville Schists near Fernleigh, Ontario: *Jour. Petrology*, v. 8, p. 1-28.
- Kennedy, G.C., and Holser, W.T., 1966, Pressure-volume-temperature and phase relations of water and carbon dioxide, in Clark, S.P., Jr., ed., Handbook of physical constants, *Geol. Soc. America Mem.* 97, p. 371-383.
- Kretz, R., 1959, Chemical study of garnet, biotite, and hornblende from gneisses of southwestern Quebec, with emphasis on distribution of elements in co-existing minerals: *Jour. Geology*, v. 67, p. 371-402.
- Lindsley, D.H., 1965, Fe-Ti oxides: Carnegie Inst. Washington, Geophys. Lab. Ann. Rept. Director, 1964-65, p. 144-148.
- Miyashiro, Akiho, 1953, Calcium-poor garnet in relation to metamorphism: *Geochimica et Cosmochimica Acta*, v. 4, p. 179-208.
- Peikert, E.W., 1963, Biotite variations as a guide to petrogenesis of granitic rocks in the pre-Cambrian of northeastern Alberta: *Jour. Petrology*, v. 4, p. 432-459.
- Petruck, W., 1964, Determination of the heavy atom content in chlorite by means of the X-ray diffractometer: *Am. Mineralogist*, v. 49, p. 61-71.
- Phinney, W.C., 1963, Phase equilibria in the metamorphic rocks of St. Paul Island and Cape North, Nova Scotia: *Jour. Petrology*, v. 4, p. 90-130.
- Robie, R.A., Bethke, P.M., Toulmin, M.S., and Edwards, J.L., 1966, X-ray crystallographic data, densities and molar volumes of minerals, in Clark, S.P., Jr., ed., Handbook of physical constants, *Geol. Soc. America Mem.* 97, p. 60-70.

- Robie, R.A., and Waldbaum, D.R., 1968, Thermodynamic properties of minerals and related substances at 298.15°K (25.0°C) and one atmosphere (1.013 bars) pressure and at higher temperatures: U.S. Geol. Survey Bull. 1259, 256 p.
- Robinson, P., 1963, Gneiss domes of the Orange area, Massachusetts and New Hampshire: Ph.D. Thesis, Harvard University.
- 1967, Gneiss domes and recumbent folds of the Orange area, West Central Massachusetts, in Robinson, Peter, ed., Guide-book for field trips in the Connecticut Valley, Massachusetts, New England Intercollegiate Geological Conference, 59th annual meeting, p. 17-47.
- Rutherford, M.J., 1969, An experimental determination of iron biotite-alkali feldspar equilibria: Jour. Petrology, v. 10, p. 381-408.
- Schoen, R., 1962, Semi-quantitative analysis of chlorites by X-ray diffraction: Am. Mineralogist, v. 47, p. 1384-1392.
- Smith, J.V., 1968, The crystal structure of staurolite: Am. Mineralogist, v. 53, p. 1139-1155.
- Sturt, B.A., 1962, The composition of garnets from pelitic schists in relation to the grade of regional metamorphism: Jour. Petrology, v. 3, p. 181-191.
- Thompson, J.B., 1955, The thermodynamic basis for the mineral facies concept: Am. Jour. Sci., v. 263, p. 65-103.
- 1957, The graphical analysis of mineral assemblages in pelitic schists: Am. Mineralogist, v. 42, p. 842-858.
- Troger, W.E., 1956, Optische bestimmung der gesteinsbildenden Minerale: Teil 1, Bestimmungstabellen: Stuttgart, E. Schweizerbart'sche Verlagsbuchhandlung, 147 p.
- Turekian, K.K., and Phinney, W.C., 1962, The distribution of Ni, Co, Cr, Cu, Ba and Sr between biotite-garnet pairs in a metamorphic sequence: Am. Mineralogist, v. 47, p. 1434-1441.
- Van der Plas, L., and Tobi, A.C., 1965, A chart for judging the reliability of point-counting results: Am. Jour. Sci., v. 263, p. 87-90.
- Winchell, A.N., and Winchell, Horace, 1951, Elements of optical mineralogy -- an introduction to microscopic petrography: New York, John Wiley and Sons, 551 p.

Wones, D.R., 1967, Compositions of the micas, in American Geological Institute, Short course lecture notes: layer silicates, given by S. W. Bailey (and others), New Orleans, Louisiana, Nov. 17-19, 1967, p. DRW 46-DRW 78.

\_\_\_\_\_ and Eugster, H.P., 1965, Stability of biotite: experiment, theory and application: Am. Mineralogist, v. 50, p. 1228-1272.

## APPENDIX 1

SPECIMEN LOCATIONS  
(After Robinson, 1963)

G = Mt. Grace quadrangle  
O = Orange quadrangle

M = Millers Falls quadrangle  
N = Northfield quadrangle  
A = Athol quadrangle

## AMMONOOSUC VOLCANICS

- 7B5A      Quartz-sillimanite pod containing prisms of kyanite and staurolite enclosed in plagioclase-quartz-biotite gneiss. Mode includes pod and border with gneiss. On face of steep west-facing bluff east of 780-foot knob 800 feet east of bridge over Kidder Brook on old Winchester Road (G).

## SULFIDIC SCHIST MEMBER OF THE PARTRIDGE FORMATION

- 82            Coarse-grained sulfidic mica-staurolite-garnet schist. Cut on Rte. 2 (Orange-Athol bypass) 1400 feet southwest of West Orange (O).
- 167          Medium-grained sulfidic mica-garnet schist. On powerline east of Wendell village (M).
- 340          Medium-grained sulfidic plagioclase-biotite-sillimanite schist. On north side of Athol Road 1000 feet west of Mayo Corners (G).
- 721          Coarse-grained sulfidic plagioclase-biotite-garnet-sillimanite schist. In inner elliptical ring of Partridge Formation at 1260-foot contour on powerline southeast of hill 1317 (G).
- 1F8A        Medium-grained mica-garnet-staurolite-kyanite schist. 200 feet northwest of small 1200-foot knob immediately north of Orcutt Hill (M).
- 4F5A        Medium-grained mica-garnet-kyanite-staurolite schist. 200 feet west of 1000-foot contour on eastern part of Rockwell Hill Road southwest of Sibley Swamp (M).
- 36           Medium-grained mica-garnet-staurolite-sillimanite schist with coarse muscovite plates. On Rte. 2A due south of hill 827 west of Orange Village (O).
- 891A        Medium-grained mica-sillimanite-garnet schist with coarse muscovite plates and quartz-sillimanite knots. 1150 feet due east of hill 827 northwest of Orange Village (O).

- 895 Coarse-grained mica-sillimanite-garnet schist. 200 feet north of tiny 920-foot knob 600 feet due west of peak 1037 of Fall Hill north of Orange Village (O).
- 86 Medium-grained mica-plagioclase-garnet-sillimanite schist with coarse muscovite plates. Large cut on Rte. 2 (Orange-Athol bypass) at 630-foot terrace 2300 feet northwest of reservoir on Walnut Hill (O).

#### GRAY SCHIST MEMBER OF THE PARTRIDGE FORMATION

- 645 Medium-grained gray mica-garnet schist. Large cut face at bend of Rte. 2A 3000 feet southwest of bridge over Millers River in Athol (A).
- 680 Medium-grained mica-staurolite-garnet-sillimanite schist. On south face of 700-foot knob northwest of junction 674 at Blissville (G).
- B15 Coarse-grained gray mica-sillimanite-garnet schist. At south end of 1150-foot knob 1800 feet due west of junction 985 between Hastings Heights and Gale Roads (G).
- G65C Fine-grained dark-gray biotite-sillimanite-garnet schist with white sillimanite "eyes." 500 feet northeast of town corner on east slope of Beach Hill (G).
- J04B Medium-grained gray biotite-sillimanite schist. At 800-foot contour 1200 feet west of junction 723 southwest of Sheomet Lake (G).

#### CLOUGH FORMATION

- 418A Quartz-mica-garnet-sillimanite schist. 900 feet due north from point on Rte. 2A 700 feet east of junction with Rte. 78 east of West Orange. Collected 10 feet west of contact with Partridge Formation (O).

#### FITCH FORMATION

- 131B Sulfidic mica-sillimanite schist. Small cut on Nielson Road (O).
- B19 Sulfidic mica-garnet-staurolite-sillimanite schist. At 520-foot contour in Coolidge Brook east of Holtshire Road (O).

## LOWER MEMBER OF THE LITTLETON FORMATION, KYANITE ZONE

- 464 Coarse-grained silvery-gray mica-garnet-staurolite schist. Southwest ridge of Round Hill (N).
- 233 Coarse-grained silvery-gray mica-garnet-staurolite schist. 400 feet due east of road junction, elevation 1155 on north end of Brush Mountain (N).
- 796B In lower member of Littleton Formation 800 feet northeast of hill 1098 at south edge of Northfield quadrangle (N).
- 908 Medium-grained silvery-gray mica-garnet schist. At graphite prospect at 1120-foot contour on southwest side of second of First Bald Hills (counting from north) (N).
- L10 Fine-grained gray mica-garnet schist. Peak 994 on west ridge of Stratton Mountain (N).
- 239B Medium-grained mica-garnet-staurolite schist. At 1030-foot contour 1200 feet west-northwest of hill 1099 near south edge of Northfield quadrangle (N).
- 529A Fine-grained silvery-gray mica-garnet-staurolite schist. Railroad cut east of Stoneville (M).
- 558-C Medium-grained gray mica-garnet-staurolite schist. Immediately north of Clough Formation contact 800 feet due west of Moss Brook (O).
- 836 Coarse-grained gray mica-garnet-staurolite schist. Summit of hill 1207 at south end of First Bald Hill (N).
- 13 At east end of closure of 950-foot contour 750 feet due south of hill 1047 southeast of Laurel Lake (O).
- 872 Fine-grained gray mica-garnet schist. At 700-foot contour in first shallow gully east of southeast ridge of hill 1021 northwest of West Orange (O).

## LOWER MEMBER OF THE LITTLETON FORMATION, RETROGRADE ZONE

- 611 Dark-gray mica-chlorite-garnet phyllite. On southeast side of knob 1244 west of Poor Farm Hill (O).
- 649A Gray mica-chlorite-garnet phyllite with large pseudomorphs after staurolite. Small cut on Wendell Road, New Salem, 500 feet south of junction with Nielson Road at BM 967 (O).



LOWER MEMBER OF THE LITTLETON FORMATION, SILLIMANITE ZONE

- 314 Fine-grained gray mica-garnet-staurolite-sillimanite schist. At 770-foot contour 2700 feet N43°W from BM 603 on Lake Mattawa (O).
- M53 Mica-garnet-staurolite-sillimanite schist with coarse quartz-sillimanite knots and fine megascopic staurolite. At Clough Formation contact in first western tributary of Gales Brook south of Hodge Brook junction (G).
- B06 Coarse-grained mica-garnet-staurolite schist. Ten-foot knob in swamp 1200 feet northwest of Gales Pond to northeast of Gale Road (G).
- 828 In narrow syncline of Littleton Formation 100 feet north of road crossing south shoulder of Crag Mountain (N).
- 337 Medium-grained mica-garnet-staurolite schist. On Athol Road 3200 feet east of Warwick Village (G).
- 443 Fine-grained dark-gray mica-chlorite-garnet schist. In stream south of elevation 825 northeast of Chestnut Hill on west side of road (O).
- 869 Fine-grained gray mica-garnet-staurolite schist. In Orcutt Brook 1100 feet north-northeast of bridge at Rte. 2A (O).
- 6D6 At base of Littleton Formation at 810-foot contour 1300 feet due east of house on southeast shore of Hastings Pond (G).
- G23 Medium-grained mica-garnet-staurolite-sillimanite schist. On tiny 1170-foot knob on road branching north from Hastings Heights Road 2000 feet southeast of junction with Allen Road (G).
- 131A Fine-grained gray mica-garnet-staurolite sillimanite schist. Small cut on Nielson Road just west of Fitch Formation contact.
- A23 Rock exposed only at low water in southern part of Gales Pond (G).
- A76A Medium-grained mica-staurolite-garnet schist. On west lobe of 910-foot knob 1000 feet due north of Athol Road crossing of Rum Brook (G).
- 7B9 At 940-foot elevation on west side of 970-foot knob 1000 feet north of point where Rum Brook Road crosses Rum Brook (G).

- 1C7 At 1000-foot contour on west side of 1010-foot knob 1000 feet north of point where Rum Brook Road crosses Rum Brook (G).
- Q67 Medium-grained biotite-garnet-sillimanite schist with coarse quartz-sillimanite knots. Fifty feet west of Athol Road, Richmond, N.H., about 400 feet north of Massachusetts state line (G).
- A66 Mica-garnet-sillimanite schist with coarse quartz-sillimanite knots. On 930-foot knob west of 900-foot contour on Black Brook (G).
- M30 Coarse-grained biotite-sillimanite-garnet schist with quartz-sillimanite knots. At 1290-foot contour 800 feet due north of BM 1295 on Pudding Hill Road (G).
- U01B Medium-grained silvery-gray mica-garnet-staurolite schist with megascopic sprays of chlorite. At ridge crest on power-line west of Nielson Road (O).

ERVING MEMBER OF THE LITTLETON FORMATION, KYANITE ZONE

- 179 Medium-grained gray mica-garnet-staurolite schist. At 860-foot contour 150 feet northeast of head of stream which enters Millers River just east of Stoneville (M).
- 231A Medium-grained gray mica-staurolite-garnet schist. At about 1100-foot contour on steep slope due east of elevation 870 feet on Gulf Road (N).
- 230 50-feet higher elevation than 231A (N).
- 50 Fine-grained silvery mica-garnet-staurolite-kyanite schist. East of sand pit at about 810 feet on Depot Road, Wendell (M).
- 50A Coarse-grained mica-garnet-staurolite-sillimanite schist with coarse muscovite plates. On Rte. 2A due south of hill 827 west of Orange (O).
- X77D Medium-grained gray biotite-staurolite-garnet-kyanite schist. At 650-foot contour on north slope of Round Mountain, 900 feet southwest of 650-foot contour in Minot Brook (N).
- X10A Medium-grained gray mica-garnet-kyanite schist. At 1080-foot contour just east of amphibolite contact due east of elevation 980 feet on Gulf Road (N).
- X80 Coarse-grained gray mica-staurolite-garnet schist. At 750-foot contour due south of point at elevation 800 feet on west ridge of Round Mountain (N).

## APPENDIX 2

## ANALYSES AND ATOM RATIOS OF DARTMOUTH SAMPLES

	Chemical Analyses					Atomic Ratios Per 12 (O, OH, F)			
	L-12	14-55	15-55	6-55		L-12	14-55	15-55	6-55
SiO <sub>2</sub>	37.80	36.49	32.44	37.10	Si	2.776	2.755	2.467	2.771
TiO <sub>2</sub>	1.14	2.36	2.31	1.44	Al <sup>IV</sup>	1.224	1.245	1.533	1.229
Al <sub>2</sub> O <sub>3</sub>	20.66	22.69	19.10	19.81	Al <sup>VI</sup>	0.563	0.773	0.178	0.514
Fe <sub>2</sub> O <sub>3</sub>	1.59	0.77	0.73	1.10	Ti	0.063	0.134	0.132	0.081
FeO	16.33	20.05	25.74	18.43	Fe <sup>3+</sup>	0.088	0.044	0.042	0.062
MnO	0.07	0.08	0.13	0.05	Fe <sup>2+</sup>	1.002	1.265	1.636	1.150
MgO	9.54	5.49	6.12	8.91	Mn	0.004	0.005	0.008	0.003
CaO	0.08	0.07	0.72	0.09	Mg	1.043	0.617	0.693	0.991
Na <sub>2</sub> O	0.39	0.22	0.22	0.38	Li	0.006	0.018	0.040	0.006
K <sub>2</sub> O	7.64	7.74	5.28	7.67	Ca	0.006	0.006	0.059	0.007
H <sub>2</sub> O(+)	4.25	3.32	5.82	4.08	Na	0.056	0.032	0.032	0.055
H <sub>2</sub> O(-)	0.17	0.09	0.30	0.02	K	0.715	0.745	0.512	0.730
Li <sub>2</sub> O	0.02	0.06	0.13	0.02	Rb	0.002	0.001	0.001	0.002
F	0.22	0.04	0.08	0.21	OH	2.080	1.670	2.949	2.030
Rb <sub>2</sub> O	0.05	0.03	0.02	0.04	O	9.869	10.316	9.032	9.920
Total	99.95	99.53	99.14	99.35	F	0.051	0.010	0.019	0.049
O F	.09	.02	.03	.09	Inter-Layer	.785	0.784	0.604	0.794
	99.86	99.51	99.11	99.26	Octa-hedral	2.77	2.857	2.729	2.807
					Percent Fe of filled VI sites	39.4	45.81	61.47	43.18
					$\frac{F_{004}}{F_{005}}$	0.92	0.97	0.76	0.78

Analyst: C. O. Ingamells, Rock Analysis Laboratory, Department of Geology, University of Minnesota.

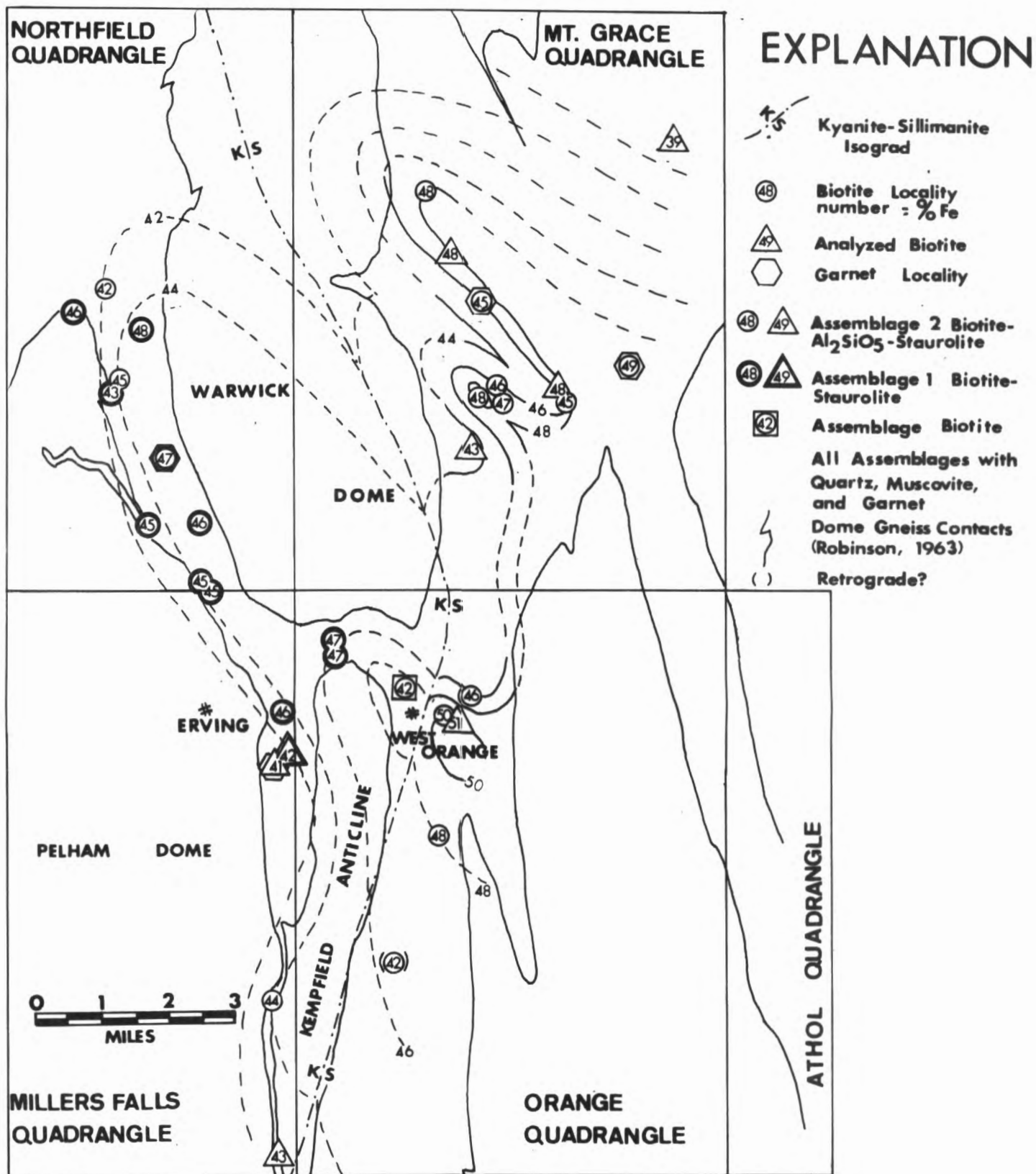
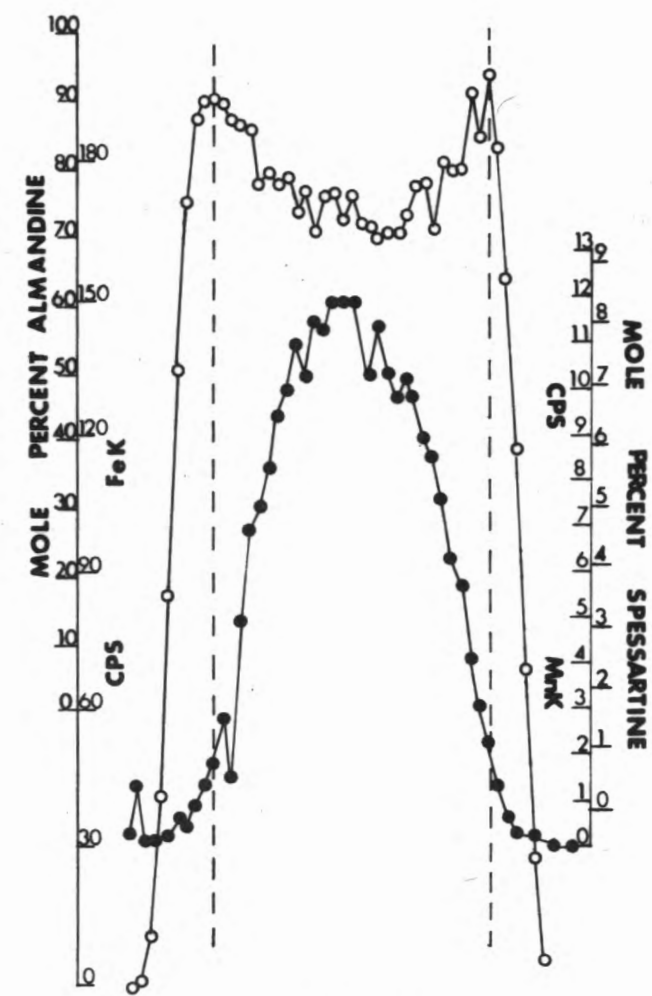
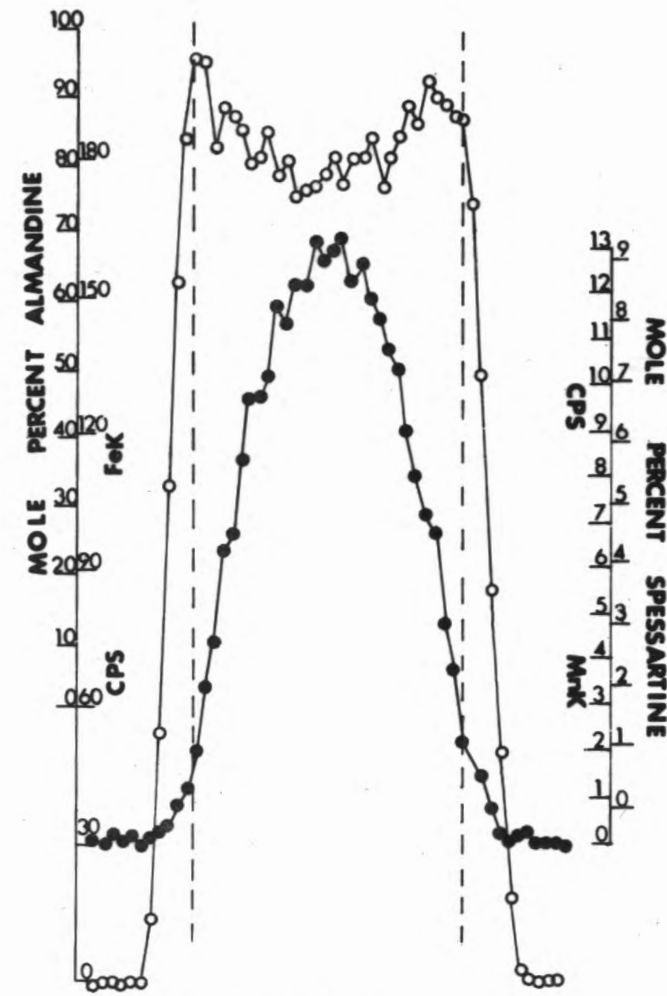


**PLATE 1 : CONTOUR MAP OF  
100 Fe/FILLED OCTAHEDRAL SITES  
IN BIOTITES IN ASSEMBLAGE 2**

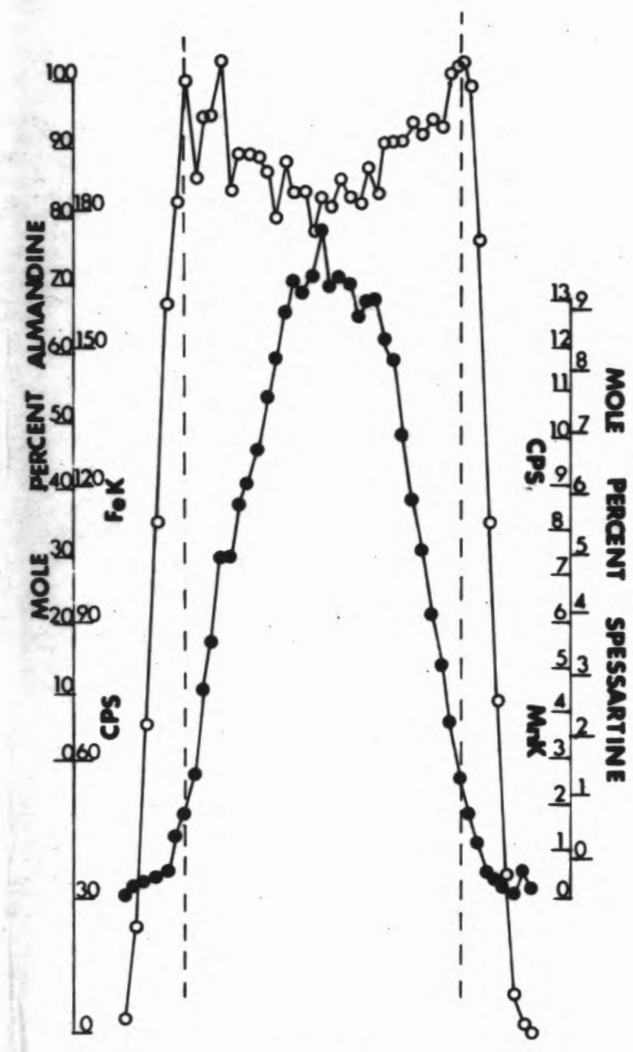
# PLATE 2. GARNET COMPOSITIONAL PROFILES



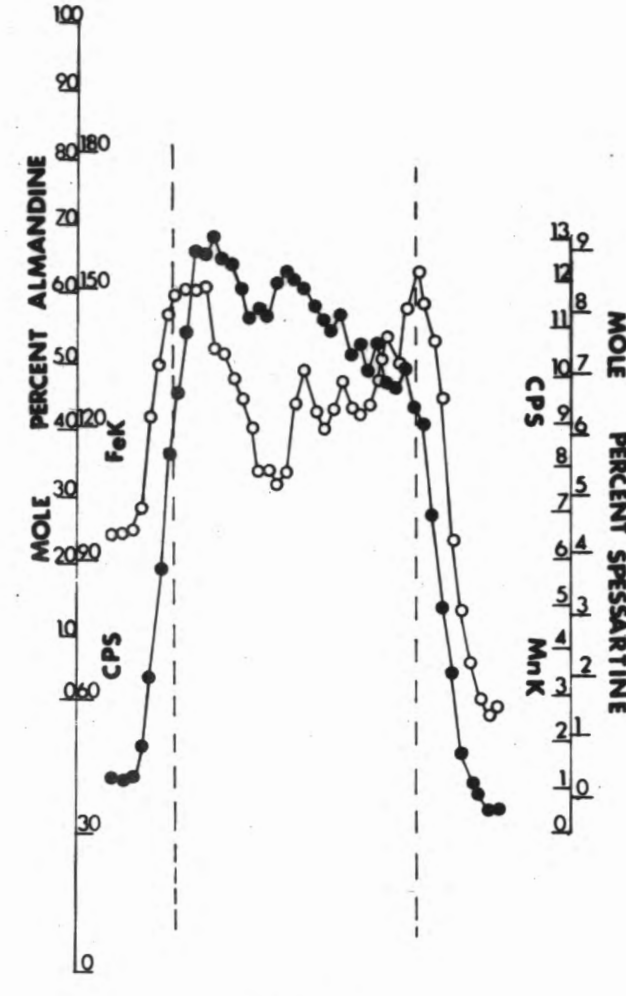
908A



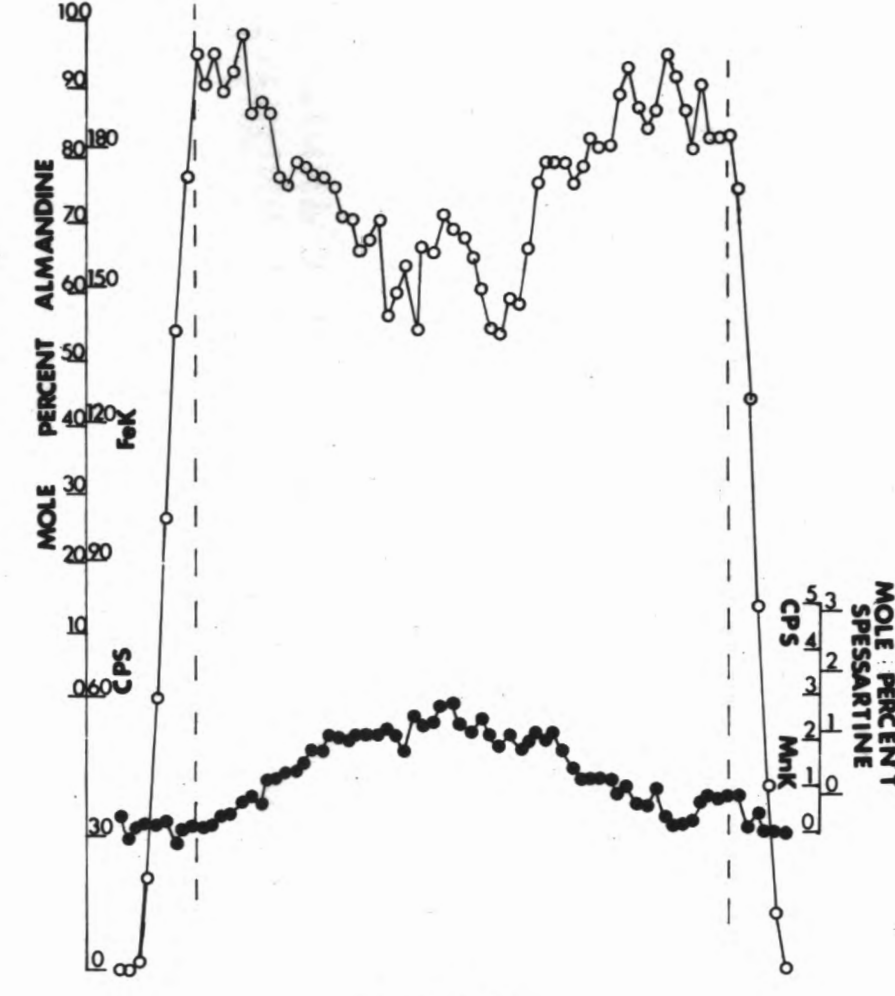
908B



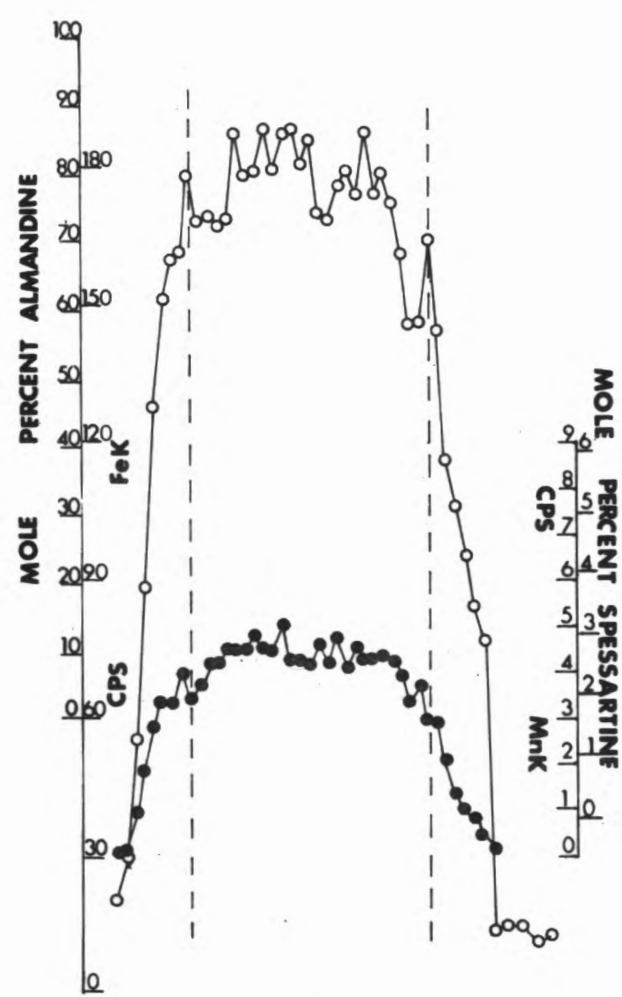
908C



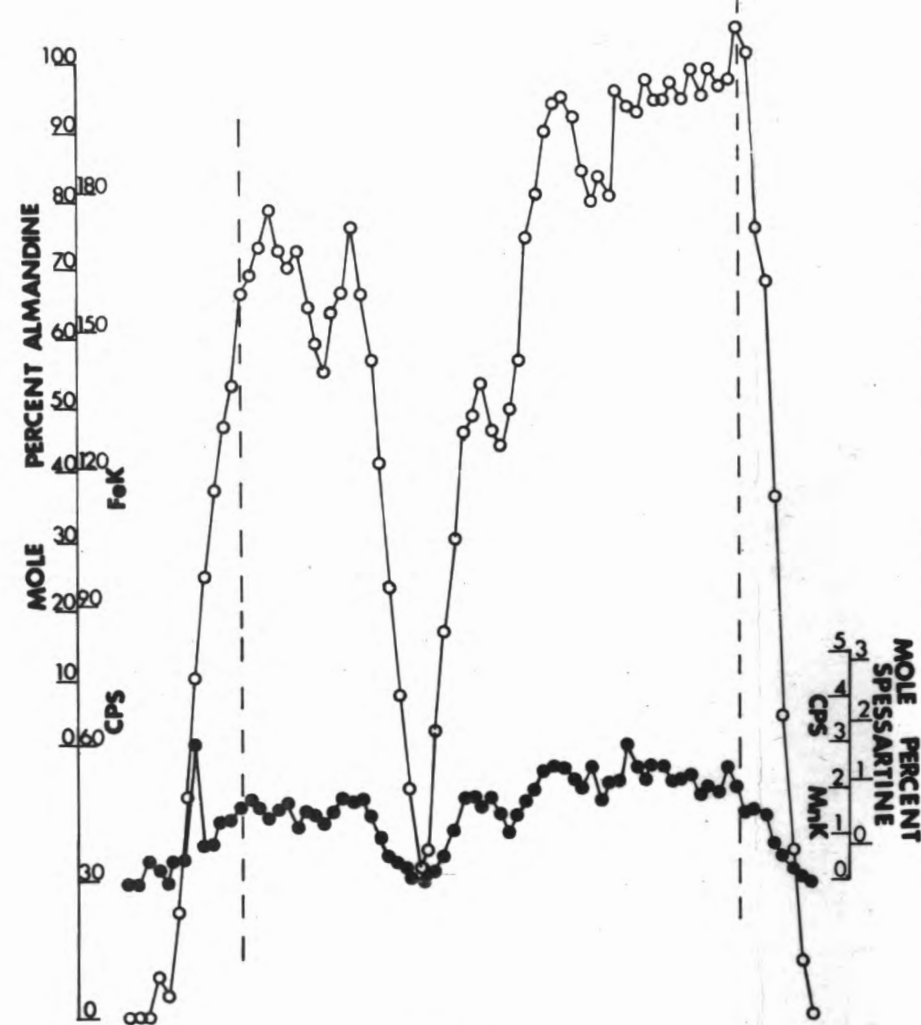
50A



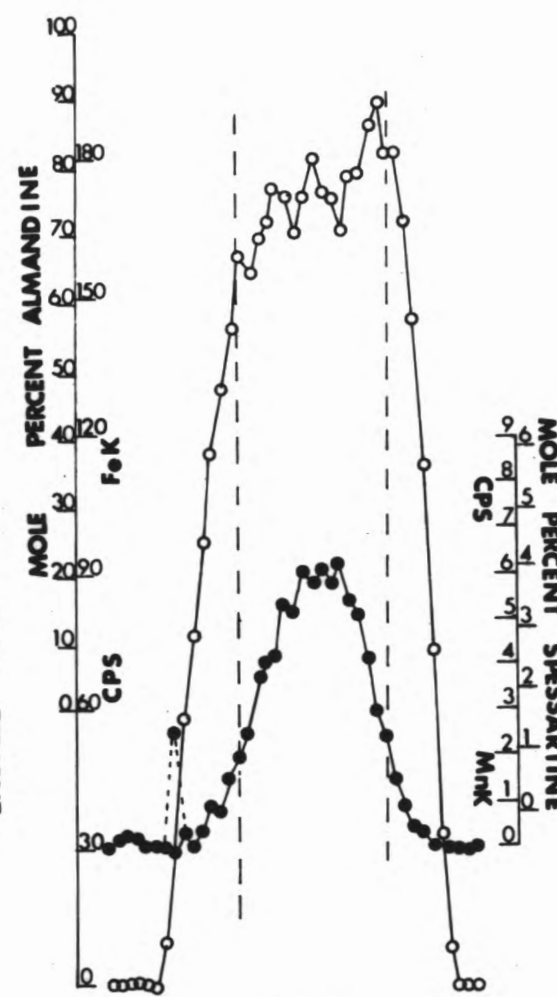
50AB



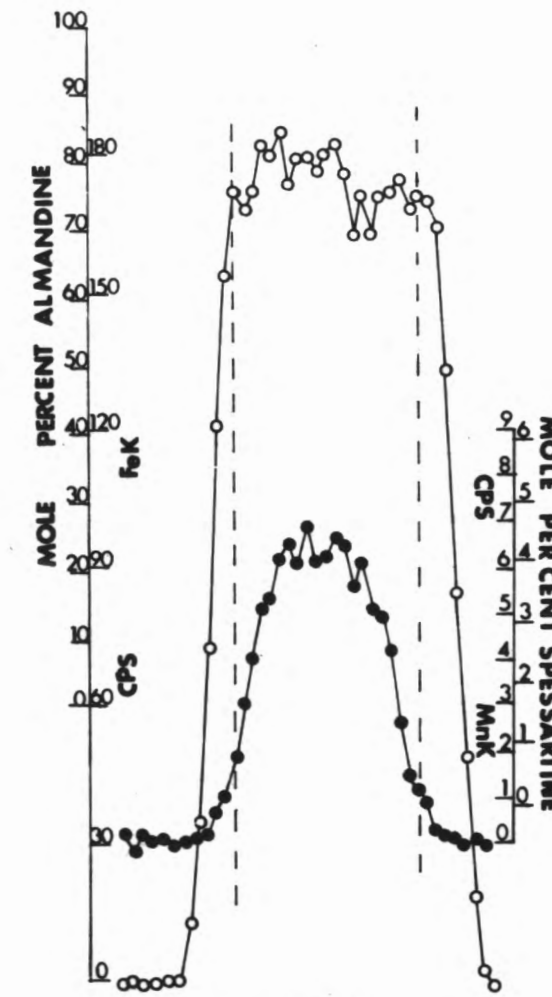
418C



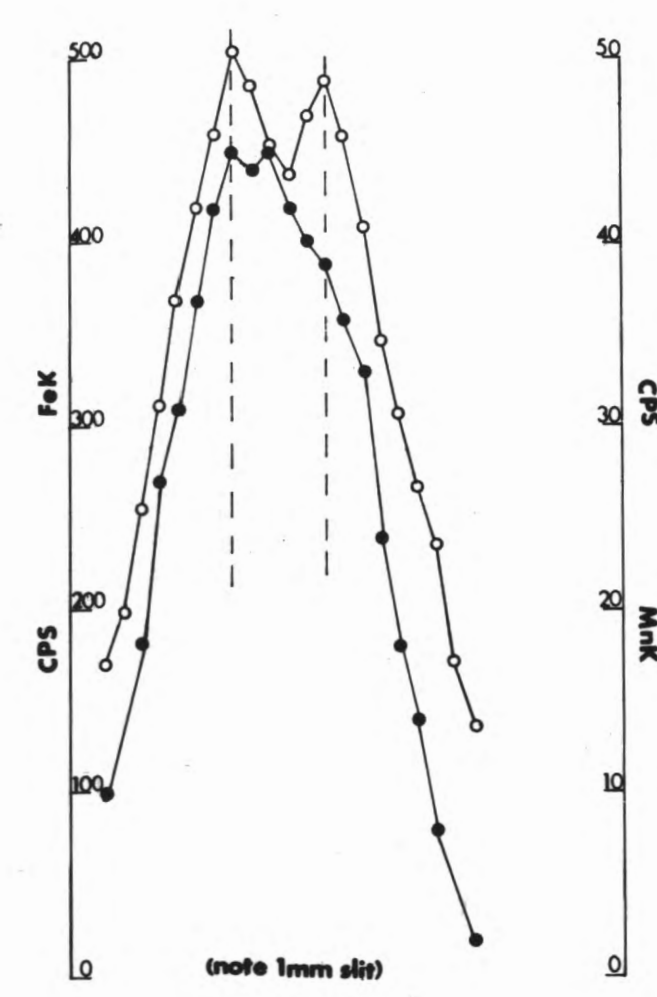
A76A



680



680R



36

## EXPLANATION

HORIZONTAL SCALE 1mm

WIDTH OF ANALYSIS ELLIPSE .5mm

Fe ○ — ○ — ○

Mn ● — ● — ●

GARNET EDGES - - - - -







